Universal higher-order bulk-boundary correspondence of triple nodal points

Patrick M. Lenggenhager [1,2,3,*], Xiaoxiong Liu [3], Titus Neupert [3] and Tomáš Bzdušek [1,3,†]

[1] *Condensed Matter Theory Group, Paul Scherrer Institute, 5232 Villigen PSI, Switzerland*

[2] *Institute for Theoretical Physics, ETH Zurich, 8093 Zurich, Switzerland*

[3] *Department of Physics, University of Zurich, Winterthurerstrasse 190, 8057 Zurich, Switzerland*

(Received 22 February 2022; accepted 27 July 2022; published 18 August 2022)

Triple nodal points are degeneracies of energy bands in momentum space at which three Hamiltonian eigenstates coalesce at a single eigenenergy. For spinless particles, the stability of a triple nodal point requires two ingredients: rotational symmetry of order three, four, or six; combined with mirror or space-time-inversion symmetry. However, despite ample studies of their classification, robust boundary signatures of triple nodal points have until now remained elusive. In this work, we first show that pairs of triple nodal points in semimetals and metals can be characterized by Stiefel-Whitney and Euler monopole invariants, of which the first one is known to facilitate higher-order topology. Motivated by this observation, we then combine symmetry indicators for corner charges and for the Stiefel-Whitney invariant in two dimensions with the classification of triple nodal points for spinless systems in three dimensions. The result is a complete higher-order bulk-boundary correspondence, where pairs of triple nodal points are characterized by fractional jumps of the hinge charge. We present minimal models of the various species of triple nodal points carrying higher-order topology, and illustrate the derived correspondence on Sc_3AlC which becomes a higher-order triple-point metal in applied strain. The generalization to spinful systems, in particular to the WC-type triple-point material class, is briefly outlined.

DOI: 10.1103/PhysRevB.106.085129

I. INTRODUCTION

The hallmark feature of higher-order topological phases in d dimensions is the presence of an anomaly on boundaries with dimensions $d-2$ or lower [1–23]. In two dimensions (2D), *second-order crystalline topological insulators* require additional chiral symmetry or particle-hole symmetry to protect zero-energy corner modes [11,24–26]. If such symmetries are absent and the corner modes merge into the bulk energy bands, the nontrivial second-order topology is instead revealed by a *corner-induced filling anomaly* [3,27–29], i.e., an obstruction to simultaneously satisfying charge neutrality and preserving the crystalline symmetries in the presence of corners. In particular, if the valence bands are filled and the crystalline symmetry preserved, the filling anomaly implies corner-localized charges. Remarkably, in the presence of rotational symmetry, the corner charges acquire fractional quantized values that can be predicted [28,30,31] using *symmetry indicators* [32–39], i.e., symmetry eigenvalues of the occupied bands at high-symmetry points (HSPs) in the Brillouin zone (BZ).

The notion of higher-order topology has recently been generalized to three-dimensional (3D) nodal phases with twofold and fourfold degeneracies, resulting in higher-order Weyl [40–44] and Dirac [9,45–47] semimetals, respectively, as well as to a class of nodal-ring semimetals obtained by perturbing Dirac degeneracies [48]. Such semimetals can be understood as 2D topological insulators which are augmented by a third dimension along which the higher-order topology changes, with the band nodes marking the occurrence of higher-order phase transitions. Correspondingly, higher-order topological semimetals are characterized by zero-energy hinge states (in the presence of chiral symmetry) or fractional hinge charges (in their absence) for a range of momenta demarcated by the band degeneracies. In light of these observations, a question of timely interest arises, namely, whether the phenomena associated with higher-order topology also extend to more intricate species of band nodes.

Triple nodal points [49–58] [*triple points* (TPs) for short] are threefold degeneracies of energy bands occurring at points in momentum space, and therefore constitute intermediates between Weyl and Dirac points. They occur on high-symmetry lines (HSL) in the BZ when a twofold-degenerate band [corresponding to a 2D irreducible corepresentation (ICR) of the HSL's little cogroup and forming what we call the *central* nodal line (NL)] is crossed by a third nondegenerate band [one-dimensional (1D) ICR of the little cogroup] [51]. In some cases, TPs are accompanied by additional NL arcs that lie off the rotation axis but coalesce with the central NL at a *nexus point* [59]. Triple points are thus classified [49,58–60] as type B if a nexus point coincides with the TP and as type A otherwise (where the appearance of a nexus point *near* the TP is optional). TPs were shown by angle-resolved photoemission spectroscopy to exist in the band structure of MoP [53] and WC [54].

In contrast to Weyl and Dirac points, a single TP generically results in a *metallic* state, due to the imbalance between the degeneracy of the crossing bands. However, *pairs* of TPs,

*Corresponding author: lenpatri@ethz.ch

†Corresponding author: tomas.bzdusek@psi.ch

TABLE I. Symmetry conditions to realize type-A vs type-B triple points (TPs) along a high-symmetry line (HSL) in the momentum space of spinless systems. The table compactly displays all magnetic point groups (MPGs) that (1) preserve one momentum component (such that the MPG corresponds to a little cogroup along some HSL), and that (2) support both 1D and 2D irreducible corepresentations (ICRs). The columns and the rows indicate generators of the MPG, where C_n is rotational symmetry of order n, $\mathcal{PT}$ is space-time inversion symmetry, and m_v is mirror symmetry with respect to a plane containing the rotation axis; furthermore, $C_n\mathcal{PT}$ corresponds to a composition of rotoinversion $C_n\mathcal{P}$ with time reversal $\mathcal{T}$. For brevity, we call $C_n\mathcal{PT}$ the *antiunitary rotational symmetry* of order n. For each entry, the corresponding MPG is first labeled per the notation of Ref. [64], and subsequently by the Hermann-Mauguin notation [65]. The last row in each cell indicates the possible TP types; in certain hexagonal cases both type-A and type-B TPs are possible, depending on the specific choice of ICRs as specified in Table II. The three MPGs colored in gray violate condition (2) and are therefore dismissed; the remaining 13 MPGs support TPs along HSLs, and are analyzed in the paper. The classification of TPs for all cases appears in Ref. [59]. In the derivation of the higher-order bulk-boundary correspondence, we exploit that the cases without $\mathcal{PT}$ correspond to subgroups of the cases with $\mathcal{PT}$. Similarly, the C_3 column corresponds to a subgroup of both the C_6 and the $C_6\mathcal{PT}$ columns.

	Trigonal	Tetragonal		Hexagonal	
Generators: ↓ and →	C_3	C_4	$C_4\mathcal{PT}$	C_6	$C_6\mathcal{PT}$
∅	16.1.60 (3) –	9.1.29 (4) –	10.3.34 ($\bar{4}'$) A	21.1.76 (6) –	22.3.81 ($\bar{6}'$) A
$\mathcal{PT}$	17.3.64 ($\bar{3}'$) B	11.4.38 ($4/m'$) A		23.4.85 ($6/m'$) A and B	
m_v	19.1.68 ($3m$) B	13.1.44 ($4mm$) A	14.3.50 ($\bar{4}'2'm$) A	25.1.91 ($6mm$) A and B	26.4.98 ($\bar{6}'m2'$) A
$\{\mathcal{PT}, m_v\}$	20.3.73 ($\bar{3}'m$) B	15.3.55 ($4/m'mm$) A		27.3.102 ($6/m'mm$) A and B	

formed when the 2D ICR consecutively crosses two 1D ICRs, can result in a semimetal with small Fermi pockets. We call such a TP configuration a *triple-point pair* (TPP). These nodal features can arise both in spinful [49] and spinless [51,60] systems; however, although there have recently been several efforts [59–63] towards their topological description and symmetry classification, it has remained an open question whether TPs or TPPs can be characterized by robust boundary signatures.

In this work, we answer both postulated questions in a single stroke: semimetallic TPPs are *generally* characterized by a higher-order bulk-boundary correspondence; namely, each species of TPP can be assigned a unique value of *fractional jump* of the hinge charge. We derive the exact correspondence by combining the symmetry classification of TPs [59,60] with the symmetry indicators of higher-order topology. Note that while we explicitly consider only TPs occurring in spinless systems, our mathematical analysis based on symmetry indicators can be easily generalized to the spinful case too. Nonetheless, the spinless setting allows us to provide a complementary *geometric* interpretation of the higher-order topology. Specifically, in the presence of space-time inversion ($\mathcal{PT}$) symmetry, non-Abelian band topology [66] in combination with the known properties of certain monopole and linking invariants [19,67–71], readily provide the result for the bulk-hinge correspondence for a subclass of TPPs in spinless systems.

Stable TPs can arise along HSLs with 13 distinct little cogroups. On the one hand, TPs can be protected if rotational symmetry C_n of order $n \in \{3, 4, 6\}$ is supplemented with $\mathcal{PT}$ *or* with mirror symmetry m_v with respect to a plane containing the rotation axis *or* with both $\mathcal{PT}$ and m_v. On the other hand, the combined symmetry $C_n\mathcal{PT}$ (which we call *antiunitary rotation*) of order $n \in \{4, 6\}$ can stabilize TPs with or without the $\mathcal{PT}$ and m_v symmetries. We provide an easily navigable summary of all admissible symmetry combinations and of their subgroup-supergroup relations in Table I. Nonsymmorphic symmetries do neither affect the possible little cogroups of HSLs along which stable TPs can arise nor the classification of those TPs [59], which is reflected in the fact that the symmetries listed in Table I are elements of the little *cogroup*, i.e., *point-group* symmetries.

The diverse range of symmetry combinations seemingly complicates the analysis. However, it turns out that all the cases of interest can be obtained by a proper perturbation of a system with $\mathcal{PT}$ symmetry. Therefore, our approach to analyze the topological invariants and the bulk-hinge correspondence of TPPs is to first deal with the $\mathcal{PT}$-symmetric cases, and afterwards consider the effect of perturbations to derive the results also for the $\mathcal{PT}$-broken cases. In particular, in the presence of $\mathcal{PT}$ we can characterize the TPP also by a second Stiefel-Whitney (2SW) or Euler monopole charge, of which the first one provides further insights into the bulk-hinge correspondence [19,22]. Our results for the correspondence between TPPs, and their associated fractional jump in the hinge charge, and (if also defined) their 2SW and Euler monopole charge, are summarized in Table II. The results also apply to nonsymmorphic space groups (SGs) with an appropriate identification of ICRs [59].

The paper is organized as follows. In Sec. II, we present a concrete C_4-symmetric tight-binding model that illustrates the phenomenology of TPP-induced higher-order topology,

including both the hinge-charge jump and the 2SW monopole invariant. This motivates our study and sets the stage for the subsequent general discussion. First, Sec. III discusses monopole charges induced by type-A TPs in $\mathcal{PT}$-symmetric spinless systems using simple manipulations with the non-Abelian band topology. The analysis reveals that pairs of TPs in three-band models can be characterized by the Euler monopole charge, while TPPs in four-band models can carry the 2SW monopole charge. The discussion is then substantially generalized in Sec. IV, where we use symmetry indicators to establish the main result of our work: a general bulk-hinge correspondence principle for TPPs *in spinless systems*. As intermediate results, we are led to also derive symmetry-indicator formulas for the 2SW and Euler monopole charge in the presence of rotational symmetry and a bulk-corner correspondence principle for the former, and we analyze the effect of symmetry breaking on TPPs. For simplicity, we first focus on symmorphic SGs and discuss the generalization to nonsymmorphic SGs only in Sec. VII.

After presenting the main results of our theoretical analysis, we apply the theory to concrete models. First, in Sec. V, we demonstrate the derived bulk-hinge correspondence on minimal tight-binding models for various TPP species. We first revisit the C_4-symmetric model from Sec. II and then discuss concrete Hamiltonians for the C_6- and C_3-symmetric cases. Next, we consider two material examples in Sec. VI. On the one hand, we consider Sc_3AlC in large uniaxial strain to provide a solid-state illustration of TPPs with the predicted fractional hinge-charge jump. On the other hand, we show that Li_2NaN under ambient conditions has a pair of TPs carrying a nontrivial Euler monopole charge, and we briefly discuss the consequences of this topological obstruction on the stability of the band nodes. In Sec. VII, we first explain how the symmetry-indicator formulas for the corner charge can be applied to compute the fractional hinge charge in a wire geometry even for nonsymmorphic SGs and then argue that the bulk-hinge correspondence of TPPs generalizes to nonsymmorphic SGs. Then, in Sec. VIII we present a short digression to TPPs in spinful systems, and argue that strongly spin-orbit-coupled compounds in the WC-type crystal structure studied by Ref. [49] could host the fractional hinge-charge jumps. Finally, we conclude in Sec. IX by summarizing the main results and outlining possible extensions of our work to other nodal configurations.

The main text is accompanied by several Appendixes which discuss details of our theoretical and numerical analysis: In Appendixes A and B we summarize our mathematical derivations that involve the symmetry indicators, in Appendix C we include details of the presented tight-binding models and explain how they were systematically constructed, in Appendix D we present methods to numerically extract the hinge charges from tight-binding models. Finally, in Appendix E we discuss the Euler monopole charge from the perspective of the non-Abelian band topology (significantly extended in the Supplemental Material [72], where we proof a conjecture relating the non-Abelian invariant computed on contours shifted by reciprocal lattice vectors) and illustrate this on several material examples.

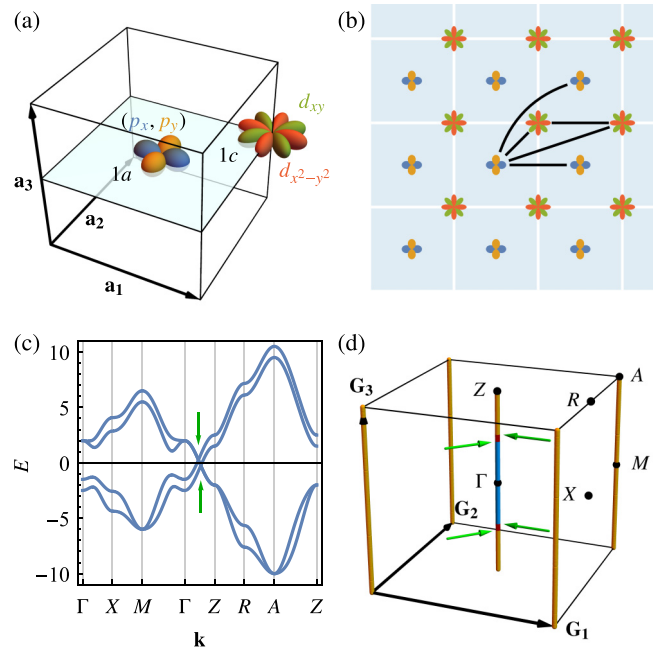

FIG. 1. Features of the model given in Eq. (1). (a) Real-space unit cell spanned by the lattice vectors $\mathbf{a}_{1,2,3}$ with the four orbitals: (p_x, p_y) at Wyckoff position $1a$ and d_{xy}, $d_{x^2-y^2}$ at $1c$. (b) Single layer (for fixed z) of the three-dimensional lattice. The blue shaded regions indicate the projection of the unit cells with the orbitals indicated in the same colors as in (a). Black lines (where further symmetry-related lines are dropped to maintain clarity) indicate the in-plane hopping processes included in the model. (c) Band structure along the high-symmetry lines. (d) Brillouin zone spanned by the reciprocal lattice vectors $\mathbf{G}_{1,2,3}$ with high-symmetry points $\{\Gamma, Z, X, R, M, A\}$ shown. Nodal lines in the first, second, and third band gaps are displayed in orange, red, and blue color, respectively. The four triple points of the model are indicated by green arrows in (c) and (d).

II. HINGE CHARGES INDUCED BY TRIPLE POINTS

To motivate our study of higher-order topology associated with TPs, we introduce a concrete model and investigate its phenomenology. The model assumes spinless particles on a tetragonal lattice (with lattice constants set to $a = c = 1$ for simplicity) and has the (symmorphic) SG $P4/mmm$ (No. 123) with isogonal point group D_{4h}. As illustrated in Fig. 1(a), we place (p_x, p_y) orbitals transforming in the ICR E_u at Wyckoff position (WP) $1a$, and the orbitals d_{xy} and $d_{x^2-y^2}$, transforming in B_{1g} and B_{2g}, respectively, at WP $1c$. The site-symmetry group of both considered WPs corresponds to the complete D_{4h} point group.

In the basis $(ip_x, ip_y, d_{xy}, d_{x^2-y^2})$, the considered model is expressed by the Bloch Hamiltonian

$$\begin{aligned}\mathcal{H}(\mathbf{k}) = &-[t_1+2t_2(\cos k_x+\cos k_y+\cos k_z)]\gamma_3 + t_3(\gamma_{14}-\gamma_{25})\\ &-t_4(\cos k_x-\cos k_y)(\gamma_{14}+\gamma_{25})\\ &+2t_5\sin k_x \sin k_y(\gamma_{15}-\gamma_{24})\\ &+2\sqrt{2}t_6\left(\cos\frac{k_x}{2}\sin\frac{k_y}{2}\gamma_1-\cos\frac{k_y}{2}\sin\frac{k_x}{2}\gamma_2\right),\end{aligned} \quad (1)$$

where $\gamma_1 = \sigma_x \otimes \tau_x$, $\gamma_2 = \sigma_x \otimes \tau_z$, $\gamma_3 = \sigma_z \otimes \mathbb{1}_\tau$, $\gamma_4 = \sigma_x \otimes \tau_y$, and $\gamma_5 = \sigma_y \otimes \mathbb{1}_\tau$ are gamma matrices obeying $\{\gamma_a, \gamma_b\} = 2\delta_{ab}$, and $\gamma_{ab} = \frac{i}{2}[\gamma_a, \gamma_b]$; Pauli matrices σ_i act on the WP degree of freedom, and Pauli matrices τ_i act on the orbital degree of freedom at fixed WP. The point group is generated by a $\frac{\pi}{4}$ rotation around the z axis $C_{4z} = -\mathrm{diag}(i\tau_y, \mathbb{1}_\tau)$, a π rotation around the y axis $C_{2y} = -\sigma_z \otimes \tau_z$, and inversion $\mathcal{P} = -\sigma_z \otimes \mathbb{1}_\tau$. Additionally, the Hamiltonian possesses time-reversal symmetry $\mathcal{T}$. Note that we have intentionally chosen the basis of p orbitals to be *imaginary*, which results in $\mathcal{PT} = \mathcal{K}$, such that the Bloch Hamiltonian is a real matrix [73]. In real space, Eq. (1) corresponds to the tight-binding model with in-plane hopping indicated by black lines in Fig. 1(b), whereas the nonvanishing out-of-plane hopping processes (not illustrated) are strictly vertical and intraorbital. We choose the model parameters such that the p orbitals have lower energy at all HSPs with the exception of a double-band inversion at Γ: $t_1 = 4$, $t_2 = t_6 = -1$, $t_3 = t_4 = \frac{1}{4}$, and $t_5 = -\frac{1}{4}$. The resulting band structure is shown in Fig. 1(c).

The HSL ΓZ has little cogroup C_{4v} combined with $\mathcal{PT}$, corresponding to the magnetic point group (MPG) $4/m'mm$ of Table I. The eigenstates of the model in Eq. (1) along ΓZ transform according to one 2D ICR E (p like) and two 1D ICRs B_1 and B_2 (d like). The degeneracy of p orbitals along ΓZ can be interpreted as a NL, which due to the double-band inversion at Γ is crossed by the two remaining d-like bands at four places, $k_z = \pm\kappa_1, \pm\kappa_2$, resulting in two TPPs at (κ_1, κ_2) and $(-\kappa_2, -\kappa_1)$, respectively, visible in Fig. 1(d). We observe that the TPs are not attached to additional NLs lying off the rotation axis, consistent with the classification in Refs. [59,60] that predicts all TPs on C_{4v}-symmetric HSLs to be type A. The only other band degeneracy exhibited by the model is the 2D ICR along the vertical hinge MA of the BZ, corresponding to a vertical NL formed by the two unoccupied p-like bands; however, this NL does not have any effect on the discussed phenomenology.

To uncover signatures of higher-order topology, we now consider a nanowire geometry, i.e., a system which is finite in x and y but infinite in z direction, at half-filling. Thus, only the momentum $k_z \in [-\pi, \pi]$ that runs along the fourfold rotation axis remains a good quantum number and the BZ is reduced to a *hinge Brillouin zone*. The considered in-plane termination is displayed in Fig. 2(a) and is chosen to respect all the symmetries of the Hamiltonian. Furthermore, we choose the ionic charge $(2|e|$ per unit cell to compensate for the half-filling of the electron bands; $e < 0$ is the elementary electron charge) to be placed at the center of the unit cell.

At fixed k_z in the hinge BZ we can view the bulk Hamiltonian as being described by an effective 2D model $\mathcal{H}_{k_z}(k_x, k_y)$ on the 2D lattice shown in Fig. 2(a). In Sec. V A, we use exact diagonalization to study this family of Hamiltonians $\mathcal{H}_{k_z}$. By computing the charge distribution of all occupied states for various k_z, we observe that the model has vanishing edge charge (related to vanishing Berry phase of the occupied bands), and a k_z-dependent corner charge (which is interpreted as a hinge charge of the 3D system) $Q_\llcorner(k_z)$ plotted as a blue line in Fig. 2(b). Three regions can be identified: (1) $Q_\llcorner = \frac{e}{4}$ for $|k_z| < \kappa_1$, (2) $Q_\llcorner = 0$ for $|k_z| > \kappa_2$, and (3) the region $\kappa_1 \leqslant |k_z| \leqslant \kappa_2$ where the bulk is gapless and the corner

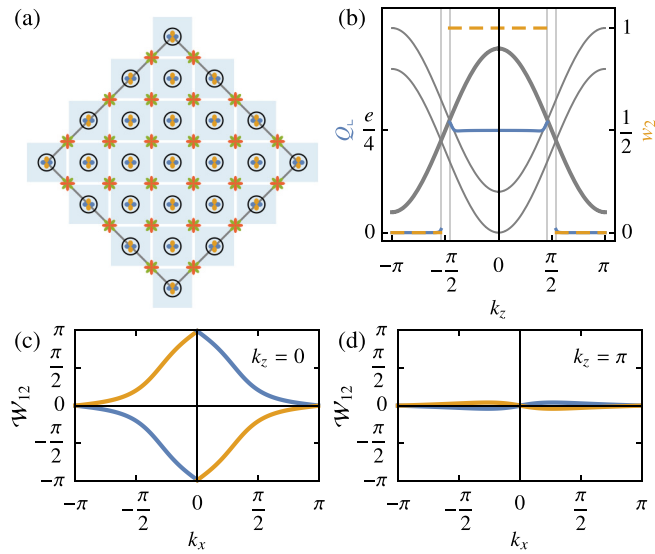

FIG. 2. (a) In-plane termination for the nanowire geometry considered in the main text. The blue shadowed regions denote unit cells with ionic charge $2|e|$ placed at the center (black circle). The electronic orbitals are illustrated as in Fig. 1. To establish terminology, we say that the depicted geometry consists of 3.5×3.5 unit cells (cf. Sec. V A). (b) Quantized hinge charges (blue solid line) identified using exact diagonalization (for details, see Sec. V A), and second Stiefel-Whitney (2SW) class (yellow dashed line) obtained from the Wilson-loop winding; both plotted as a function of k_z in the wire geometry. Cuts at fixed k_z can each be interpreted as 2D flakes as shown in (a) that are characterized by a corner charge $Q_\llcorner(k_z)$. The edge charge of the model vanishes. For reference, the bulk band structure along k_z for $k_x = k_y = 0$ is displayed in gray with the 1D (2D) degenerate bands plotted by a thin (thick) line. (c), (d) Wilson-loop spectrum of the two occupied bands in the 2D BZ for fixed $k_z = 0$ and π, respectively. For $k_z = 0$ (c) we observe a winding with odd parity, indicating a nontrivial 2SW class.

charge therefore undefined. These regions reflect exactly the regions defined by which gap the central NL is located in [cf. Fig. 1(d)]. In particular, we observe a jump of the hinge charge from region (2) to region (1) by $\Delta Q_\llcorner = \frac{e}{4}$.

The difference in bulk topology between these regions is reflected in the Wilson-loop spectrum. Figures 2(c) and 2(d) show the Wilson-loop spectrum of the occupied bands for $k_z = 0, \pi$, respectively. While the former winds once around the 2D BZ torus, the latter does not. Recall [68] that the parity of the winding of the Wilson-loop eigenvalues determines the 2SW class. Note that the $\mathcal{PT}$ symmetry of the model allows us to compute the 2SW class for a cut at *each* value of k_z where the central energy gap is open, plotted as a yellow dashed line in Fig. 2(b). We thus make the observation that the pair of TPs separates a region in the hinge BZ with nontrivial 2SW class and nonvanishing hinge charge $\frac{e}{4}$ from a region with trivial 2SW class and vanishing hinge charge.

Motivated by the fractional jump of the hinge-charge observed for the model in Eq. (1) and by the jump's correlation with the 2SW class, we organize the next sections as follows. First, in Sec. III we present a geometric discussion that explains how type-A TPs give rise to nontrivial 2SW (Sec. III A) and Euler (Sec. III B) monopole charges by appealing to

the relation between monopole charges and multiband nodal links. These insights will readily explain the 2SW class observed in this section's model. In Sec. IV, we then adopt the method of symmetry indicators and generalize the observations discussed above to establish a comprehensive bulk-hinge correspondence for TPPs. Finally, in Sec. V we first revisit this section's model in the light of those general results, before discussing two C_6-symmetric examples: one with type-A TPs and one with type-B TPs.

III. MONOPOLE CHARGES INDUCED BY TRIPLE POINTS

In this section we argue that pairs of type-A TPs in spinless systems can be imbued with monopole charges. This conclusion is achieved by adopting the geometric interpretation of monopole charges as linking numbers [70,71]. After presenting the general argument, we apply it to two specific configurations of type-A TPs: a four-band configuration resulting in a nontrivial second Stiefel-Whitney (2SW) monopole charge in Sec. III A, and a three-band configuration resulting in a nontrivial Euler (but trivial 2SW) monopole charge in Sec. III B. In both cases we elaborate on the implications of the monopole charge on the stability of the NL segments and on the bulk topology. (NL segments demarcated by type-B TPs are not easily analyzed through the geometric method considered in the present section. We address them using the more general framework of symmetry indicators in Sec. IV.)

The 2SW class w_2 is a stable $\mathbb{Z}_2$-valued invariant defined on a closed 2D manifold with a spectral gap whenever there is an antiunitary momentum-preserving symmetry squaring to $+\mathbb{1}$, such as $\mathcal{PT}$ or $C_2\mathcal{T}$ [19]. Note that we require only *one* gap, here the *principal* gap, to be open on the 3D manifold. The 2SW class remains well defined in the presence of nodes in other band gaps. On a spherical surface enclosing nodal-ring degeneracies in 3D, the 2SW class defines a monopole charge that enhances the stability of the node [67,68,70]. For 2D insulating systems, on the other hand, the 2SW class on the BZ torus defines a bulk topological invariant of the full system [19,20,22,70] similar to the Chern number.

The $\mathbb{Z}$-valued fragile extension of the 2SW class, which can be defined for a two-band subspace separated from the rest of the spectrum by energy gaps, is the Euler class χ [68,74,75]. Note that only its absolute value is gauge invariant [73] (see also Appendix B 3); we will therefore restrict χ to non-negative values. Under the addition of trivial bands to the two-band subspace, only the parity of the Euler class is stable and reduces to the 2SW monopole charge discussed above, $w_2 = \chi \mod 2$.

We now investigate the monopole charges associated with configurations of TPs. For concreteness, in this section we focus on NL segments that are demarcated by a pair of type-A TPs (this, in particular, implies the presence of C_n symmetry with $n = 4$ or 6 [60]). We will call the energy gap in which that NL segment is formed the *principal gap* [73]. To understand why such NL segments could carry a nontrivial monopole charge, consider one such NL segment and require that there are no additional band nodes in the principal gap for the considered range of k_z. Two examples of such configurations are shown in Figs. 3(b) and 5(a), where nodes in the principal gap are shown in red.

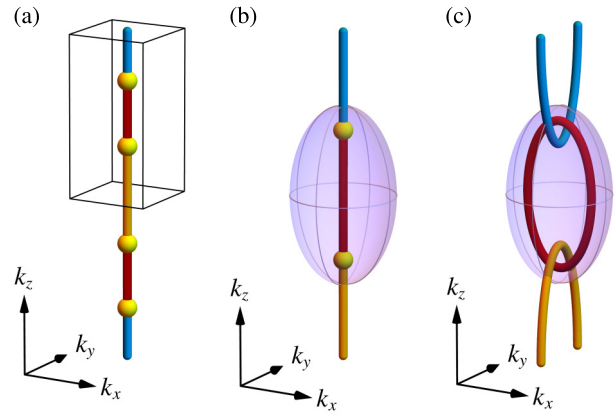

FIG. 3. (a) Two pairs of type-A triple points (TPs, yellow dots) formed by consecutive triplets of bands. All TPs are protected by C_4 or C_6 symmetry with respect to the z axis. In k_z direction the full extent of the Brillouin zone is shown. Nodal lines in the first, second, and third gaps of a four-band model are shown in orange, red, and blue, respectively. (b), (c) Closeup of the boxed region in (a) with the ellipsoid, on which the second Stiefel-Whitney (2SW) class is computed with respect to the principal (red) band gap, shown in purple. (c) Multiband nodal links that form after breaking the rotational symmetry. The red nodal ring carries a nontrivial value of the 2SW class computed on the purple ellipsoid. By continuity, the red nodal segment in (b) also carries a nontrivial 2SW class.

As has been argued in Ref. [60], adding a small C_n-breaking but $\mathcal{PT}$-preserving perturbation transforms TPs into multiband nodal links as illustrated in Figs. 3(c) and 5(b) and 5(c). Crucially, the linked nodal rings are in band gaps adjacent to each other, and such linking was shown to be in a one-to-one correspondence [70,71] with monopole charges. Thus, there potentially is a nontrivial monopole charge on a surface enclosing the nodal ring of interest [purple ellipsoid in Figs. 3(c) and 5(b) and 5(c)]. By continuity we can switch this perturbation off without closing the principal energy gap on the enclosing surface, which allows us to assign the same monopole charge also to the original NL segment, i.e., on the ellipsoid in Figs. 3(b) and 5(a). In the following two subsections we investigate in detail the implications of the linking for the bulk topology of the two specified type-A TP configurations.

A. Second Stiefel-Whitney monopole charge from triple points

We first analyze the four-band configuration with two TPs, in which case the 2D ICR is transferred from occupied to the unoccupied bands along a rotation axis (without loss of generality set to k_z) as shown in Fig. 3(b), similar to the case of the model discussed in Sec. II. We call such a configuration of TPs a *triple-point pair* (TPP). It involves three species of NLs, displayed in the figures in orange, red, and blue according to increasing band index. The individual TPs correspond to locations where the 2D ICR transfers from one energy gap to another. Due to the periodicity in k_z, the minimal model of such a configuration involves *two* such TPPs [cf. Fig. 3(a)].

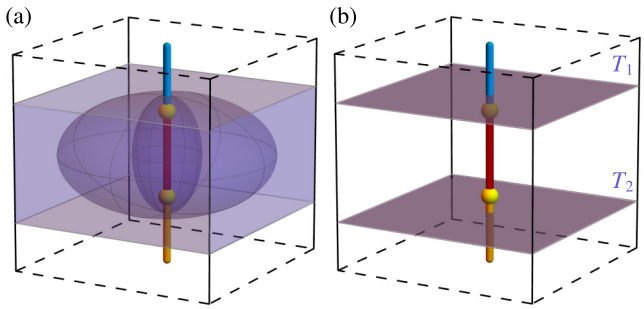

FIG. 4. Relation between a nodal-line segment carrying a nontrivial second Stiefel-Whitney monopole charge, and a pair of two-dimensional insulators characterized by the $\mathbb{Z}_2$-valued 2SW class. The black frame represents the complete momentum-space extent of the Brillouin zone in the two horizontal directions (solid black lines), but not in the vertical direction (dashed black lines). (a) The monopole charge of the red nodal-line segment is calculated on a surface enclosing it (innermost purple ellipsoid), which can be continuously inflated (second purple ellipsoid) until it fills the whole BZ in k_x and k_y directions (purple cuboid). (b) The purple cuboid in (a) is equivalent to two horizontal planes (actually tori) T_1 and T_2 at the appropriate k_z values.

Here it is sufficient to consider the upper half of the BZ, Fig. 3(b), with one (red) NL segment in the principal gap. Applying the argument outlined above for the purple ellipsoid shown in the figure, we consider a small perturbation leading to the multiband nodal link [60] [cf. Fig. 3(c)]. Since one NL in each of the two adjacent band gaps (first and third) is linked with the red nodal ring, the purple ellipsoid carries nontrivial 2SW monopole charge $w_2 = 1$ [70]. This has immediate consequences for the stability of the red NL segment and thus for the two TPs in Fig. 3(b). In particular, the monopole charge guarantees the persistence of the red NL even when the rotational symmetry is broken (and the 2D ICR split) as long as the $\mathcal{PT}$ symmetry is preserved.

We next discuss implications of the monopole charge for the bulk topology. Assuming there are no additional NLs in the principal gap in the relevant k_z range, the ellipsoid enclosing the red NL segment can be continuously deformed as illustrated in Fig. 4(a) until it spans the whole BZ in k_x and k_y directions for a finite range of k_z. Due to the periodicity in the BZ, the contributions from opposite vertical faces of that surface cancel and we are left with the two horizontal planes T_1 and T_2 shown in Fig. 4(b). Note that these are actually 2D tori which can be interpreted as the BZs of certain 2D systems, namely, ones with the two-dimensional Hamiltonians $\mathcal{H}_{k_z}(k_x, k_y) := \mathcal{H}(k_x, k_y, k_z)$.

Owing to the continuous deformation of the surface, the 2SW class does not change, such that $w_2(T_1) + w_2(T_2) = 1 \mod 2$. Consequently, one of the two planes will be trivial, $w_2 = 0$, and the other nontrivial, $w_2 = 1$. Viewing them as 2D systems as described above, the latter is a 2D insulator with nontrivial 2SW class, called *Stiefel-Whitney insulator* (SWI) [70]. In the simultaneous presence of C_2 rotational and of chiral symmetry, SWIs were shown [19,22] to have robust zero-energy corner states accompanied by half-integer corner charges. Our situation is different: we do not assume chiral symmetry, and the order of rotational symmetry necessary to protect type-A TPs is $n \in \{4, 6\}$. Until now, the (higher-order) bulk-boundary correspondence for (nonchiral) SWIs with rotational symmetry has not been clarified. We derive this piece of information in Sec. IV A; in particular, we show that the corner charge in the presence of trivial (nontrivial) 2SW class is quantized to even (odd) multiples of $\frac{e}{n}$. We subsequently apply the result to study the bulk-hinge correspondence for TPPs of both type A and type B in Sec. IV C.

B. Euler monopole charge from triple points

An even simpler configuration is obtained in a three-band model with two type-A TPs formed by the *same* triplet of energy bands, as illustrated in Fig. 5(a). Since the ordering of the ICRs along the rotation (k_z) axis has to be the same at both $k_z = -\pi$ and π due to the periodicity of the momentum space, it again follows that the number of TPs formed by the three bands is even. In the minimal model, the NL changes the band gap twice, once from the second (blue) to the first (red) and once back to the second gap, at two TPs (yellow dots). Here we assume a single occupied and two unoccupied bands, such that the two-band subspace allows us to define the Euler monopole charge $\chi \in \mathbb{Z}$ on the purple ellipsoid in Fig. 5(a) [68].

The Euler monopole charge of a nodal ring is determined by the linking with NLs in the adjacent band gap, similar to the case of the 2SW class, such that we can again apply the argument with the breaking of the rotational symmetry. However, here the *orientation* of the linked NLs becomes important [71]. Recall that in a generic multiband setting the orientation of a NL can be formally defined via the non-Abelian generalized quaternion invariant [66]. In particular, this orientation obeys the same noncommutative rules as the winding number of point nodes in 2D as reported by Ref. [19], allowing us to interpret the NLs as braid trajectories. The orientation [indicated by arrows in Figs. 5(b) and 5(c)] of the adjacent (blue) NL at the point where it crosses the disk bounded by the principal (red) nodal ring determines the flux ± 1, indicated in gray. We observe that two distinct scenarios can arise after breaking the rotational symmetry: Fig. 5(b) where the total flux vanishes, and Fig. 5(c) where it is nonvanishing. According to Ref. [71] the former implies $\chi = 0$ and the latter $|\chi| = 2$.

While we have so far only established the *possibility* of the red NL segment carrying a nontrivial Euler monopole charge, the two cases $\chi = 0$ and $|\chi| = 2$ can be distinguished based on the Zak-Berry phases $\phi_{2,3} \in \{0, \pi\}$ along the k_z axis of the two bands involved in the formation of the blue NL in the adjacent energy gap, i.e., the NL segment on the opposite side of the triple point than the segment under consideration. Assuming the minimal model with only a single pair of TPs along k_z, as shown in Fig. 5, there are in fact only two nodal rings (the red one in the center, and the blue one on the boundary), since the two blue NL segments belong to the *same* nodal ring, only shifted by a reciprocal lattice vector **b**. Notably, the two *copies* of the blue NL ring do not necessarily exhibit consistent orientations: the orientation of a NL

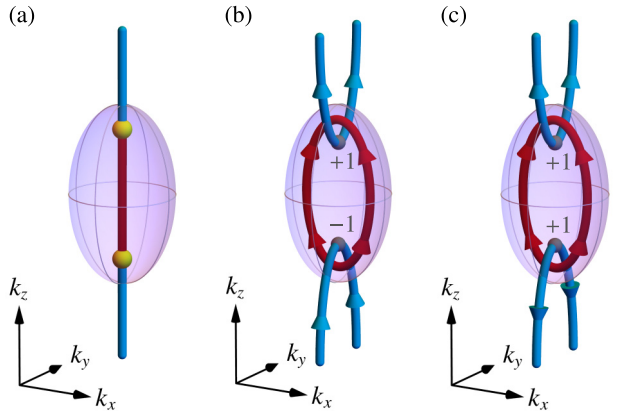

FIG. 5. (a) Type-A triple points (yellow dots). The red (blue) line indicates nodal lines formed by the lower (upper) two bands of a three-band model. In k_z direction the full extent of the Brillouin zone is shown. (b), (c) Multiband nodal link formed from (a) by breaking the rotational symmetry protecting the triple points. The flux (gray ± 1's) depends on the orientation of the two blue nodal lines at the intersection points (gray) with the disk bounded by the red nodal ring [71]. The total flux vanishes in (b) giving rise to $\chi = 0$, but is finite in (c) such that $|\chi| = 2$. In the presence of mirror $m_z : k_z \mapsto -k_z$ symmetry, the difference between the situations (b) and (c) is reflected in the mirror eigenvalues of the three bands at $k_z = 0$ vs $k_z = \pi$ (cf. the discussion in Sec. VI B).

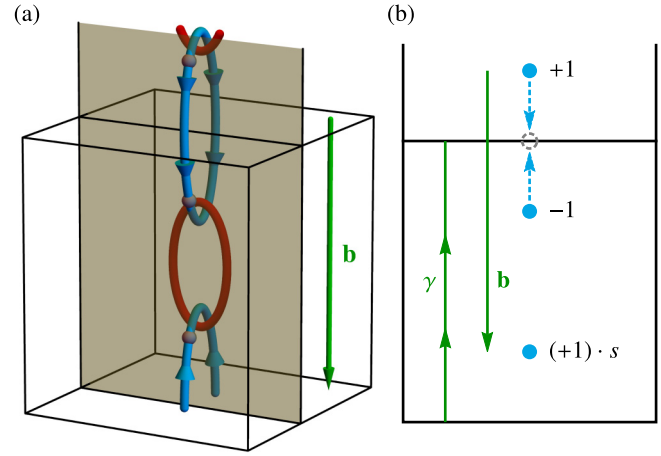

FIG. 6. (a) Nodal-line (NL) configuration (here colored red vs blue for NLs formed by the lower vs upper two bands of a three-band model) in the first Brillouin zone (BZ, black frame) and part of the second BZ. The two blue displayed NLs are displaced by a reciprocal lattice vector **b** (green arrow). The blue NL is intersected by a 2D plane (pale brown) at two inequivalent points (gray dots). The shown orientation of the blue NLs is compatible with $\phi_2 + \phi_3 = \pi$ (cf. Sec. III B). (b) Band nodes (blue points) on the 2D plane in (a), with winding numbers ± 1 inherited from the orientation of the NLs in 3D. The two upper point nodes have opposite orientation, because they pairwise annihilate (blue arrows pointing to the gray disk) when the vertical plane is shifted away from the NL composition. The point nodes displaced by **b** have winding numbers differing by a factor $s = e^{i(\phi_2+\phi_3)} = \pm 1$ [19].

between bands 2 and 3 at $\mathbf{k} + \mathbf{b}$ is *reversed* compared to the one at $\mathbf{k}$ if and only if $\phi_2 + \phi_3 = \pi \mod 2\pi$. In Appendix E (with additional information detailed in the Supplemental Material [72]), we formalize this statement in the framework of the non-Abelian generalized quaternion invariant [66,71]. The result applies to an arbitrary number of bands and provides a general transformation rule for the NL orientation between neighboring BZs depending on the Berry phases.

The orientation reversal can be related to the properties of Dirac points in 2D derived in Ref. [19] if we consider a 2D cut [brown plane in Fig. 6(a)] through the BZ that intersects the blue NLs. Note that continuity implies that the two upper point nodes [i.e., upper two blue dots in Fig. 6(b)] have opposite winding number because they correspond to cuts through the *same* nodal ring, i.e., they manifestly annihilate when sliding the plane away from the nodal-link composition. According to Ref. [19] the copy of the uppermost node with winding number $+1$ in an adjacent BZ (bottom-most node), i.e., shifted by the reciprocal lattice vector **b**, has winding number $(+1)s$, where $s = e^{i(\phi_2+\phi_3)}$ and ϕ_j is the Zak-Berry phase of band j on the contour γ winding around the 2D BZ in the direction of **b**.

Although the even-valued Euler class is a *fragile* topological invariant, it may still imply unusual stability of the corresponding NL under perturbations, which we briefly investigate in Sec. VI B. The following Secs. IV and V investigate in more detail the case of TPs in the four-band configuration, which may exhibit the stable 2SW class, and we derive their associated signatures in the fractional hinge charges.

IV. HIGHER-ORDER BULK-BOUNDARY CORRESPONDENCE

In this section we mathematically establish the higher-order bulk-boundary correspondence principle foreshadowed in Sec. II: a triple-point pair (TPP) in a SG with (antiunitary) rotational symmetry of order $n \in \{2, 3, 4, 6\}$ is generally associated with a fractional jump of the hinge charge. While the previous Secs. II and III explicitly considered only type-A TPs in systems with $\mathcal{PT}$ symmetry, the discussion in this section is more general and encompasses *all* the TPs reported by the classification in Refs. [59,60] and reproduced in Table I in *symmorphic SGs*. (We discuss the generalization to nonsymmorphic SGs in Sec. VII.) Furthermore, we report a correspondence between the 2SW monopole charge (if it is defined) of the NL segment connecting the two TPs and the value of the hinge-charge jump: a trivial 2SW monopole charge implies a $\pm\frac{e}{n}$ jump, while a nontrivial value results in a jump by $\pm\frac{2e}{n}$. We remark that the hinge-charge jump associated with a TPP always occurs without a change in the bulk polarization. This implies that if there is no fractional surface charge appearing on one side of the TPP, then there is also no fractional surface charge on the other side of the TPP, thus guaranteeing that the fractional jump in the hinge charge is observable.

We begin in Sec. IV A by discussing the 2D SWI with C_n-rotational symmetry. Here, we adapt the C_2-symmetry-indicator formula [19] for the 2SW class to C_n-rotational symmetry, where $n \in \{4, 6\}$, and show that the value of the

2SW class constrains the possible fractional corner charges of the C_n-symmetric 2D system with vanishing bulk polarization. Subsequently, by temporarily adopting a stronger assumption on energy gaps in the band structure, we derive in Sec. IV B a symmetry-indicator formula for the Euler monopole charge of TPPs in the presence of C_n rotational symmetry. In Sec. IV C, we combine the results obtained in the previous two subsections with the classification of TPPs to derive the general bulk-hinge correspondence principle for all possible TPP configurations in $\mathcal{PT}$-symmetric systems. Finally, in Sec. IV D, we discuss the effect of breaking various symmetries; in particular, we extend the bulk-hinge correspondence principle to TPPs protected by *all* MPGs listed in Table I. Our results for the bulk-hinge correspondence are compactly summarized in Table II, while Table III compiles the various topological phase transitions induced by symmetry breaking.

A. Stiefel-Whitney insulator with rotational symmetry

We consider an insulating 2D system with $C_2\mathcal{T}$ and C_n symmetry, where C_2 and C_n are with respect to the same axis perpendicular to the system. Due to the $C_2\mathcal{T}$ symmetry (where C_2 acts like inversion in 2D) the insulator is characterized by the 2SW class, while the C_n symmetry implies fractional corner charges [28–30] if the edge charge vanishes. For simplicity we assume that all the positive ionic charge, which compensates for the negative charge of the filled electron bands, is located at the maximal Wyckoff position $1a$, i.e., the center of the square unit cell. In Sec. IV C we will see that for $n = 3$, the 2SW class is not symmetry indicated. Thus, we restrict the present discussion to $n = 4, 6$, which implies that C_2 and $\mathcal{T}$ symmetry are also symmetries of the system.

In the following we use symmetry indicators to derive constraints on the corner charges due to a nontrivial 2SW class. We adopt the notation of Ref. [28], where the eigenvalues of the C_n-rotation operator at the C_n-symmetric HSP Π for spinless particles are denoted by

$$\Pi_p^{(n)} = e^{2\pi i(p-1)/n}, \quad p = 1, 2, \ldots, n \tag{2}$$

and define the quantities

$$\left[\Pi_p^{(n)}\right] = \#\Pi_p^{(n)} - \#\Gamma_p^{(n)}, \tag{3}$$

where $\#\Pi_p^{(n)}$ and $\#\Gamma_p^{(n)}$ are the number of occupied energy bands with eigenvalue $\Pi_p^{(n)}$ at HSPs Π and Γ, respectively. For C_4 we have HSPs Γ, X, and M, while for C_6 they are Γ, M, and K. Then, assuming the specific geometries of the 2D crystals shown in Fig. 7(a), the corner charges are given by [30]

$$Q_{\llcorner}^{(4)} = \frac{e}{4}\left(\mp\left[X_1^{(2)}\right] + 2\left[M_1^{(4)}\right] + 3\left[M_2^{(4)}\right]\right) \mod e, \tag{4a}$$

$$Q_{\llcorner}^{(6)} = \frac{e}{4}\left[M_1^{(2)}\right] + \frac{e}{6}\left[K_1^{(3)}\right] \mod e, \tag{4b}$$

where $e < 0$ is the electron charge and the sign in front of $[X_1^{(2)}]$ depends on whether the center of the C_4-symmetric crystal is located at Wyckoff position $1a$ (upper sign) or $1b$ (lower sign). Note that, consistent with the assumptions in the present discussion, Eq. (4) assumes the presence of time-reversal symmetry $\mathcal{T}$ with $\mathcal{T}^2 = +\mathbb{1}$; if $\mathcal{T}$ is not a symmetry, Eqs. (A2) and (A3) should be used instead.

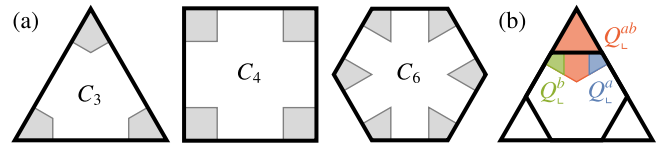

FIG. 7. (a) The C_n-symmetric cross-section geometries for which the hinge charges are defined, and for which the values listed in Table II apply. The corners (gray regions) in the cross sections correspond to the hinges in the 3D system. (b) Deformation of the C_6-symmetric sample (inner hexagon) to a C_3-symmetric sample (outer triangle). Two corners (blue and green) of the hexagon with corner charges $Q_{\llcorner}^{a}$ and $Q_{\llcorner}^{b}$ merge into a single corner (red) of the triangle with corner charge $Q_{\llcorner}^{ab} = Q_{\llcorner}^{a} + Q_{\llcorner}^{b}$.

Since both C_4 and C_6 symmetries imply the presence of C_2 symmetry, we can also consider the symmetry-indicator formula for the 2SW class [70], namely,

$$w_2 = \sum_{\Pi \in \mathrm{TRIM}} \left\lfloor \frac{1}{2}\#\Pi_2^{(2)} \right\rfloor \mod 2, \tag{5}$$

where the sum is over the four time-reversal-invariant momenta (TRIM) in the BZ (these are exactly the C_2-invariant momenta) and $\lfloor\cdot\rfloor$ is the floor function. In Appendix A 2 we show that in the presence of an enlarged rotational symmetry, the 2SW class can be equivalently written as

$$C_4: \quad w_2 = \left[M_2^{(4)}\right] \mod 2, \tag{6a}$$

$$C_6: \quad w_2 = \frac{1}{2}\left[M_1^{(2)}\right] \mod 2, \tag{6b}$$

where on the right-hand side we used the same C_n symmetry indicators that also enter Eq. (4).

Finally, we observe that for vanishing polarization, the 2SW class constrains the corner charge. For $n = 4$ the polarization vanishes if and only if $[X_1^{(2)}] = 0 \mod 2$, while for $n = 6$ it always vanishes [28]. Therefore, vanishing polarization also implies that the center-dependent sign ambiguity in Eq. (4a) drops from our analysis. Combining the assumption of vanishing polarization with Eqs. (4) and (6), we show in Appendix A 2 that the nontrivial value $w_2 = 1$ constrains the corner charge for C_4-symmetric SWIs to

$$Q_{\llcorner}^{(4)} \in \left\{\pm\frac{e}{4}\right\} \mod e \tag{7a}$$

and for C_6-symmetric SWIs to

$$Q_{\llcorner}^{(6)} \in \left\{\pm\frac{e}{6}, \frac{e}{2}\right\} \mod e, \tag{7b}$$

i.e., to *odd* multiples of $\frac{e}{n}$, whereas the complementary fractional values correspond to insulators with $w_2 = 0$.

Before applying the presented formulas to study TPPs in 3D, we briefly comment on some relations of the result in Eq. (7) to previous works. First, note that in the presence of chiral symmetry, the corner charge can only attain value 0 or $\frac{e}{2} \mod e$. This can be easily understood as follows. If the occupied states carry localized corner charge $Q \mod e$, then (by completeness of the Hilbert space) the unoccupied states carry localized corner charge $-Q \mod e$. Chiral symmetry is local in real space and maps occupied onto unoccupied states, therefore guaranteeing that $Q = -Q \mod e$.

That equation has two solutions: $Q = 0, \frac{e}{2} \mod e$. On the other hand, our derivation in Appendix A 2 reveals that the value $w_2 = 1$ can result in corner charge $Q_\llcorner^{(6)} = \frac{e}{2} \mod e$ if and only if $[K_1^{(3)}] = 0 \mod 6$. This is compatible with the finding of Ref. [76] which showed that chiral symmetry that commutes with C_3 rotation implies $[K_1^{(3)}] = 0$. The value $\frac{e}{2}$ mod e of the corner charge was also reported in the study of a SWI model with chiral and C_6 symmetry by Ref. [19]. Second, the result in Eq. (7a) implies that the three conditions (1) C_4 symmetry, (2) $w_2 = 1$, and (3) vanishing polarization are incompatible with (4) the presence of chiral symmetry; equivalently, SWI with chiral and C_4 symmetries must necessarily have gapless edges. This finding is compatible with the observations of Ref. [48] made in the context of second-order NL semimetals.

B. Euler monopole charge in presence of rotational symmetry

If the two occupied bands involved in the TPP formation are separated from lower-lying occupied bands by an energy gap, the 2SW can be refined to the Euler monopole charge. Note that this is a different situation from the one discussed in Sec. III B: here we consider a surface enclosing a TPP, i.e., two TPs in adjacent band gaps, as shown in Fig. 3(b). Monopole charges such as the 2SW and the Euler monopole charge can be inferred from the winding of the Wilson-loop spectrum. Symmetries constrain the latter [33,77,78] and therefore lead to symmetry-indicator formulas for the monopole charges. To our knowledge, no such symmetry-indicator formulas for the Euler monopole charge in the presence of rotational symmetry have been previously derived, therefore, we do that here. Along the way, we identify that TPPs formed by certain combinations of ICRs are necessarily associated with extended NLs in the principal gap, which prevents the system from exhibiting higher-order topological signatures and the monopole charge from being defined. The details of these derivations are relegated to Appendix B, while here we only outline the main steps and results.

To derive the symmetry-indicator formulas, we consider a spherical surface enclosing part of a HSL with C_n rotational symmetry in its little cogroup, e.g., containing a TPP, as illustrated in Fig. 8(a). We refer to the two points where the sphere is intersected by the rotation axis as the south and north pole. Let N and N_{occ} be the total number of bands and the number of occupied bands, respectively. We assume the system to have space-time inversion symmetry $\mathcal{PT}$ satisfying $(\mathcal{PT})^2 = +\mathbb{1}$, such that there is a basis in which the corepresentation of $\mathcal{PT}$ is the identity matrix and the Bloch Hamiltonian a real symmetric matrix. Let further D_0 and D_1 label the symmetry representations of the occupied bands in that basis at the south and north poles of the spherical surface, respectively. In Appendix B 1 we show that the Wilson-loop operator $\mathcal{W}(\phi)$ computed on the path

$$\Gamma(\phi) = \gamma(\phi)^{-1} \circ \gamma(0) \tag{8}$$

illustrated in green in Fig. 8(a) is constrained by C_n symmetry:

$$\mathcal{W}\left(\phi + \frac{2\pi}{n}\right) = D_0(C_n) P(\phi)^\dagger D_1(C_n)^\dagger P(\phi) \mathcal{W}(\phi), \tag{9}$$

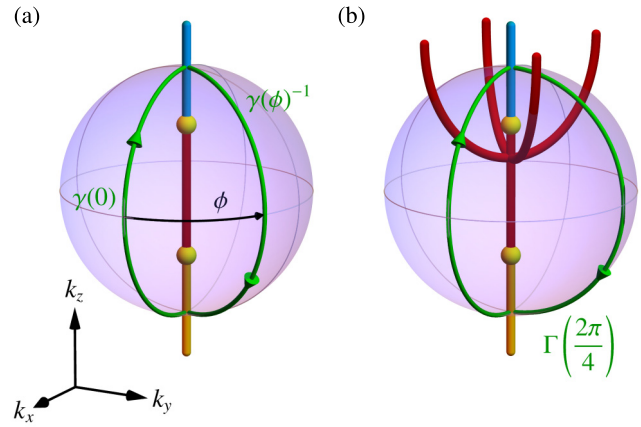

FIG. 8. (a) Definition of the closed contours $\Gamma(\phi) = \gamma(\phi)^{-1} \circ \gamma(0)$ (green) on which the Wilson-loop operator $\mathcal{W}(\phi)$ is computed. The spherical surface (purple) is covered by these contours as the argument is increased in the range $\phi \in [0, 2\pi)$. If the surface is not crossed by any other nodal lines (NLs) than the orange and blue ones, the Euler monopole charge χ can be defined and is determined by the winding of the Wilson-loop spectrum. This is the case, for example, if there are no red nexus points enclosed in the surface. (b) In other cases, e.g., if there is exactly one red nexus point enclosed, red NLs crossing the surface are *always* present. This is indicated by a π Berry phase on the path $\Gamma(2\pi/n)$, where n is the order of the rotational symmetry. The nontrivial Berry phase implies that $\Gamma(2\pi/n)$ encircles an odd number of NLs in the principal gap (red NLs), as illustrated.

where $P(\phi) \in \mathsf{SO}(N_{\mathrm{occ}})$ is defined by parallel transport [see Eq. (B17) in Appendix B 1]. Note that in Eq. (8), one first traverses the path appearing to the right of the composition symbol "$\circ$."

For arbitrary N_{occ}, we consider the implication of Eq. (9) for the Berry phase of the occupied bands on the contours $\Gamma(\phi)$. The Berry phase is given by $\varphi = \arg\det \mathcal{W}$ [79], such that

$$\varphi\left(\phi + \frac{2\pi}{n}\right) = \varphi(\phi) + \arg\det[D_0(C_n) D_1(C_n)^\dagger] \mod 2\pi. \tag{10}$$

Due to $\mathcal{PT}$ symmetry, $\Delta\varphi = \arg\det[D_0(C_n) D_1(C_n)^\dagger]$ is quantized to 0 vs π. If $\Delta\varphi = \pi$, there are an odd number of NLs in the principal gap crossing the surface in each sector $[\phi, \phi + 2\pi/n]$ [cf. Fig. 8(b)]. This implies that the principal gap is necessarily closed somewhere on the enclosing surface, thus preventing one from assigning a monopole charge to the enclosed TPP. We will see in Sec. IV C that this condition also prevents the corresponding TPPs from exhibiting the higher-order signature at the hinges.

In the remainder of this subsection, we call a TPP *admissible* when the principal gap on the enclosing sphere can be open. This corresponds to the case with $\Delta\varphi = 0$, which is equivalent to requiring

$$\det[D_0(C_n) D_1(C_n)^\dagger] = 1. \tag{11}$$

By our initial assumption, the two occupied bands involved in the TPP are separated from lower-lying occupied bands by an energy gap on the whole surface, such that we can ignore

TABLE II. Bulk-hinge correspondence for triple-point pairs (TPPs) in spinless systems. Triple points (TPs) can arise only in crystals with rotational symmetry C_n (or screw symmetry) of order $n \in \{2, 3, 4, 6\}$; this fixes the nanowire geometry (see table footnote a) in which we study the hinge charges. In particular, the TPs occur along high-symmetry lines (HSLs) with little cogroup (LCG) that has the same rotational symmetry C_n supplemented with space-time inversion ($\mathcal{PT}$) symmetry *or* with mirror (m_v) symmetry with respect to plane that contains the HSL *or* with both $\mathcal{PT}$ and m_v. Note that C_n may be generated by an antiunitary rotational symmetry $C_{n/2}\mathcal{PT}$ for even n, and that the antiunitary rotations $C_4\mathcal{PT}$ and $C_6\mathcal{PT}$ can stabilize TPs even without additional symmetries. (For an easily navigable summary of all admissible symmetry combinations supporting spinless TPs, see Table I.) In the second row we indicate representative HSLs with the required rotational symmetry, which are realized in SGs with a prismatic Brillouin zone (however, the below-listed values of $\Delta Q_{\llcorner}$, χ, and w_2 apply equally to all HSLs with the specified symmetry). In the third row we indicate the generator of the LCG rotational symmetry, i.e., the maximal (unitary or antiunitary) rotational symmetry. The next row lists the possible pairs of TP types along the corresponding HSL which can exhibit a gapped spectrum on both sides of the NL segment (cf. Fig. 10); for the classification of *individual* TPs in spinless systems into type A vs type B, see Table I or Ref. [59]. The row labeled by "ICRs" indicates the possible triplets of irreducible corepresentations of the LCG which can form a four-band TPP (cf. Fig. 9); "any" means that all combinations of a 2D ICR with two 1D ICRs give the same result. The notation for the ICRs follows Ref. [65], where we drop the subscripts if they do not affect the result. Note that for the 2D ICRs of $6/m'$ we define ${}^2E_2\,{}^1E_2 \mapsto E_1$ and ${}^2E_1\,{}^1E_1 \mapsto E_2$. Finally, we find that *each* TPP is characterized by a fractional hinge-charge jump $\Delta Q_{\llcorner}$. If $\mathcal{PT}$ symmetry is present, we also assign the TPPs the Euler $|\chi|$ and second Stiefel-Whitney w_2 monopole charges. The hinge charges $Q_{\llcorner}$ are computed for the geometries depicted in Fig. 7(a).

Rotational symmetry	C_2[a]	C_3		C_4		C_6	
Example HSLs	$\Gamma Z, MA$	$\Gamma A, KH, K'H'$		$\Gamma Z, MA$	KH[b]	ΓA	
LCG rotation generator	$C_4\mathcal{PT}$	C_3	$C_6\mathcal{PT}$[a]	C_4	C_3	C_6	
TP types	(A, A)	(B, B)	(A, A)	(A, A)	(B, B)	(A, A)	(B, B)
ICRs	Any	Any		$(E;A,A)$ $(E;B,B)$	Any	$(E_1;A,A)$ $(E_2;B,B)$	$(E_1;B,B)$ $(E_2;A,A)$
$\Delta Q_{\llcorner} \mod e$	$\frac{e}{2}$	$+\frac{e}{3}$		$+\frac{e}{4}$	$+\frac{e}{3}$	$+\frac{e}{6}$	$-\frac{e}{3}$
$\lvert\chi \mod n\rvert$[d]	–	1	–	1	2	1	2
w_2	–	0 or 1[c]	–	1	0	1	0

[a]For $C_4\mathcal{PT}$ (without additional $\mathcal{PT}$), the largest unitary rotational symmetry is C_2. Then, we consider a square geometry, and the quantization of the hinge-charge jump to $\frac{e}{2} \mod e$ occurs only if summing over two neighboring hinges. For $C_6\mathcal{PT}$ we consider the C_3 (triangular) geometry.
[b]Due to the double occurrence of the KH line in a C_6-symmetric system, the Brillouin zone exhibits two TPPs at the same value of k_z. The indicated values of $\Delta Q_{\llcorner}$ and w_2 represent the combined contribution of *both* of them.
[c]Here, the second Stiefel-Whitney monopole is not symmetry indicated and both options are possible. For an example of each, see Sec. V D.
[d]Here we use the convention that $a \mod n \in (-\lfloor n/2\rfloor, \ldots, \lfloor n/2\rfloor]$, such that $|a \mod n| \in \{0, 1, \ldots, \lfloor n/2\rfloor\}$. This implies that for $n = 6$ the value 4 (5) is equivalent to 2 (1), for $n = 4$ the value 3 is equivalent to 1 and for $n = 3$ only 0,1 can be distinguished (with 2 equivalent to 1 and therefore with undetermined parity). For further clarification of the ambiguity involved in defining $|\chi| \mod n$, see Appendix B 4.

the lower-lying bands and set $N_{\mathrm{occ}} = 2$. Then, the absence of nodes in the principal gap implies that the Euler monopole charge on the sphere is well defined and given by the winding number of the Pfaffian of the logarithm of $\mathcal{W}(\phi)$ [73]. In Appendix B 3, we show that if $D_0(C_n), D_1(C_n) \in \mathsf{SO}(2)$, then Eq. (9) simplifies to

$$\mathcal{W}\left(\phi + \frac{2\pi}{n}\right) = D_0(C_n)\; D_1(C_n)^{\dagger}\mathcal{W}(\phi). \tag{12}$$

Since the nth power of $D_{0,1}(C_n)$ gives the identity, it follows that for $j \in \{0, 1\}$: $D_j(C_n) = e^{-\frac{2\pi i}{n} r_j s_y}$ with $r_j \in \mathbb{Z}$ and the Pauli matrix s_y acting on the space of the two valence bands. Then, we extract the following symmetry-indicator formula for the Euler monopole charge χ:

$$\chi = r_1 - r_0 \mod n. \tag{13}$$

Note that χ is only gauge invariant up to sign and that the relevant topological invariant therefore is $|\chi|$.

C. Triple-point configurations with hinge charges

In this section we apply the symmetry-indicator formulas from Secs. IV A and IV B to study four-band TPP configurations in $\mathcal{PT}$-symmetric systems. While in Sec. III A we have assumed the TPPs to be demarcated by type-A TPs, we here generalize to the case of both type-A and type-B TPs. Our result, summarized by Table II, provides the complete correspondence between TPPs, their 2SW and Euler monopole charge (if they are defined), and the higher-order signature in the fractional hinge charge. For simplicity, we first focus on TPs in crystals with a symmorphic SG and generalize the results to nonsymmorphic SGs in Sec. VII.

Our analysis is structured as follows. First, based on the classification result of Refs. [59,60], we know that TPs can be stabilized in spinless systems on HSLs with trigonal, tetragonal, or hexagonal symmetry (cf. Table I). Such HSLs arise in SGs with the corresponding symmetry. For crystals with C_n symmetry, where $n \in \{2, 3, 4, 6\}$, some representative HSLs with the specified symmetry (namely, ones that are realized in SGs with prismatic BZs), are listed at the top of Table II (however, the derived bulk-hinge correspondence, encoded by $\Delta Q_{\llcorner}$, χ, and w_2, applies equally to *all* HSLs with the prescribed symmetry). Then, given the little cogroup of any such HSL, we consider all possible combinations of ICRs leading to TPPs. Recall that a TPP requires a 2D ICR ($\rho^{2\mathrm{D}}$) to be crossed consecutively by two 1D ICRs ($\rho_a^{1\mathrm{D}}$ and $\rho_b^{1\mathrm{D}}$) (cf. Fig. 9), and can thus be characterized by the triplet ($\rho^{2\mathrm{D}}; \rho_a^{1\mathrm{D}}, \rho_b^{1\mathrm{D}}$) (here, the ordering of the 1D ICRs is

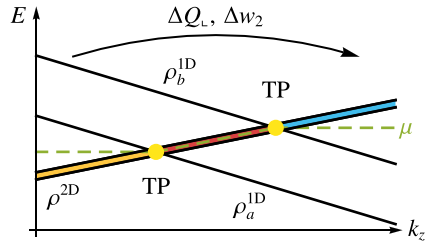

FIG. 9. Convention for defining the jump of the fractional hinge charge ($\Delta Q_{\llcorner}$) and of the second Stiefel-Whitney monopole (Δw_2) associated with a pair of triple points (TP, yellow dots) in a four-band configuration. The black lines indicate the band structure along a high-symmetry line, with the 2D irreducible corepresentation (ICR) ρ^{2D} passing from the bottom (orange) to the central (red) to the upper (blue) energy gap with increasing momentum k_z due to crossing two 1D ICRs ρ_a^{1D} and ρ_b^{1D}. The green dashed line (μ) indicates half-filling at various k_z. The quantities $\Delta Q_{\llcorner}$ and Δw_2 associated with the TP pair are defined as the characteristics of the 2D cut in the region where ρ^{2D} is unoccupied (i.e., above μ) from which we subtract the characteristics of the 2D cut in which ρ^{2D} is filled (i.e., below μ). In practice, the *physical* chemical potential has a value independent of momentum, and will therefore locally deviate from the μ defined above. Nevertheless, generically, the system will still be at half-filling for extended parts of the orange and blue regions which lie far enough from the TP pair. The differences $\Delta Q_{\llcorner}$ and Δw_2 are therefore still well defined and unchanged compared to the situation with variable $\mu(k_z)$.

unimportant). Finally, we apply the symmetry-indicator formulas from Secs. IV A and IV B to derive the higher-order bulk-boundary correspondence of TPPs, listed in the bottom of Table II.

Choosing k_z along the HSL and taking 2D cuts of the system at constant k_z, we obtain a series of 2D systems with Hamiltonian $\mathcal{H}_{k_z}(k_x, k_y)$, which we assume to be at half-filling. This fixes the principal gap to be the second one (such that principal nodes are indicated in red, cf. Fig. 9). Upon increasing k_z, the system goes from having ρ^{2D} occupied (to the left of the first TP) to instead having $(\rho_a^{1D}, \rho_b^{1D})$ occupied (to the right of the second TP). Let us refer to the three ranges of k_z separated by the two TPs by the corresponding color of the central NL as *orange*, *red*, and *blue* k_z range. The corresponding band inversions lead to changes in the symmetry indicators $\#\Pi_p^{(n)}$, and thus potentially alter both the corner charge [cf. Eq. (4)] and the 2SW class [cf. Eq. (6)] of the 2D cuts. Let us remark that, in practice, the *physical* chemical potential of the 3D system will be constant. However, generally it can be chosen such that we have half-filling with insulating bulk at least for some 2D cuts in the orange and blue k_z ranges; then, the jumps will be observable by comparing only k_z values corresponding to those cuts.

We briefly explain how to apply the 2D symmetry-indicator formulas to 3D systems with $\mathcal{PT}$ and arbitrary C_n symmetry. For concreteness we assume the rotation axis to be along k_z. In this case, any 2D cut perpendicular to k_z through the 3D BZ inherits both of these symmetries. In particular, within the 2D plane $\mathcal{PT}$ acts as $(C_2\mathcal{T})_{2D}$ with $(C_2)_{2D} = C_2$ being the rotation around the k_z axis, and $\mathcal{T}_{2D} = \mathcal{P}C_2\mathcal{T} = m_z\mathcal{T}$ [49] being the composition of the physical time-reversal symmetry with the horizontal mirror symmetry $m_z : z \mapsto -z$. Note that the HSPs entering the symmetry-indicator formulas need to be identified with the intersection of the corresponding HSLs in the 3D BZ with the chosen 2D plane at fixed k_z. For $\Pi^{(n)}$ we thus need to consider the C_n-invariant HSLs, while the 2D TRIM correspond to lines invariant under $\mathcal{T}_{2D}$. The computed corner charges in the 2D cuts therefore imply the corresponding values of hinge charges in the 1D hinge BZ, while the jump of the 2SW class between two 2D cuts corresponds to the 2SW *monopole charge* as we explained in Sec. III A and illustrated in Fig. 4.

The hinge charge is only well defined for values of k_z, where the bulk of $\mathcal{H}_{k_z}$ is gapped and the surface charge vanishes [28]. Similarly, the monopole charges are only well defined as long as there is a surface enclosing the TPP that is not penetrated by NLs in the principal gap (red). While these conditions generally depend on the model parameters, we can formulate the following criteria for a gapped bulk, which conversely implies constraints on the admissible TPP configurations (to be precise, we call a combination of a 2D and two 1D ICRs an *admissible TPP configuration* if it is *not* necessarily gapless in the orange or blue k_z range):

(1) In Sec. IV B we have discussed a condition [summarized by Eq. (11) and derived in Appendix B], that the representations of C_n in the orange and blue k_z ranges must necessarily fulfill in order for the TPP to be admissible. According to Fig. 9, we have $D_0(C_n) = \rho^{2D}(C_n)$ and $D_1(C_n) = \rho_a^{1D}(C_n) \oplus \rho_b^{1D}(C_n)$, such that the condition for the TPP configuration to be admissible is

$$\det \rho^{2D}(C_n) = \rho_a^{1D}(C_n)\rho_b^{1D}(C_n). \tag{14}$$

Note that this is fully determined by the rotation eigenvalues since the determinant on the left is just the product of eigenvalues. In Appendix B 4, we show that this excludes exactly the TPPs with two 1D ICRs that have different rotation eigenvalues, i.e., for the little cogroups $C_{4(v)}$ these are the combinations $(E; A, B)$ and for $C_{6(v)}$ the combinations $(E_i; A, B)$, $i = 1, 2$ (we have omitted subscripts of the 1D ICR labels since the argument is insensitive to them). In these cases neither the jump of the hinge charge nor the Euler and 2SW monopole charges are defined.

(2) For the little cogroup $C_{6(v)}$, the gaplessness can be understood from the NL structure implied [60] by the type of TPs involved, as illustrated in Fig. 10. A TPP consisting of one type-A and one type-B TP necessarily has NL arcs in the principal gap that extend beyond the red k_z range. In contrast, if both involved TPs are of the same type, the orange and the blue k_z ranges can generally be gapped. On the one hand, the case of two type-A TPs is very simple since there are no additional NLs and the bulk is gapped in the corresponding regions of k_z. On the other hand, for two type-B TPs there must be NL arcs in the principal band gap attached to both TPs. However, the NL arcs can tie the two TPs together in the red k_z range, where the gapless 2D cuts are not considered when analyzing the higher-order topology, thus leaving the orange and the blue k_z range gapped. Note that in the applicable case, i.e., $C_{6(v)}$ which are the only point groups where both types of TPs are possible, this criterion turns out to be equivalent to the first.

(3) While the above two points give necessary criteria for having a gapped bulk, they are not sufficient. Two type-A

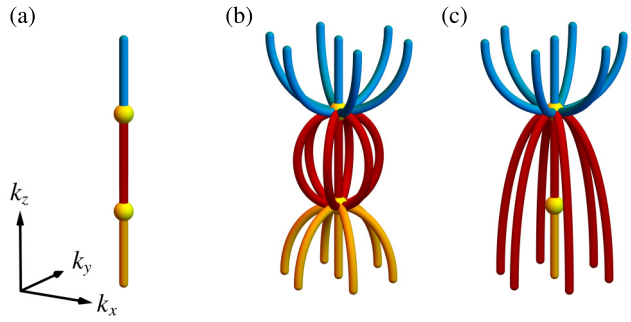

FIG. 10. Illustration of possible nodal-line (NL) compositions for the three considered triple-point pair configurations. (a) Two type-A triple points (TPs) have no attached NL arcs. (b) Two type-B TPs both exhibit attached NL arcs in the principal gap (red), but these NLs *can* compactly tie the two TPs together, leaving the 2D bulk gapped in both the orange and in the blue k_z range. (c) If one of the TPs is type A and the other type B, the NL arcs in the principal gap *necessarily* cross into either the orange or into the blue k_z range, making the corresponding 2D cuts gapless.

TPs do not have any NL arcs attached, but they are often accompanied by nexus points, i.e., points on the HSL away from the TPs where NL arcs coalesce [59] [see Figs. 11(a) and 11(b)]. If there are an even number of nexus points in the principal gap, then there are two options: (a) the NL arcs connect together through the red k_z range or (b) the NL arcs extend *outside* the red k_z range, making the orange and blue k_z ranges gapless. These two cases are illustrated in Figs. 11(a) and 11(b), respectively, for a C_4-symmetric example. Similarly, the NL arcs of two type-B TPs might not connect through the

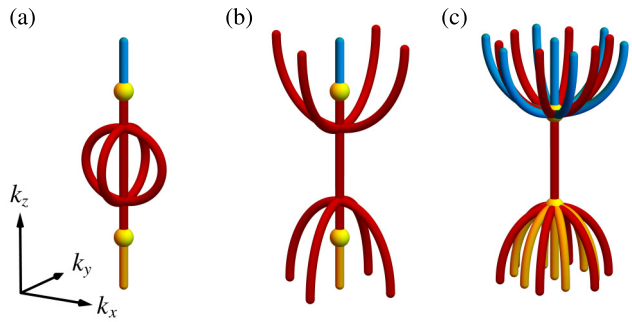

FIG. 11. Illustration of certain more intricate nodal-line (NL) compositions which can also arise near triple-point pairs (TPPs). (a) Type-(A, A) TPP with two red nexus points whose NLs are tied together *inside* the red k_z range, leaving the 2D bulk gapped in both the orange and in the blue k_z range despite the nexus points. Here, both the monopole charges and the hinge-charge jump can be defined. (b) Analogous situation as in the previous panel; however, here the NLs extend into the orange and blue k_z ranges rendering the corresponding 2D cuts gapless. In this case, neither the monopole charges nor the hinge-charge jump can be defined. (c) Type-(B, B) TPP with NL arcs extending *outside* the red k_z range, making the relevant 2D cuts gapless. The monopole charges and the hinge-charge jump are undefined. This scenario should be contrasted to Fig. 10(b), which shows a similar situation with the NL arcs tied together *inside* the red k_z range.

red k_z range as indicated in Fig. 10(b) but rather extend outside of it as shown in Fig. 11(c). These cases are *not* distinguished by symmetry properties but by the model parameters. The results of our analysis, e.g., Table II, apply to the cases that do have a gapped bulk in some part of both the orange and the blue k_z ranges.

Let us remark that the cases disallowed by the first criterion 1 for point group $C_{4(v)}$ (which according to Table I involve a pair of type-A TPs) correspond to situations where there is one (or a larger odd number of) symmetry-imposed nexus points of NLs in the principal gap, i.e., with the NLs attaching to the red region demarcated by the two TPs. An example of such a TPP configuration is illustrated in Fig. 8(b). Since an odd number of nexus points cannot be paired as in Fig. 11(a), there necessarily exist extended NLs which render either the orange or the blue k_z region gapless. Therefore, the corresponding TPP is not admissible for the same reason as is visualized for the mixed-type TPP in Fig. 10(c).

Having clarified the necessary conditions to realize an admissible TPP, let us tackle their associated hinge-charge jump. To observe the hinge charge, the system needs to be extended in the z direction and finite in the x and y directions, with a geometry possessing the same C_n symmetry as the SG [see Fig. 7(a)]. We need to distinguish geometries with the center of the rotational symmetry being placed at different WPs in the unit cell. In Appendix A 3 we consider all possible cases for each combination of ICRs listed in Table II and compute the hinge-charge jump using the appropriate symmetry-indicator formulas [30] [in particular, aside from Eqs. (4a) and (4b), we also need the analogous expression for $Q_{\llcorner}^{(3)}$; see Eq. (A1)]. Note that for this analysis the ionic charge distribution is irrelevant because it does not depend on k_z and therefore it does not contribute to the *jump* of the hinge charge. Table II summarizes the results of this analysis. We observe that the combination of ICRs uniquely determines the jump of the hinge charge. In particular, there is a nonvanishing jump $\Delta Q_{\llcorner} \neq 0 \mod e$ quantized into multiples of $\frac{e}{n}$ for C_n symmetry for any TPP.

Let us briefly comment on the jump of the *surface* charge. As already stated, the vanishing of the fractional part of the surface charge (which is related to bulk polarization [80]) is a necessary condition for the hinge charge to be observable [28]. Therefore, to observe the hinge-charge *jump*, the surface charge must vanish for the k_z ranges on *both* sides of the TPP, which can only happen if the TPP is not associated with a fractional jump $\Delta\mathbf{P}$ of the 2D bulk polarization. We present in Appendix A 3 a derivation, based on the symmetry-indicator formulas for the 2D polarization [28–30], showing that indeed $\Delta\mathbf{P} = 0 \mod e\mathbf{R}$ (where the Bravais vectors $\mathbf{R}$ constitute the usual ambiguity of bulk polarization [81]) for all tabulated TPPs. Therefore, the surface charge does not present an obstacle for the definition of the hinge charges, and we expect the hinge-charge jump to be observable for an appropriate choice of the boundary termination.

To compute the jump of the 2SW class, or equivalently the 2SW monopole charge $w_2 = \Delta w_2$ carried by the red NL segment, we proceed as follows. For systems with C_4 or C_6 symmetry the 2SW class of the 2D cuts can be computed readily by applying Eq. (6) with the appropriate interpretation of the HSPs, as described above. The full derivation can be

found in Appendix A 3 and the results are displayed in the bottom-most row of Table II. Consistent with the results of Sec. III A, we find that type-(A, A) TPPs in $\mathcal{PT}$-symmetric systems universally carry $w_2 = 1$. Furthermore, we recognize the following correspondence principle between the bulk invariant w_2 and the hinge signature $\Delta Q_{\llcorner}$ (which is only defined modulo e): a nontrivial 2SW monopole charge $w_2 = 1$ implies a fractional hinge-charge jump of the minimal nonvanishing magnitude $|\Delta Q_{\llcorner}| = \frac{e}{n}$, while $w_2 = 0$ results in a twice as large a jump $|\Delta Q_{\llcorner}| = \frac{2e}{n}$.

Determining the 2SW monopole charge in the case of C_3 symmetry is not as straightforward. However, we note that the 2SW monopole charge is attributed to the red NL segment along the HSL as illustrated in Fig. 3(b) and is therefore a feature local in k_x, k_y. Thus, it cannot depend on the specific choice of HSL in the BZ, but only on the Hamiltonian near the HSL. Noting that the little cogroup of all three HSLs has the same rotational symmetry and there is only one class of combinations of ICRs, the admissible values of the 2SW monopole charge w_2 are the same for all three HSLs ΓA, KH, and $K'H'$. In the next paragraph we argue that, in fact, the 2SW class is not symmetry indicated in the C_3-symmetric case, meaning that both $w_2 = 0$ or 1 are possible. We emphasize that this is not in contradiction to the bulk-hinge correspondence principle described above because the fractional part of the hinge-charge jump satisfies $\pm\frac{e}{3} = \mp\frac{2e}{3} \mod e$. Thus, the hinge signatures of nontrivial and trivial 2SW monopole charge become indistinguishable.

The fact that the 2SW class is not symmetry indicated in a SG with C_3 symmetry can be easily deduced from the other results in Table II. In particular, note that a SG with C_6 symmetry also has C_3 symmetry. Thus, we can deform any of the possible TPP configurations on the ΓA line of a sixfold-symmetric system (cf. last two columns of Table II), having either $w_2 = 0$ or 1, into a TPP configuration of a C_3-symmetric system by introducing a small C_2-breaking perturbation. However, Table II shows that in the in threefold-symmetric little cogroups, only a single combination of ICRs is possible, such that any initial choice of the TPP in the C_6-symmetric case results in that unique TPP type of the C_3-symmetric system (in particular, type-A TPs generically transform into type-B TPs). Since the 2SW class requires only $\mathcal{PT}$ symmetry (which is preserved when breaking C_2) and the 2D cuts outside the red k_z range remain gapped under the addition of a small perturbation, the 2SW class is unaffected by the perturbation. This implies that both $w_2 = 0$ or 1 are possible for TPPs in C_3-symmetric SGs, and that the 2SW class is not symmetry indicated. We demonstrate this feature for two explicit models in Sec. V D.

The symmetry-indicator formula for the Euler class, Eq. (13), is, in contrast to the other formulas, already formulated in 3D. It involves the corepresentations of C_n in the orange and blue k_z ranges. By going through all allowed combinations of ICRs (cf. Appendix B 4), we verify that indeed $\rho^{2D}(C_n)$ and $\rho_a^{1D}(C_n) \oplus \rho_b^{1D}(C_n)$ are SO(2) matrices; then we extract $r_0 = r_{2D}$, $r_1 = r_{1D+1D}$ and compute χ. The results are shown in the second to last row of Table II for the cases with $\mathcal{PT}$ symmetry. We observe that in *all* cases where it is defined, the Euler monopole charge is nontrivial and consistent with the independently calculated w_2, via the relation $w_2 = \chi \mod 2$. Note that for $n = 3$, χ is determined only modulo 3 and thus has undetermined parity, which is consistent with the 2SW not being symmetry indicated in that case (cf. Sec. V D).

Finally, we remark on the consistency of the results in Table II for a TPP on the KH line of a C_6-symmetric compared to a C_3-symmetric system. Naturally, a system with sixfold rotational symmetry is also threefold rotation symmetric, such that one expects compatibility of the results for the two cases. However, there are two caveats: (1) in a C_6-symmetric system the KH and $K'H'$ HSLs are equivalent such that there are in fact *two* symmetry-related TPPs per BZ at the same value of k_z, and (2) the hinge-charge jumps in the two cases are computed for a *different geometry* of the sample [cf. Fig. 7(a)]. Therefore, if we only consider the C_3 symmetry of a C_6-symmetric system, we have to (1) count contributions of identical TPPs on the two HSLs KH and $K'H'$, and (2) deform the sample with hexagonal cross section into one with a triangular cross section by combining two corners into a single new corner as depicted in Fig. 7(b).

With this insight, it is easily checked that the corresponding entries in Table II are fully consistent. First, for the 2SW class the two monopole charge contributions are additive, $w_2^{(6)} = 2w_2^{(3)}$, which results in $w_2^{(6)} = 0 \mod 2$ for both $w_2^{(3)} = 0$ or 1. Furthermore, the corner charge of the triangular cross section $Q_{\llcorner}^{ab}$ is given by the sum of two of the corner charges of the hexagonal cross section $Q_{\llcorner}^{ab} = Q_{\llcorner}^{a} + Q_{\llcorner}^{b}$ [cf. Fig. 7(b)]. Note that due to the sixfold rotational symmetry $Q_{\llcorner}^{a} = Q_{\llcorner}^{b} = \frac{e}{3} \mod e$, such that for the C_6-symmetric model with a TPP on KH in the *triangular geometry* we find $Q_{\llcorner}^{ab} = 2\frac{e}{3}$. On the other hand, when interpreting the same model as being C_3 symmetric, we simply add the corner charges for a TPP on KH and $K'H'$, giving $Q_{\llcorner}^{ab} = 2\frac{e}{3}$ as well.

D. Effect of symmetry breaking

The discussion in Sec. IV C has focused on spinless systems with $\mathcal{PT}$ symmetry (corresponding to the MPGs in rows two and four of Table I), which has allowed us to characterize the TPPs with the Stiefel-Whitney monopole charge. However, stable TPPs can exist even when the $\mathcal{PT}$ symmetry is removed [59] (cf. Table I); in this case, the monopole charges cease to exist, but the bulk-hinge correspondence of the TPPs persists. In this section we discuss the effect of symmetry breaking on the derived bulk-hinge correspondence of TPPs. First, in Sec. IV D 1 we argue that the the hinge-charge jumps derived for the cases with m_v and $\mathcal{PT}$ symmetry still apply when the $\mathcal{PT}$ symmetry is broken while m_v remains present. We continue in Sec. IV D 2 with a discussion how the derived results generalize to the cases where the TPPs are protected by the antiunitary $C_n\mathcal{PT}$ rotational symmetry. Finally, in Sec. IV D 2 we briefly analyze the effect of breaking other combinations of symmetries, which generally leads to the loss of TPPs and to the formation of other species of band nodes. Our results are summarized in Table III.

1. Triple points protected by C_n and mirror symmetry

We first discuss the effect of breaking $\mathcal{PT}$ symmetry while keeping the rotational symmetry C_n. According to Table I, mirror symmetry m_v is then required to protect TPs. The crucial observation is that if both $\mathcal{PT}$ and mirror m_v sym-

TABLE III. Effect of symmetry breaking on triple-point pairs (TPPs). We initially consider TPPs in the combined presence of $\mathcal{PT}$ (space-time inversion), C_n (rotation of order $n \in \{3, 4, 6\}$), and m_v (vertical mirror) symmetries, corresponding to the first row of the table. Such TPPs are characterized by the second Stiefel-Whitney (2SW) monopole, by symmetry indicators ($\#\Pi_p^{(n)}$), and by the fractional hinge-charge jump (integer multiples of e/n). We then consider the breaking of the various symmetries, as analyzed in Sec. IV D. We find that TPPs can evolve into higher-order Weyl points (HO-Weyl), into nodal lines (NLs) with the 2SW monopole, or into Weyl points or nodal lines without higher-order topology (indicated as "various").

$\mathcal{PT}$	C_n	$C_n\mathcal{PT}$	m_v	Nodes	Bulk invariant	Hinge charge
√	√	√	(√)	TPPs	2SW, $\#\Pi_p^{(n)}$	$e/n\,\mathbb{Z}$
✗	√	✗	√	TPPs	$\#\Pi_p^{(n)}$	$e/n\,\mathbb{Z}$
✗	$C_{n/2}$[a]	√	(√)	TPPs	$\#\Pi_p^{(n)}$	$2e/n\,\mathbb{Z}$
√	✗	✗	(√)	NLs	2SW	Not quantized
✗	√	✗	✗	HO-Weyl	$\#\Pi_p^{(n)}$	$e/n\,\mathbb{Z}$
✗	✗	✗	(√)	(Various)	–	Not quantized

[a]The requirement of the presence of $C_{n/2}$ restricts n to 4,6.

metries are present in the little cogroup, then the ICRs are not modified by the removal of $\mathcal{PT}$ [82,83], i.e., the ICRs of the unitary symmetries of the full group are exactly given by the ICRs of the unitary subgroup. As a consequence, the classification of TPPs in systems with m_v symmetry based on ICRs is *identical* both with and without $\mathcal{PT}$ symmetry; in fact, detailed analysis [59] reveals that the *type* (A vs B) produced by the crossing of specified ICRs is also unaffected by the removal of $\mathcal{PT}$. An analogous statement also applies to the result that the ICR combination $(E; A, B)$ is necessarily gapless (see Appendix B 5).

To derive the hinge-charge jumps $\Delta Q_{\llcorner}$ associated with TPPs protected by m_v symmetry without $\mathcal{PT}$, we should, in principle, repeat the above-described analysis (detailed in Appendix A 3) with the symmetry-indicator formulas that do not assume time-reversal symmetry, i.e., (A1)–(A3), and the ICRs of the point groups without $\mathcal{PT}$ symmetry. However, as described in the previous paragraph, the ICRs (and therefore the rotation eigenvalues) are identical to the ICRs of the corresponding point groups *with* $\mathcal{PT}$ symmetry, such that Eqs. (A2) and (A3) still simplify to Eqs. (A4) and (A5). This implies that the jumps in the symmetry indicators are not changed when breaking $\mathcal{PT}$ symmetry while keeping the rotational symmetry C_n, and the hinge-charge jumps $\Delta Q_{\llcorner}$ remain unaltered as well. On the other hand, the monopole charges are not defined in the absence of $\mathcal{PT}$ symmetry. Therefore, all results in Table II except for the last two rows apply to systems with mirror m_v symmetry but no $\mathcal{PT}$ symmetry.

2. Triple points protected by the antiunitary $C_n\mathcal{PT}$ symmetry

Since TPs can also be protected by the antiunitary rotational symmetry $C_n\mathcal{PT}$ (cf. Table I), $\mathcal{PT}$ symmetry can alternatively be broken while keeping $C_n\mathcal{PT}$. In such a case, the C_n rotational symmetry is broken, while $C_{n/2} = (C_n\mathcal{PT})^2$ is a symmetry of the system. We have to distinguish two scenarios: the TPs are either protected by $C_6\mathcal{PT}$ or by $C_4\mathcal{PT}$. Note that, as we discuss in Appendix B 5, Eq. (14) still applies in these MPGs, yet a careful analysis reveals that this constraint does not imply the inadmissibility of any TPP configurations.

We begin with analyzing the case of $C_6\mathcal{PT}$, where the largest remaining rotational symmetry is C_3; therefore, a triangular geometry needs to be considered and the relevant rotational symmetry quantizing the hinge charges is C_3. Furthermore, we find [82,83] that the corresponding MPGs with and without m_v symmetry ($\bar{6}'m2'$ and $\bar{6}'$, respectively) have the same unitary subgroup as the $\mathcal{PT}$-symmetric MPGs $\bar{3}'m$ and $\bar{3}'$, respectively, with matching ICRs. As a consequence, the hinge-charge jump is the same as for the other little cogroups with C_3 rotational symmetry, i.e., no change in the bulk-boundary correspondence. This has motivated us to group C_3 and $C_6\mathcal{PT}$ within a single column of Table II. We remark, however, that although the ICRs of the subgroup and the higher-order bulk-boundary correspondence are equivalent to the C_3 case, this is not true for the corresponding TP types, which depend on the ICRs of the full point group. Irrespective of the presence (MPG $\bar{6}'m2'$) vs absence (MPG $\bar{6}'$) of m_v symmetry, the TPs protected by $C_6\mathcal{PT}$ are *always* type A [59]. In the latter case, this simply follows from the absence of symmetries (no m_v and no $\mathcal{PT}$) that can protect NLs lying off the rotation axis, while in the former this requires a more in-depth analysis [59].

Similarly, C_4 and $\mathcal{PT}$ can be broken while keeping $C_4\mathcal{PT}$. However, in that case the largest remaining rotational symmetry is C_2, such that in a square geometry only the *sum* over two adjacent hinges gives a quantized charge [28]. The resulting little cogroups are the MPGs $\bar{4}'2'm$ (with m_v mirrors) and $\bar{4}'$ (without m_v mirrors), which are subgroups of the $\mathcal{PT}$-symmetric MPGs $4/m'mm$ and $4/m'$, respectively. It is easily verified [82,83] that all four listed MPGs have equivalent C_2-rotation eigenvalues for the 1D and 2D ICRs: all 1D ICRs are *even* while all 2D ICRs are *odd* under C_2. Since in the presence of $C_4\mathcal{PT}$ the hinge-charge jump is completely determined by C_2-rotation eigenvalues, the hinge-charge jump of TPPs protected by $C_4\mathcal{PT}$ is, in principle, the same as in the C_4 case. However, since only the sum of charges on two adjacent hinges is quantized, the resulting jump is doubled to $\Delta Q_{\llcorner} = 2 \times \frac{e}{4} \mod e = \frac{e}{2} \mod e$. The TPs protected by $C_4\mathcal{PT}$ are always type A [59], i.e., of the same type as before the $\mathcal{PT}$ breaking. With this analysis, we explained the "C_2" column in Table II, and established the higher-order bulk-boundary correspondence for all TPPs listed in Table I.

3. Breaking the symmetry protection of triple points

Aside from breaking the symmetry in ways that keep the TPs robust, here we briefly discuss the effect of breaking symmetries that protect the TPs. We find that this generically results in the conversion of the TPs to other species of band nodes [84]. The case of broken C_n symmetry (with or without m_v) in the presence of $\mathcal{PT}$ symmetry has already been discussed implicitly in Sec. III A for type-(A, A) TPPs, where we revealed their conversion [60] into multiband nodal links carrying a nontrivial 2SW monopole. Using the results in Table II, we can now extend this discussion to generic TPPs. If the TPP carries $w_2 = 1$, then the 2SW monopole implies stable multiband nodal links upon breaking the rota-

tional symmetry. On the other hand, note that $w_2 = 0$ only arises for type-(B, B) TPPs. Since these are characterized by the attached NL arcs carrying a π flux of Berry phase [85], and this quantization is unaffected by the broken rotational symmetry, a small C_n-breaking perturbation leaves behind a NL composition with a trivial 2SW monopole. In both cases, $w_2 \in \{0, 1\}$, the absence of rotational symmetry implies the *absence* of the hinge-charge quantization for all geometries depicted in Fig. 7.

We next analyze the situation where C_n is kept but both m_v and $\mathcal{PT}$ are broken. In such cases, the rotational symmetry ensures that the quantized hinge-charge jump associated with the TPP is maintained. At the same time, it is impossible to protect NLs (including the 2D ICR along the HSL) without $\mathcal{PT}$ and m_v [86] using C_n alone, and instead Weyl points [87] become the generic band degeneracy. Therefore, the breaking of both m_v and $\mathcal{PT}$ symmetry results in a *higher-order Weyl semimetal* with Weyl points along the rotation axis [40–42], characterized by quantized hinge-charge jumps.

We remark that in spinless systems higher-order *Dirac* points [9,45–47] cannot be obtained by perturbing a TPP; and vice versa, a TPP cannot be created by perturbing a higher-order Dirac point. Nonetheless, the results in Table II readily generalize to include the higher-order Dirac points that are realized in C_6-symmetric models by crossing two different 2D ICRs [47]. Indicating such a crossing as $(E_1; E_2)$, we formally write $(E_1; E_2) \sim (E_1; \rho_a^{1D}, \rho_b^{1D}) - (E_2; \rho_a^{1D}, \rho_b^{1D})$. This equation represents the fact that the two pairs of TPPs can be evolved into the higher-order Dirac point: to see this, assume that along k_z the two 1D ICRs (for simplicity dispersionless) are first crossed by a 2D ICR E_1 with increasing energy and subsequently by 2D ICR E_2 with decreasing energy. By shifting the energy of the dispersionless 1D ICRs to higher values, the nodal feature at half-filling indeed evolves from two TPPs into a single Dirac point. However, this continuous change preserves the total topological characterization of the band nodes, therefore (cf. Table II) we deduce that the higher-order Dirac point is characterized by hinge-charge jump $\Delta Q_{\llcorner}^{(6)} = \frac{e}{6} - (-\frac{e}{3}) = \frac{e}{2} \mod e$ and by a nontrivial Stiefel-Whitney monopole $w_2 = 1 - 0 = 1 \mod 2$.

Finally, if C_n and $\mathcal{PT}$ are broken and only m_v is kept, then both the 2SW as well as the rotational symmetry indicators become invalid. As a consequence, no higher-order topology remains. Depending on the details of the perturbation, the m_v symmetry could leave behind mirror-protected NLs or the system opens an energy gap. If m_v is also broken, then depending on the details of the perturbation the system either becomes a Weyl semimetal or opens an energy gap.

V. MINIMAL MODELS

In the previous section we have shown that TPP configurations demarcate a NL segment that can be characterized by an Euler and 2SW monopole charge (if $\mathcal{PT}$ is present) and by a fractional hinge-charge jump (for all cases). Here we verify these theoretical predictions by analyzing several concrete tight-binding models: First, in Sec. V A we revisit the C_4-symmetric model introduced in Sec. II, and we relate the phenomenology described there to the theoretical results presented in Sec. IV. Subsequently, in Secs. V B and V C we present two C_6-symmetric models, one involving type-A and the other involving type-B TPs, and confirm that the jumps in the 2SW class and in the hinge charge as well as the Euler monopole charge follow the predictions of Table II.

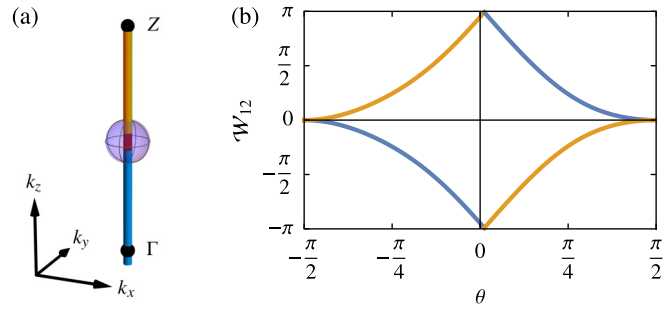

FIG. 12. Verification of the second Stiefel-Whitney monopole charge $w_2 = 1$ carried by the red NL segment in the model defined in Eq. (1). (a) Nodal configuration near the high-symmetry line ΓZ and the ellipsoid (purple) on which the monopole charge is computed. (b) Wilson-loop spectrum $\mathcal{W}_{12}$ of the lower two bands computed on that ellipsoid, parametrized by the latitude $\theta \in [-\pi/2, \pi/2]$. The spectrum shows a single winding (odd parity) and thus implies $|\chi| = 1$ and $w_2 = 1$.

For simplicity, all the discussed models retain both the (spinless) $\mathcal{PT}$ symmetry and the mirror m_v symmetry. It follows from Table I and from the subgroup relations discussed therein that models for all other species of TPPs can in principle be obtained by applying an appropriate perturbation to one of the C_4 or C_6 models discussed in the following subsections. We utilize this feature in Sec. V D, where we break the C_2 symmetry in each of the two C_6-symmetric models. This construction allows us to explicitly show that the 2SW class is not symmetry indicated in C_3-symmetric systems, as previously stated (but not proved) in Sec. IV C.

A. C_4-symmetric model

In Sec. II we introduced a tight-binding model with hinge charges induced by a NL configuration with two pairs of TPs in adjacent band gaps [see Eq. (1) and Figs. 1 and 2]. We observed that the red NL segments divide the BZ into two parts: one with nontrivial 2SW class on 2D cuts through the BZ and hinge charge $\frac{e}{4}$, and another with trivial 2SW class and a vanishing hinge charge. We now recast the phenomenology observed for that model in light of the bulk-hinge correspondence derived in Secs. III and IV and summarized in Table II. In particular, we recognize that the 2SW class and hinge charge are consequences of the nodal configuration of the model with the robust signatures being their jumps as a function of k_z. In addition, we also clarify how the hinge charge $Q_{\llcorner}(k_z)$ plotted in Fig. 2(b) has been extracted.

As we argued in Sec. III A and proved using symmetry indicators in Sec. IV C, each four-band TPP along a C_4-rotation axis (which are automatically type A) demarcates a NL segment in the principal gap [red in Fig. 12(a)] which carries 2SW monopole charge $w_2 = 1$. This can be diagnosed by computing the Wilson-loop spectrum of the lower two bands on an ellipsoid [purple in Fig. 12(a)] containing one such NL segment. Figure 12(b) shows that there is a single winding, confirming that indeed $|\chi| = 1$ and $w_2 = 1$.

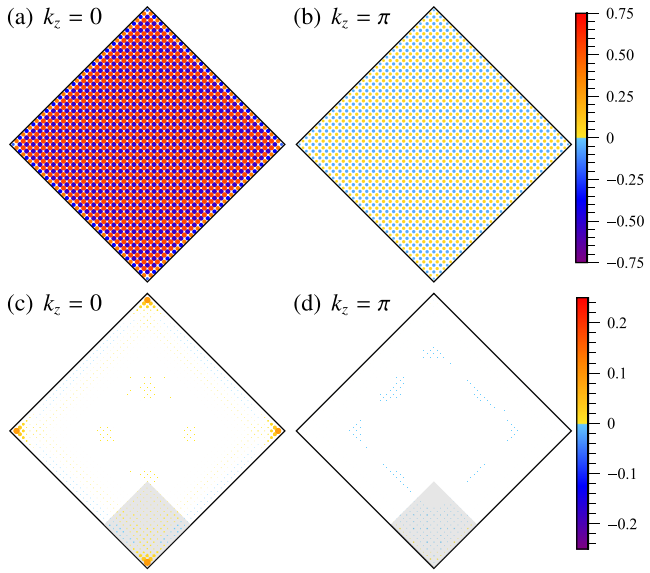

FIG. 13. Charge distribution of the model defined in Eq. (1) and for the geometry illustrated for fewer unit cells in Fig. 2(b). Assuming the compensating ionic charge to be located at Wyckoff position $1a$, we plot the total charge distribution at $k_z = 0$ (a), (c) and at $k_z = \pi$ (b), (d). The total charge at each lattice site is indicated by a disk with its value encoded both in the area of the disk and the color scale (see legend on the right of each row). Note that the disks are scaled separately for each panel: compared to (a) the disks are enlarged by factors of (b) 2, (c) 3, and (d) 6 to increase visibility. To remove sub-unit-cell oscillations of the charge distribution observable in (a) and (b), we perform coarse graining of the data as explained in Appendix D 1 and Fig. 23(b). The results of the coarse graining are shown in (c) and (d), respectively.

Furthermore, according to Table II, the TPP should be accompanied with a fractional hinge-charge jump in a nanowire geometry. To observe the quantized hinge charges and the predicted hinge-charge jump, the termination of the nanowire has to preserve the C_4 symmetry. Here, we opt to study the model in the rotated square geometry shown in Fig. 2. To fully specify the model, we also need to choose where to place the ionic charges. The placement is not fixed by the tight-binding model itself and in a real material would depend on the chemical composition. While the ionic charge distribution affects the value of the hinge charge and can even lead to fractional hinge or corner charges for systems that are electronically completely trivial [88], it does not affect the hinge-charge *jump* because of its independence of k_z. For concreteness, we assume the ionic charge to be concentrated at the center of the 2D projection of the unit cell (Wyckoff position $1a$), as indicated with black circles in Fig. 2(a). However, other distributions of the ionic charge are possible; in particular, moving charge $n|e|$ from $1a$ to $1b$ position changes the corner charge of a 2D system by $-\frac{n|e|}{4}$, as is easily verified from Eqs. (17)–(19) in Ref. [30].

For fixed k_z of the nanowire geometry model, we consider a 2D system with 20.5×20.5 unit cells [compare Fig. 2(a) for 3.5×3.5 unit cells] and compute the charge distribution using exact diagonalization. Results for $k_z = 0$ and π are shown in Figs. 13(a) and 13(b), respectively. On length scales smaller than a unit cell, we observe strong oscillations, which make it impossible to directly integrate the charge on a corner or even detect any possible localization. This is a typical problem for the case of ionic crystals and is usually tackled by coarse graining the charge distribution [29,30,89]. We perform a discrete version of such a coarse graining by following a scheme explained in Appendix D 1. Considering each orbital position (i.e., the two per unit cell) as a separate site of a square lattice, we compute the charge on the *dual square lattice* [cf. Fig. 23(b)] by distributing charge on each site of the original lattice with equal weights to the nearest sites of the dual lattice. Effectively, this coarse grains the charge distribution to the length scale of one unit cell and significantly reduces the oscillations, as shown in Figs. 13(c) and 13(d).

After coarse graining, we can integrate over various regions to find the bulk, edge, and corner charges. First, we observe that the bulk and edge charges vanish for both $k_z = 0, \pi$ as can be seen in Figs. 13(c) and 13(d). Due to the double-band inversion at Γ, the model has vanishing Berry phases along the path $M\Gamma M$ (perpendicular to the edge), which implies [80] that the bulk polarization [81] and therefore the edge charge vanish. On the other hand, the corner charge only vanishes for $k_z = \pi$. The nonvanishing corner charge at $k_z = 0$ is a consequence of the corner-induced filling anomaly [28]. This excess charge is strongly localized near the four corners. Integrating over the gray area indicated in the figure, and taking care that the integration region forms 90° angles with the edges [29], we find $Q_\llcorner = 0.2498e$ for $k_z = 0$ and $Q_\llcorner = 8 \times 10^{-9}e$ for $k_z = \pi$. The deviations from the expected values $\frac{e}{4}$ and 0 are due to finite-size effects, and can be further reduced by increasing the total system size and the coarse-graining scale while keeping the relative size of the integration region fixed.

We numerically compute the 2SW class and the (coarse-grained) corner charge of the C_4-symmetric model defined in Eq. (1) using the described methods for planes at multiple values of fixed k_z. Our results are summarized in Fig. 2(b) in Sec. II. We find that the model exhibits a jump of the 2SW class by $+1$ and of the hinge charge by $+\frac{e}{4}$ as the 2D ICR moves from the occupied to the unoccupied band subspace. This agrees with the prediction of Table II since the ICRs of the bands involved in the two TPs on the HSL ΓZ are $(E; B_1, B_2)$. While far away from the TPs the hinge charge is very close to the quantized value, there are finite-size effects. This is especially observed in the small deviations from the quantized values for k_z near to the closing of the principal gap (i.e., in the vicinity of each TP), where the localization length of the corner charge is expected to grow.

B. C_6-symmetric model with type-A triple points

To realize a type-(A, A) TPP along a C_6 rotational symmetry, we consider the ΓA line of the hexagonal SG $P6/mmm$ (No. 191). More specifically, we consider a model [detailed in Eq. (C3) of Appendix C 2 a] with $(d_{xy}, d_{x^2-y^2})$ orbitals transforming in the 2D ICR E_{2g} and orbitals $f_{x(x^2-3y^2)}$ and $f_{y(3x^2-y^2)}$ transforming in 1D ICRs B_{1u} and B_{2u}, respectively, all placed at the Wyckoff position $1a$ with site-symmetry group D_{6h}. We tune the parameters such that the d orbitals have lower energy than the f orbitals at all HSPs with the

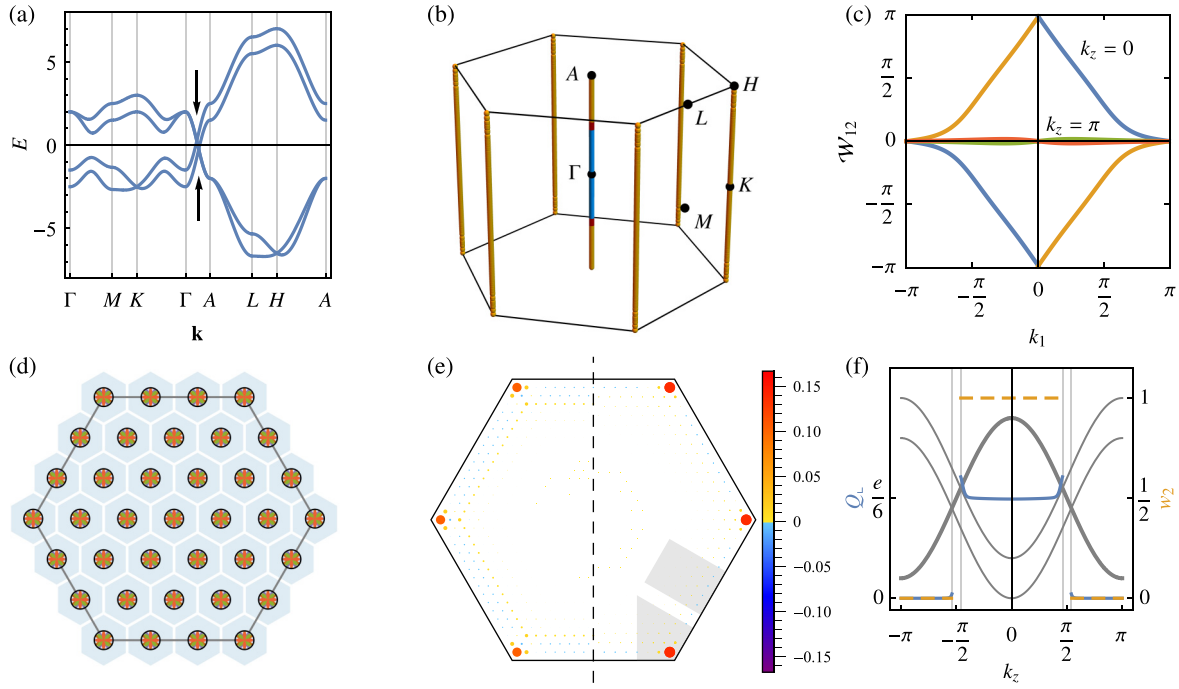

FIG. 14. Results for the C_6-symmetric model with two type-A triple points (TPs) defined in Eq. (C3) and discussed in Sec. V B. (a) Band structure with the two TPs indicated by black arrows. (b) Nodal-line structure in the full Brillouin zone with the high-symmetry points indicated. Nodal lines in the first, second, and third band gaps of the four-band model are shown in orange, red, and blue, respectively. (c) The second Stiefel-Whitney class can be determined from the Wilson-loop spectrum $\mathcal{W}_{12}$ of the lower two bands on horizontal cuts through the Brillouin zone (parametrized by the projection k_1 of the momentum onto the first reciprocal lattice vector). Blue/orange lines show the spectrum for $k_z = 0$ (single winding) and green/red lines for $k_z = \pi$ (no winding). (d) Cross section through a hexagonal nanowire three shells wide; light blue hexagons indicate the model's unit cells. The orbitals are represented in color and all placed on top of each other in the center of the unit cell. The ionic charge is concentrated at the same position, indicated by the black circles. (e) Charge distribution for a cut through a 16-shell-wide nanowire at $k_z = 0$. The charge at each site is indicated by a disk with its value encoded both in the area of the disk and the color scale (see legend on the right). The left half shows the charge distribution on the original lattice, and the right half shows the charge after two iterations of coarse graining [cf. Appendix D 1 and Fig. 23(c)]. A hinge charge of $Q_\llcorner = \frac{e}{6}$ with a strong localization is observed. (f) Hinge Brillouin zone with hinge charge $Q_\llcorner$ (blue solid line, left axis), second Stiefel-Whitney class w_2 (orange dashed line, right axis), and the projection of the bulk dispersion along $k_x = k_y = 0$ (gray). The doubly degenerate band is displayed with a thicker line.

exception of a double-band inversion at Γ. Consequently, on ΓA two 1D ICRs (B_1, B_2) consecutively cross the 2D ICR (E_2) resulting [60] in two type-A TPs. The band structure and the NL configuration of the model are displayed in Figs. 14(a) and 14(b), respectively. We remark that apart from the twofold degeneracy along the ΓA line, the model also exhibits twofold degeneracies along the KH lines; however, these lie within the occupied band subspace and therefore have no effect on the discussed topological features. The model exhibits no additional NLs beyond these degeneracies along the HSLs. We remark that for the computation of the hinge charges we set the compensating ionic charge to also reside at site 1a.

According to Table II, we expect a jump of $+\frac{e}{6}$ in the hinge charge and $+1$ in both the Euler and 2SW class when going from the orange k_z range to the blue k_z range. More precisely, based on a symmetry eigenvalue analysis and Eqs. (4) and (5), we expect that the 2SW class is 1 in the blue k_z range and 0 in the orange k_z range, while the hinge charge should be $\frac{e}{6}$ and 0, respectively. The results for the 2SW class are verified by computing the Wilson-loop spectra of the lower two bands on horizontal cuts through the BZ as a function of k_z. The 2SW class is then given by the parity of the winding of the spectrum. Two examples, for $k_z = 0$ and π, are shown in Fig. 14(c), and demonstrate that indeed $|\chi| = 1$ and $w_2 = 1$ for $k_z = 0$. Figure 14(f) shows w_2 as a function of k_z with the visible jumps at the position of the two TPs along the ΓA line.

To verify the results for the hinge charge, we construct a system finite in x and y directions with 16 hexagonal shells in the cross section [the cross section illustrated in Fig. 14(d) has three shells]. Using exact diagonalization we find the charge distribution at half-filling for 2D cuts of the BZ that lie outside of the red k_z range. Figure 14(e) shows the results of such analysis for $k_z = 0$. The charge is strongly localized at the corners of the 2D cross section while it vanishes both in the bulk as well as along the edges. Note that while the charge vanishes on the edges [integrating over the gray edge area in Fig. 14(e) we obtain $8 \times 10^{-4}|e|$], we also observe small oscillations of the charge in the direction perpendicular to the edges which visually obscure the localization of the corner charge. To reduce these oscillations, we perform coarse graining similar to the one described in the previous subsection. The major technical difference is that here we coarse grain over a hexagonal supercell with two shells, i.e., seven unit cells, in one iteration (cf. Fig. 23). After two iterations we end

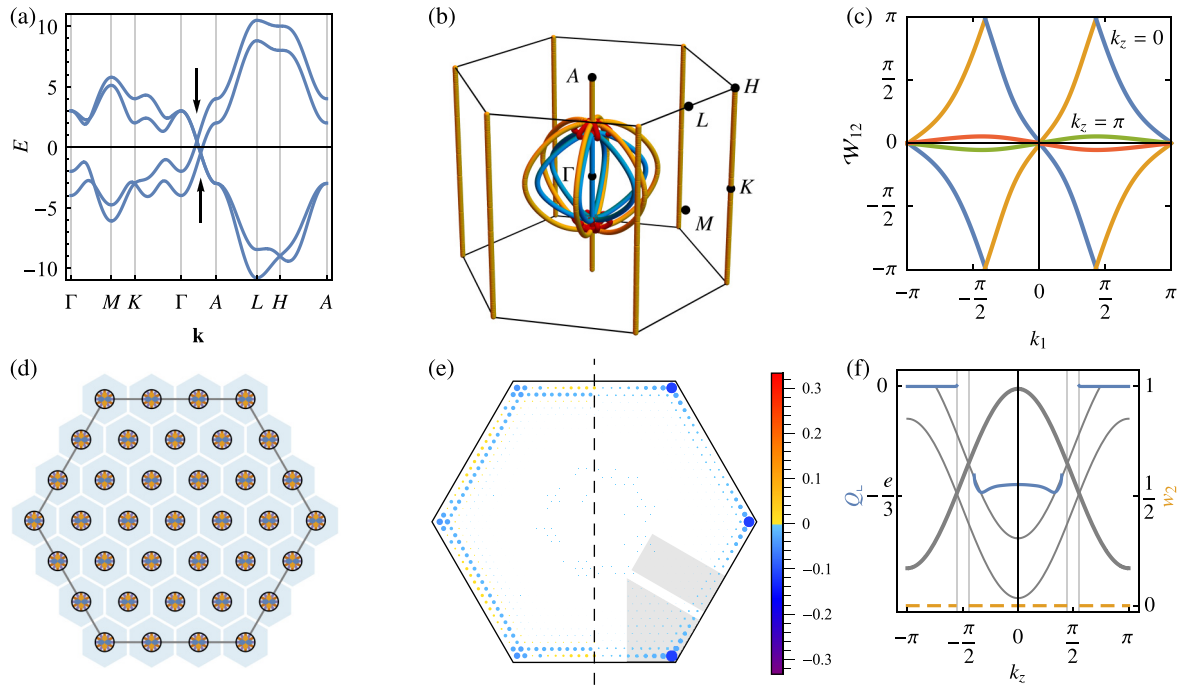

FIG. 15. Results for the C_6-symmetric model with two type-B triple points (TPs) defined in Eq. (C5) and discussed in Sec. V C. The organization of the panels is in one-to-one correspondence with Fig. 14. The key differences to observe are as follows: (b) Due to the TPs being type B, there are nodal-line arcs attached to them, visible in the nodal-line structure. (c) The Wilson-loop spectra for both $k_z = 0$ and π show double and zero winding, respectively, implying $|\chi| = 2$ and $w_2 = 0$. (e), (f) The hinge charge in the region around $k_z = 0$ is $Q_\llcorner = -\frac{e}{3}$; the localization length is larger than for the model shown in Fig. 14, such that finite-size effects produce a visible deviation from the ideal quantized value of the corner charge in (f).

up with a coarse-grained lattice that is smaller by two shells. Integrating over the gray corner area in Fig. 14(e) we obtain $0.1652e$, where the deviation from $\frac{e}{6}$ can be traced back to finite-size effects. As can be seen in Fig. 14(f) those finite-size effects grow stronger with decreasing the central energy gap, i.e., close to the two TPs.

C. C_6-symmetric model with type-B triple points

We next consider a C_6-symmetric model with type-(B, B) TPP realized in the same SG ($P6/mmm$, No. 191) and on the same hexagonal lattice. The following four orbitals are placed at Wyckoff position $1a$: $f_{x(x^2-3y^2)}$ and $f_{y(3x^2-y^2)}$ transforming, respectively, in 1D ICRs B_{1u} and B_{2u}, together with (p_x, p_y) transforming in the ICR E_{1u}. The model's Bloch Hamiltonian is given in Eq. (C5) in Appendix C 2 b. As in the previously discussed tight-binding models, we set the parameters to produce a double-band inversion at Γ. As a consequence, the p orbitals have lower energy than the f orbitals at all HSPs except Γ. Then, two 1D ICRs (B_1, B_2) consecutively cross the 2D ICR (E_2) resulting [60] in two type-B TPs. The band structure and the NL configuration are shown in Figs. 15(a) and 15(b), respectively. We observe the NL arcs attached to the type-B TPs; as desired, the NL arcs in the principal gap (shown in red) are tied together in the red k_z range [cf. Fig. 10(b)]. There are no further degeneracies in the principal band gap of the model. According to Table II, we expect a jump of $-\frac{e}{3}$ in the hinge charge and no jump of the 2SW class when the 2D ICR along ΓA moves from the occupied to the unoccupied band subspace, but an Euler monopole charge $|\chi| = 2$. More precisely, based on a symmetry eigenvalue analysis and Eqs. (4) and (5), we anticipate that the 2SW class vanishes in *both* regions, while the hinge charge is expected to be 0 and $-\frac{e}{3}$ in the orange and blue k_z range, respectively, assuming that the compensating ionic charge is placed at position $1a$.

We verify these predictions numerically. First, in Fig. 15(c) we plot the Wilson-loop spectra of the lower two bands on horizontal cuts at both $k_z = 0$ and π. Since they both exhibit even winding number, we confirm that $w_2 = 0$ on both sides of the TPPs. We observe that the Wilson-loop spectrum for the 2D cut at $k_z = 0$ has winding number ± 2, meaning that the corresponding 2D model is an Euler insulator [74]. The double winding also implies that each TPP with its attached (red) NL arcs (the *nodal-line nexus*) carries a Euler class $|\chi| = 2$ on both the occupied and the unoccupied band subspaces, as predicted. Therefore, as long as $\mathcal{PT}$ symmetry is present, the only way to gap out the red NL nexus is to annihilate it with the other NL nexus [68]. We remark that this topological obstruction is trivialized in the presence of additional occupied and unoccupied bands [71].

To calculate the hinge charge, we construct a system finite in x and y directions with 20 hexagonal shells in the cross section [in Fig. 15(d) we illustrate a system with three hexagonal shells]. By exact diagonalization we find the charge distribution at half-filling for values of k_z where the spectrum is gapped. In Fig. 15(e) the charge distribution for $k_z = 0$ is shown. The charge is still localized at the corners of the 2D cross section and vanishes both in the bulk as well as along the edges. However, due to trivial in-gap states and therefore a reduced energy gap, we observe an oscillation of

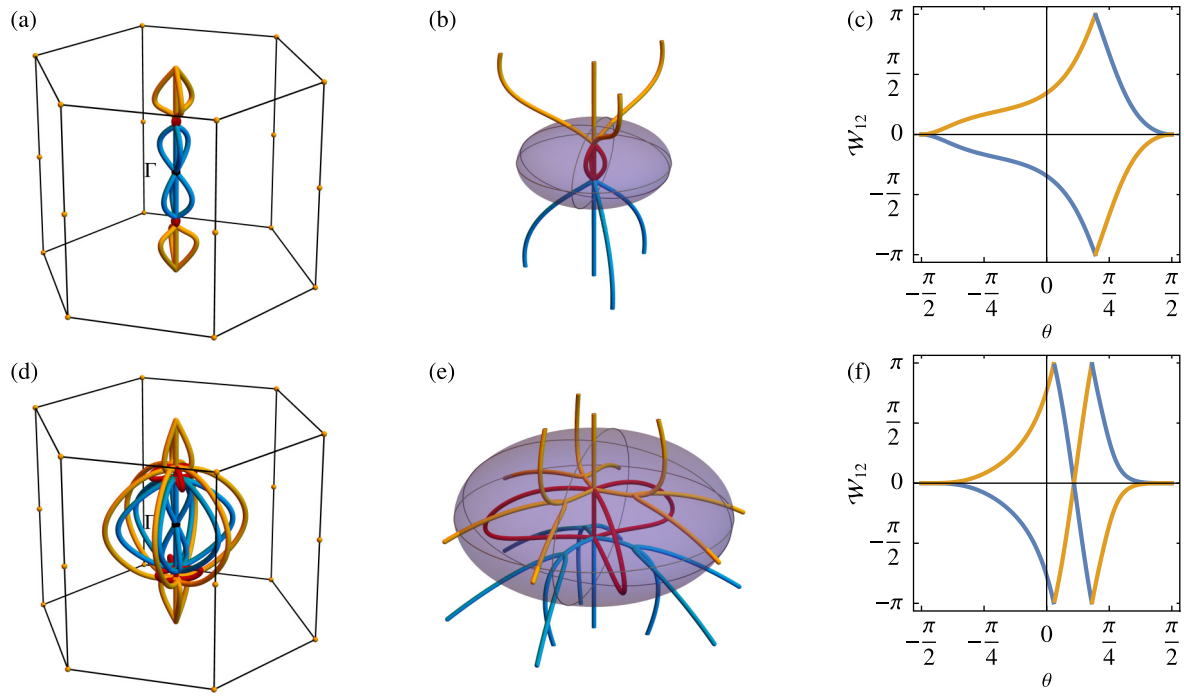

FIG. 16. Nodal lines and Wilson-loop spectra for the C_3-symmetric models obtained by breaking the C_6 symmetry in the models discussed in Secs. V B and V C using the trigonal perturbation given in Eq. (C6) with $\delta_{C_3} = 8 \times 10^{-4}$. (a), (d) Nodal lines in the full Brillouin zone (black frame). Nodal lines in the first, second, and third band gaps are shown in orange, blue, and red, respectively. (b), (e) Closeups of the red nodal-line segment. In both cases the triple points are clearly type B with three attached nodal-line arcs per energy gap. (c), (f) Wilson-loop spectra on the purple ellipsoids shown in (b) and (e), respectively. The single winding in (c) implies $|\chi| = 1$ and $w_2 = 1$ and the double winding in (f) implies $|\chi| = 2$ and $w_2 = 0$.

the charge distribution in the direction perpendicular to the edge, as well as a significantly larger localization length for the corner charge than found in the previous hexagonal model. In fact, the chosen system is too small to achieve convergence, but it is sufficient to support the theoretical predictions in Table II. Integrating the coarse-grained charge distribution over the gray edge area in Fig. 15(e) we obtain $4 \times 10^{-2}|e|$; while over the gray corner area we find $-0.2983e$, which is close to the ideal result $-\frac{e}{3}$ in the absence of finite-size effects. We repeat the same analysis for 2D cuts for multiple values of k_z, and plot the dependence of the 2SW class and of the hinge charge as a function k_z (where the gap is open) in Fig. 14(f).

D. C_3-symmetric models

In this section, we explicitly show that in the presence of $\mathcal{PT}$ symmetry there exist C_3-symmetric models where the TPPs carry either $w_2 = 0$ or 1. We therefore confirm that the 2SW monopole charge in C_3-symmetric SGs is not symmetry indicated, thus justifying the ambiguous entry in Table II. This freedom is present despite the fact that (cf. Table I), C_3-symmetric HSLs only support a single species of TPs, namely, type B with three attached NLs arcs and with the central NL carrying Berry phase π.

We can obtain such C_3-symmetric models by reducing the C_6 symmetry of the models discussed in Secs. V B and V C down to C_3 (while keeping $\mathcal{PT}$). A possible perturbation that achieves that is given by Eq. (C6) in Appendix C 2 c. The resulting NL structure for each parent model is shown in Figs. 16(a) and 16(b) and 16(d) and 16(e), respectively. Note that the 2SW monopole charges of the TPPs in the parent hexagonal models are not changed by the trigonal perturbation: as long as the enclosing ellipsoid [purple in Figs. 16(b) and 16(e)] is chosen to be sufficiently large to contain the lobes of red NLs, the principal gap does not close on that ellipsoid, keeping the Wilson-loop winding invariant. We confirm this by explicitly computing the Wilson-loop spectra on the enclosing ellipsoids of the perturbed models, plotted in Figs. 16(c) and 16(f).

We briefly comment on the change of the NL configurations from Figs. 14(b) and 15(b) to Figs. 16(b) and 16(e), respectively. In both cases, the central NL stretched along ΓA initially carries quaternion charge -1 (corresponding to Berry phase 2π [66], i.e., it is a quadratic NL) before switching on the trigonal perturbation. Let us first consider the case of type-A TPs [$w_2 = 1$, Figs. 16(a)–16(c)]. Here, as soon as the perturbation is switched on, all three segments of the central NL, i.e., in the orange, red, as well as blue k_z ranges, split into four NLs with Berry phase π each. One NL of the quadruplet is still pinned to the ΓA line, while the other three NLs are related by the C_3 symmetry and remain attached to the TPs. As a result, the hegaonal type-A TPs with no attached NL arcs have transformed into trigonal type-B TPs with three attached NL arcs in each gap, as detailed in Fig. 16(b).

For the hexagonal model with type-B TPs [$w_2 = 0$, Figs. 16(d)–16(f)], the process is similar; in particular, one observes the same splitting of the central quadratic NL into four linear NLs around the HSL. However, in this case the

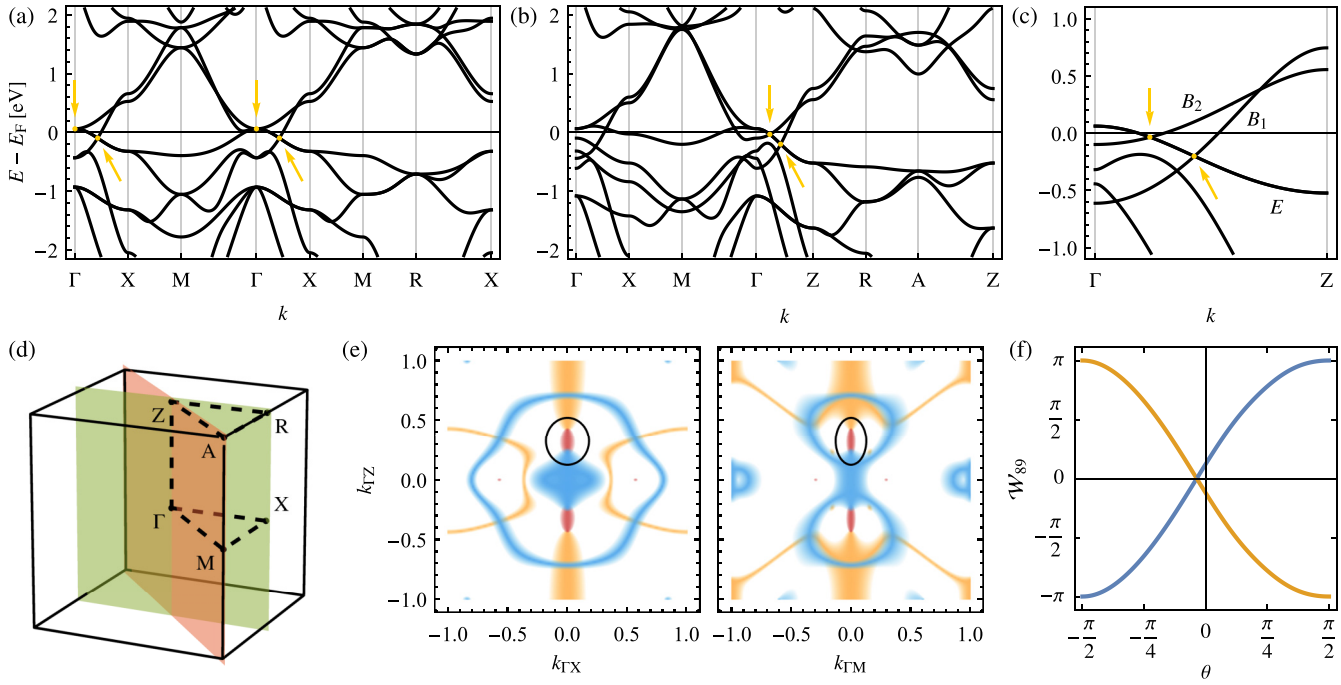

FIG. 17. Bulk properties of the compound Sc_3AlC. The band structure (a) without any strain and (b) with 6.6% uniaxial compressive strain in z direction, which generates a triple-point pair on the ΓZ line. Triple points are indicated by yellow arrows. (c) Closeup of the band structure near the triple-point pair with the relevant bands labeled by their irreducible corepresentations. (d) The Brillouin zone of the tetragonal lattice of strained Sc_3AlC. The high-symmetry points and mirror planes are indicated. (e) Nodal lines in the relevant three gaps (orange, blue, red according to increasing energy) determined from the Wannier tight-binding model for the mirror planes shown in (d). The triple point is clearly type A. The cross sections of the ellipsoid on which we compute the second Stiefel-Whitney monopole charge with the mirror planes are indicated by black ellipses. (f) Wilson-loop spectrum of the relevant bands computed on the ellipsoid indicated in (e); the single winding implies $w_2 = 1$.

hexagonal NL configuration starts out with six attached NLs per gap because the hexagonal TPs have been type B. Here the three new NL arcs either annihilate with three of the original NL arcs (in the principal gap, red) or combine with the original NL arcs to form intersecting nodal chains (other two gaps, orange and blue) [90]. As a result, we find that the hexagonal type-B TPs have been transformed into trigonal type-B TPs with three attached NLs per gap, as predicted in Ref. [60]. The intersection of the orange and of the blue NLs visible in Fig. 16(e) is stablized by the non-Abelian band topology in the presence of m_v and $\mathcal{PT}$ symmetries, as discussed in Ref. [66].

VI. MATERIAL EXAMPLES

In this section we discuss two concrete material examples that illustrate the introduced phenomenology. While these examples demonstrate that the higher-order topology of TPs can arise in crystalline solids, the large values of strain required to realize the presented band structures imply that our particular materials predictions are not amenable to experimental studies, and that further research is needed to find realistic material candidates. Note that in Sec. VIII we briefly discuss the higher-order bulk-boundary correspondence for TPPs in *spinful systems*.

Our discussion is structured as follows. In Sec. VI A we show that the compound Sc_3AlC subjected to large uniaxial strain exhibits a TPP with type-A TPs on the $Z\Gamma Z$ line and no interfering NLs. Based on first-principles calculations and an *ab initio* tight-binding model, we compute the 2SW monopole charge and the hinge-charge jump. We find that the 2SW monopole charge takes value $w_2 = 1$ and that a fractional hinge-charge jump $\Delta Q_\llcorner = \frac{e}{4}$ is present, in agreement with the values predicted by Table II. This demonstrates the higher-order bulk-boundary correspondence introduced in Sec. IV.

In Sec. VI B we study a material example with a NL segment carrying nontrivial Euler monopole charge. The TP material Li_2NaN [60,91] has a single pair of inversion-related type-A TPs along the $A\Gamma A$ line. Based on an *effective* tight-binding model [60], we show that one of the NL segments carries Euler monopole charge $|\chi| = 2$. Furthermore, we demonstrate that this leads to a topological obstruction preventing the removal of that NL segment when colliding the two TPs at the A point, instead leading to a conversion into a nodal ring.

A. Nontrivial Stiefel-Whitney class in strained Sc_3AlC

We first consider Sc_3AlC [92], which, on the level of a Wannier tight-binding model, manifests the bulk-hinge correspondence for TPPs derived in Sec. IV C. The compound has a cubic crystal structure with SG $Pm\bar{3}m$ (No. 221) and exhibits a threefold-degenerate touching point at Γ and TPs on the ΓX, ΓY, and ΓZ lines (which are all equivalent) [see Fig. 17(a)]. Furthermore, the spin-orbit coupling is expected to be small due to the elements involved being light, therefore, we can neglect it and treat the electrons as spinless. Then, the system

possesses $\mathcal{PT}$ symmetry squaring to $+\mathbb{1}$. Applying uniaxial compressive strain along one of the equivalent crystal axes (which we choose to be the z direction) removes the TPs on the ΓX and ΓY lines leaving only those on the ΓZ line, and splits the touching point at Γ into two additional TPs on the ΓZ line [cf. Fig. 17(b) for approximately 6.6% strain]. The result is a configuration of two inversion-symmetry-related TPPs on the ΓZ line with one TPP shown in Fig. 17(c). The strained material has a simple tetragonal crystal structure with SG $P4/mmm$ (No. 123).

We study the material by first obtaining the band structure and wave functions from density functional theory (DFT) calculations with the projected augmented wave (PAW) method implemented in the Vienna *ab initio* simulation package (VASP) [93,94] with generalized gradient approximation (GGA) and Perdew-Burke-Ernzerhof (PBE) approximation [95]. We use a Γ-centered $8 \times 8 \times 8$ k mesh. Uniaxial compressive strain in z direction is modeled by reducing the lattice constant in that direction by the appropriate amount. The lattice structure of Sc_3AlC is obtained from the Materials Project database [96] (material identifier mp-4079 [92]) with lattice vectors $a = 4.512$ Å ($a = 4.512$ Å and $c = 4.212$ Å after strain). We construct Wannier functions using WANNIER90 [97] resulting in a Wannier tight-binding model with s, p, d orbitals of Sc and s, p orbitals of Al and C. We process disentanglement with a frozen window from -20 to 4 eV relative to E_F but do not perform maximum localization [98]. The hoppings of the Wannier model are symmetrized [99] in real space.

To check for conflicting NLs in the BZ, we perform additional DFT calculations on the two inequivalent mirror planes $X\Gamma Z$ and $M\Gamma Z$. The results are shown in Fig. 17(e) and we observe that the only NLs in the principal gap are the two NL segments (red) spanning between the TPs of each TPP. In particular, there are no additional NLs attached to the TPs off the HSL, confirming that the TPs are type A, in agreement with Table I. This allows us to define an ellipsoid [whose intersections with the two mirror planes are indicated by the black ellipses in Fig. 17(e)] enclosing the TPP on which the relevant 2SW monopole charge is defined. Using the Wannier tight-binding model and the Python package Z2PACK [100,101] we compute the Wilson-loop spectrum on the ellipsoid [cf. Fig. 17(f)], and find that it winds once, therefore indicating $w_2 = 1$.

We further proceed to study the hinge-charge jump in strained Sc_3AlC. First, we calculate the traces of matrix representations obtained from VASP to get the ICRs of the energy bands at HSPs in the first BZ with the help of IRVSP [102]. The corepresentations at HSLs are then inferred using compatibility relations obtained from the Bilbao crystallographic server (BCS) [103–106]. The ICRs of the bands forming the TPP are found to be $(E; B_1, B_2)$ [cf. Fig. 17(c)]. Based on Table II, the knowledge of the rotational symmetry C_4, the HSL ΓZ, and the ICRs of the little cogroup of that line allows us to predict the fractional part of the hinge-charge jump $\Delta Q_\llcorner$ to be $+\frac{e}{4}$.

To compute the hinge-charge jump explicitly and to verify the above prediction, we use the Python package PYTHTB to construct a nanowire with a C_4-symmetric cross section of 9.5×9.5 unit cells from the bulk Wannier tight-binding model [see Fig. 18(a)]. Recall that the placement of the ionic charge in the unit cell does not influence the hinge-charge *jump*. Therefore, we choose it such that it simplifies our calculations: we assume all ionic charge of a unit cell to be concentrated at WP $1b$ (at the corner of the 2D projection of the unit cell), which is also the location of the center of the cross section [cf. Fig. 18(a)]. The band structure of the nanowire is shown in Fig. 18(b) as a function of the remaining momentum k_z. Each state ψ is colored according to the inverse participation ratio $\sum_i p_i(\psi)^2$ where $p_i(\psi)$ is the probability of finding an electron in state ψ at site i in the 2D cross section. Together with the gray overlay of the bulk states, we can easily identify the in-gap surface (green) and hinge (red) states.

We now select two k_z values at which the principal gap is open in the spectrum of the nanowire [yellow diamond and purple triangle in Fig. 18(b)]. Assuming that all states below the indicated gap are occupied, we compute the total charge distribution in the nanowire. The results for $k_z = 0.08$ and 0.34, after coarse graining over a unit cell (see Appendix D 1), are shown in Figs. 18(d) and 18(e), respectively. Integrating over successively larger square regions at one of the corners [cf. gray squares in Figs. 18(d) and 18(e)], we observe that the corner charge (corresponding to the hinge charge of the 3D model at the selected value of k_z) converges to $\frac{e}{4}$ and 0 for $k_z = 0.08$ and 0.34, respectively. This verifies that the jump is $\Delta Q_\llcorner = \frac{e}{4}$, as predicted.

The localization of the charge at the corners is already visible in Figs. 18(d) and 18(e) and the edge charge (corresponding to the surface charge of the 3D model) is clearly vanishing; however, there are strong oscillations of the charge on the edges. These oscillations are due to trivial surface states, as is revealed by computing the charge distribution on a slab (data not shown). Using the information about the charge distribution on the slab, we remove (see Appendix D 2) this edge signal and reveal the strong localization of the net charge on the corners [cf. Figs. 18(f) and 18(g). Note that this *removal* of the charge oscillations is performed in a charge-neutral way, i.e., by changing neither the corner nor the edge charge.

B. Nontrivial Euler monopole charge in Li_2NaN

We now turn our attention to Li_2NaN. Reference [60] identified the compound Li_2NaN as an ideal candidate to observe the conversion of TPs to multiband nodal links, and developed its description using an effective four-band model which we assume in the following discussion. The compound exhibits a single pair of inversion-related TPs and no additional NLs close to the central NL (along the reciprocal lattice vector $\mathbf{G_3} \parallel k_z$) and TPs, as shown in Fig. 19(a). Therefore, this is also an ideal candidate for a TP-induced Euler monopole charge. The Berry phases of each band of the tight-binding model in k_z direction can be easily computed using the Wilson-loop method, and we obtain $(0, 0, 0, \pi)$, with the nontrivial value carried only by the highest-energy band. Based on the arguments presented in Sec. III B, we therefore predict the red NL segment (connecting TPs in two adjacent BZs) to carry Euler monopole charge $|\chi| = 2$ and the blue one $\chi = 0$. We verify these predictions in the effective four-band tight-binding model by computing the Euler class on ellipsoids enclosing the corresponding NL segment, such

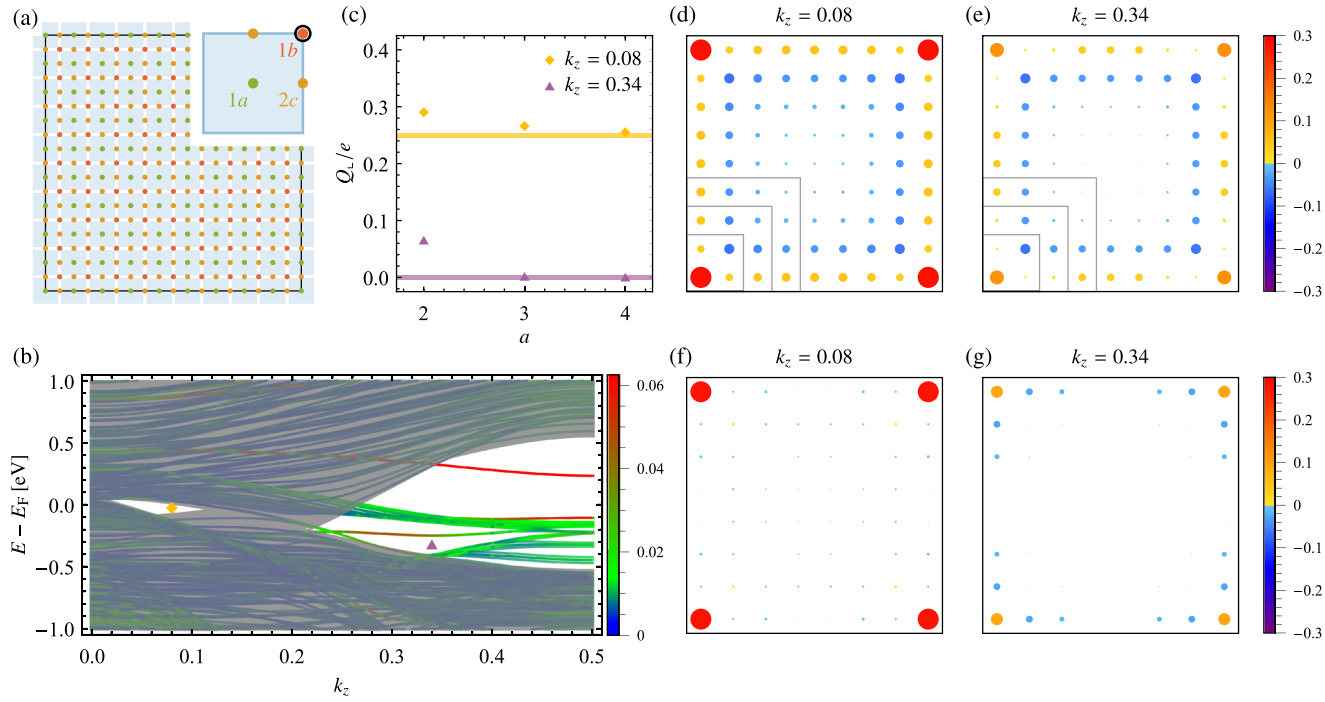

FIG. 18. Hinge-charge jump observed in the nanowire geometry of Sc_3AlC. (a) Cross section of the nanowire geometry (extended along the z direction) with 9.5×9.5 unit cells. The unit cells are shown as blue shaded squares, and the boundary of the nanowire indicated with a black frame. Two-dimensional Wyckoff positions (WPs) are shown as green, red, and orange points with their labels in the inset that shows an enlarged single unit cell. The scandium atoms project onto WPs $1b$ and $2c$, the aluminum atoms onto $1a$, and the carbon atoms onto $1b$. Note the C_4 symmetry of the cross section with the center at WP $1b$. The black circle in the enlarged unit cell denotes the location of the ionic charge of $8|e|$ per unit cell. (b) Band structure of the nanowire (colored lines) with cross section shown in (a) as a function of momentum (k_z) in the hinge Brillouin zone. The projected bulk bands (transparent gray) are overlayed on the nanowire spectrum. The coloring of the bands (see legend) encodes the inverse participation ratio, with a larger value indicating localization on fewer sites. Consequently, hinge-localized states are colored red, surface-localized states green, and bulk states blue. The two energy gaps to the left and to the right of the studied triple-point pair are marked by a yellow square ($k_z = 0.08$) and by a purple triangle ($k_z = 0.34$), respectively. (c) Integrated corner charge (corresponding to the hinge at the selected values of k_z) for the two k_z cuts with filling as indicated in (b) as a function of the side length a of the square integration region [cf. gray squares in (d) and (e)]. The corner charge for $k_z = 0.08$ converges to $\frac{e}{4}$ and for $k_z = 0.34$ to 0 (yellow vs purple solid lines). (d), (e) Charge distribution coarse grained over one unit cell for $k_z = 0.08$ and 0.34, respectively. The magnitude of the charge (in units of e) is shown by both the area of the circles as well as the color (see legend on the right). (f), (g) Charge distribution for the same values of k_z after removing the contributions from the edge based on slab calculations (cf. Appendix D 2). In (f) the localization of a nonzero charge on the corners is clearly visible.

as shown in Fig. 19(a), using three independent methods: (i) via the linking numbers obtained when applying strain to get proper linked nodal rings, (ii) via Wilson-loop spectra, and (iii) directly via the Euler curvature [73].

We first discuss the red NL segment. Following the argument of Sec. III, we reduce the C_6 rotational symmetry of Li_2NaN down to C_2 by applying tensile strain of approximately 5% in y direction. This turns the NL segment into linked red and blue NL rings [cf. Fig. 19(b)]. The Berry phases $\phi_{3,4}$ of the bands forming the blue NL (i.e., bands 3 and 4) on the green contour satisfy $\phi_3 + \phi_4 = \pi \mod 2\pi$. Thus, according to Sec. III B, the red nodal ring and consequently also the red NL segment in Fig. 19(a) carry Euler monopole charge $|\chi| = 2$. We arrive at the same conclusion based on the Wilson-loop spectrum computed on the purple ellipsoid shown in Fig. 19(a). The double winding implies [68] $|\chi| = 2$.

To verify this prediction independently, recall that the Euler class can be brought [69,107] to a form analogous to the Chern number, i.e., an integral of a curvature over the base manifold. By adopting a Hilbert-space basis for which $\mathcal{PT}$ is represented by complex conjugation [73], the eigenstates can be gauged to be purely real. For two real Bloch bands $|u_1(\mathbf{k})\rangle$ and $|u_2(\mathbf{k})\rangle$ (which could possibly be degenerate with each other, but which must be separated by energy gaps from all other bands) one then defines the *Euler curvature*

$$\mathbf{F}(\mathbf{k}) = \langle \nabla_{\mathbf{k}} u_1(\mathbf{k})| \times |\nabla_{\mathbf{k}} u_2(\mathbf{k})\rangle, \tag{15}$$

i.e., as the off-diagonal component of the two-band non-Abelian Berry-Wilczek-Zee connection [69,73]. Integrating the curvature over a closed surface S^2 gives the Euler class

$$\chi = \frac{1}{2\pi} \int_{S^2} d\mathbf{S} \cdot \mathbf{F}(\mathbf{k}) \in \mathbb{Z}. \tag{16}$$

Note that the Euler class is independent of the parametrization of S^2, such that we can parametrize the relevant ellipsoid by

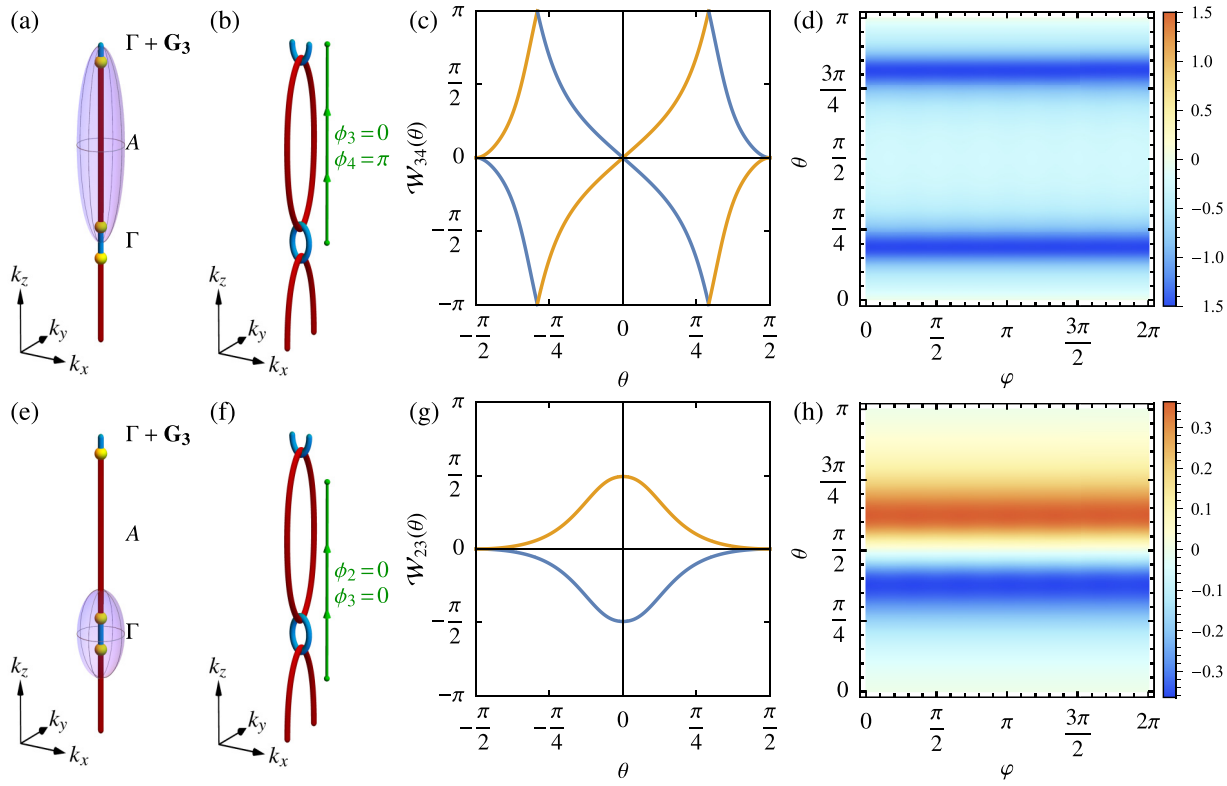

FIG. 19. Verification of the Euler monopole charge $|\chi| = 2$ ($\chi = 0$) on the red (blue) nodal-line segment in Li_2NaN, based on the four-band tight-binding model of Ref. [60]. (a)–(d) Show illustrations and data for the red nodal-line segment (centered at A) and (e)–(h) for the blue segment (centered at Γ). (a), (e) Nodal line and triple-point configuration in the first one-and-a-half Brillouin zones $A\Gamma A\Gamma$. Nodal lines in the second and third band gaps are shown in red and blue, respectively; triple points are shown in yellow. The purple ellipsoid defines the surface on which we compute the Euler class. (b), (f) Linking structure of the corresponding nodal chain configuration after applying approximately 5% tensile strain in y direction. The green line shows the closed contour on which the Berry phases are computed. (c), (g) Spectrum of the Wilson-loop operators $\mathcal{W}_{ij}(\theta)$ of bands i and j as indicated in the axis labels of constant latitude contours on the purple ellipsoid in (a) and (e), respectively, parametrized by the latitude angle θ. (d), (h) Euler curvature $F(\theta, \varphi)$ on the purple ellipsoid in (a) and (e), respectively, calculated using the algorithm from Ref. [73]. The curvature integrates to $|\chi| = 2$ in (d) and to $\chi = 0$ in (h).

the spherical coordinates $(\theta, \varphi) \in [0, \pi] \times [0, 2\pi)$ and define

$$F(\theta, \varphi) = \langle \nabla_{(\theta,\varphi)} u_1(\theta, \varphi)| \times |\nabla_{(\theta,\varphi)} u_2(\theta, \varphi)\rangle. \quad (17)$$

We utilize the algorithm of Ref. [73] implemented in *Mathematica* to compute the Euler curvature on the ellipsoid shown in Fig. 19(a). The resulting $F(\theta, \varphi)$ is plotted in Fig. 19(d). Integration over the full ellipsoid confirms that $|\chi| = 2$.

The nontrivial value of χ implies a topological obstruction as discussed in Sec. III B: the red NL segment cannot be removed completely as long as $\mathcal{PT}$ symmetry is preserved. We verify this explicitly in the context of the tight-binding model of Ref. [60]. The 1D ICR involved in the TP has most of its weight on the nitrogen p_z orbital, such that we can move the TPs towards the A point by reducing the onsite energy of that orbital. We denote the change in energy by $\Delta\varepsilon_{N p_z} = -\delta$ eV < 0. As shown in Fig. 20, increasing δ shrinks the red NL segment until the two TPs collide at A. At that stage, the band degeneracy in the red energy gap has reduced to a single touching point at A. However, the Euler monopole charge prevents opening of the energy gap; indeed, increasing δ even further results in a conversion of the red TP segment into a nodal ring in the horizontal $k_z = \pi$ plane. Crucially, the Euler monopole charge persists in $\mathcal{PT}$-symmetric systems even if the horizontal m_z symmetry was removed from the model.

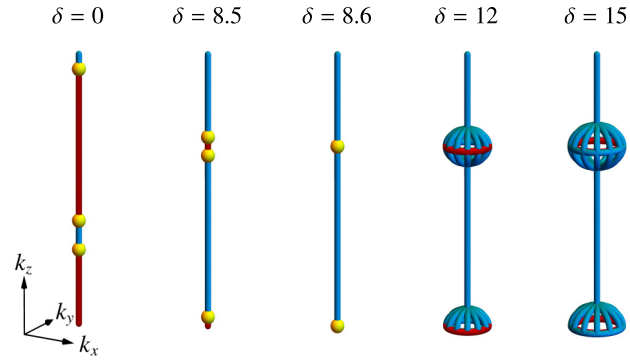

FIG. 20. Demonstration of the topological obstruction of the red nodal-line segment in Li_2NaN due to the nontrivial Euler monopole charge. The nodal lines (obtained from the tight-binding model in Ref. [60]) near the rotation axis $A\Gamma A\Gamma$ spanning over one-and-a-half Brillouin zones are shown, with nodes in the second and third band gaps shown in red and blue, respectively. The two triple points (yellow) can be forced to collide as described in the text by tuning a parameter δ of the tight-binding model. The triple points collide at $\delta = -8.6$, at which point the red NL segment has been reduced to only a single touching point at A. Increasing δ even further, a horizontal red nodal ring forms in the ALH plane.

We remark that the critical three-band touching obtained by colliding the two TPs at the A point shares certain similarities with the very recently discussed Euler topology of topological acoustic triple points by Ref. [108]. The notable difference is that in our case the Euler-point degeneracy requires fine tuning of the model parameters, whereas Ref. [108] finds this to be a *generic* feature of the acoustic phonon branches.

Finally, we also comment on the blue NL segment. We can use the same three arguments to show that $\chi = 0$ in this case. For the argument via the linking, the relevant change is that now we need to consider bands 2 and 3, whose Berry phases along the green contour [cf. Fig. 19(f)] are both vanishing. Therefore, $\chi = 0$ despite the linking of the rings (see Sec. III B and Appendix E). We arrive at the same conclusion by observing that the Wilson-loop spectrum in Fig. 19(g) does not wind. Finally, in Fig. 19(h), we present the Euler curvature for the purple ellipsoid shown in Fig. 19(e). The Euler curvature turns out to be antisymmetric with respect to reflection at $\theta = \pi/2$, such that integrating over the whole ellipsoid results again in $\chi = 0$.

VII. EXTENSION TO NONSYMMORPHIC SPACE GROUPS

Up to now, we have simplified the presented analysis by excluding nonsymmorphic SGs, i.e., SGs containing symmetries like screw rotations and glide planes. In this section we discuss these excluded cases, arguing that the inclusion of nonsymmorphic elements in the space group does not change the bulk-hinge correspondence. In particular, we reveal that Table II applies to triple-point pairs in nonsymmorphic SGs as well, with the only differences being that (i) the first row of the table "C_n" should be interpreted as only the point-group part of the possibly present nonsymmorphic screw symmetry (i.e., without the translation), and (ii) the mapping of ICRs of the little group to the ICRs of the little *cogroup* should be performed as described in Ref. [59].

To motivate the advertised result, note that our parallel work [59] shows that nonsymmorphic symmetries do not alter the classification of TPs. More precisely, as long as the HSL supports TPs (i.e., both 1D and 2D ICRs of the little group exist; due to nonsymmorphicity this property may be lost for certain HSLs on the BZ boundary), the symmetry constraints on the Bloch Hamiltonian $\mathcal{H}(\mathbf{k})$ due to some corepresentation of the little group $\mathcal{G}^{\mathbf{k}}$ of the HSL supporting TPs, are *equivalent* [59] to the constraints due to a corresponding corepresentation of the little cogroup $\overline{\mathcal{G}}^{\mathbf{k}}$ (which consists of the corresponding point-group symmetries, i.e., without the translation). However, although nonsymmorphic symmetries have trivial implications for the TP classification, they may nontrivially affect the rotation eigenvalues that enter the symmetry-indicator formulas for the fractional corner and hinge charges (in particular if the rotational symmetry is replaced by a screw rotation).

Here, we argue in two steps that even in the case of a screw rotation, there is no change to the bulk-hinge correspondence derived in Sec. IV C. First, we discuss in Sec. VII A how to apply the symmetry-indicator formulas for corner charges in C_n-symmetric 2D systems [28,30] to compute momentum-resolved hinge charges in a wire geometry of 3D crystals with a screw rotation (instead of pure rotation) symmetry. Along the way, we derive that the symmetry-indicator formulas for corner charges [without assuming time-reversal symmetry (cf. Appendix A 1)] are symmetric under cyclic permutation of the rotation eigenvalues. Next, we consider in Sec. VII B the mapping of ICRs between the little group and the little cogroup of the HSL on which the TPs lie. We show that this mapping is compatible with the application of the symmetry-indicator formulas for the hinge charge, allowing us to establish the generalization of the bulk-hinge correspondence to TPPs protected by a screw symmetry.

A. Fractional hinge charges due to screw rotational symmetry

Consider any SG with a nonsymmorphic rotational symmetry around the z axis, $\{C_n|\mathbf{w}\}$, where $n = 2, 3, 4, 6$ and $\mathbf{w}$ is the nonsymmorphic translation. Note that the x, y components of $\mathbf{w}$, i.e., the ones perpendicular to the rotation axis, can be removed by shifting the rotation axis (this may potentially result in a change of the fractional translations associated with other symmetry elements in the SG, but this is not relevant for our argument). We end up with the screw symmetry $S_n = \{C_n|\frac{m}{n}\mathbf{e}_z\}$ with $m \in \mathbb{Z}$ that together with the translations $\mathbf{t} \in \mathfrak{T}$ by lattice vectors generate a subgroup G of the full SG (i.e., we drop the potentially present time-reversal symmetry as well as all point-group operations that are not generated by C_n).

Let D be the representation of G in which the eigenfunctions of the Hamiltonian transform and $D_{\mathbf{k}}$ its restriction to the $\mathbf{k}$ sector, i.e., a representation of the little group $G^{\mathbf{k}}$. Then, for any $\{R|\mathbf{v}\} \in G$,

$$D_{\mathbf{k}}(\{R|\mathbf{v}\})\mathcal{H}(R^{-1}\mathbf{k})D_{\mathbf{k}}(\{R|\mathbf{v}\})^{-1} = \mathcal{H}(\mathbf{k}). \tag{18}$$

In analogy with Sec. IV C, we take a 2D cut at fixed k_z and define the 2D Hamiltonian $\mathcal{H}_{k_z}(k_x, k_y) = \mathcal{H}(\mathbf{k})$, which still satisfies Eq. (18) at any $\mathbf{k}_{2\mathrm{D}} = (k_x, k_y)$ and for any $\{R|\mathbf{v}\} \in G$. In particular, for any 2D HSP Π invariant under S_n^ℓ for some power ℓ of the screw symmetry, where $0 < \ell < n$ is a divisor of n, $\mathcal{H}_{k_z}$ commutes with the operator $D_{\mathbf{k}}(S_n^\ell)$ which admits eigenvalues

$$s_p^{(n/\ell)} = e^{i\frac{\ell}{n}[-mk_z+2\pi(p-1)]}, \quad p = 1, 2, \ldots, \frac{n}{\ell}. \tag{19}$$

The above follows because $D_{\mathbf{k}}(S_n^\ell)$ is a representation and $(S_n^\ell)^{n/\ell} = S_n^n = \{\mathbb{1}|m\mathbf{e}_z\}$, where $m\mathbf{e}_z \in \mathfrak{T}$ is a lattice translation and therefore $D_{\mathbf{k}}(\{\mathbb{1}|m\mathbf{e}_z\}) = e^{-imk_z}\mathbb{1}$, which has eigenvalues e^{-imk_z}; thus, eigenvalues of $D_{\mathbf{k}}(S_n^\ell)$ are (n/ℓ)th roots of e^{-imk_z}.

Next, we define the operator

$$D'_{\mathbf{k}_{2\mathrm{D}}}(C_n) = e^{i\frac{1}{n}(mk_z+2\pi p')}D_{\mathbf{k}}(S_n), \tag{20}$$

which is a symmetry of the 2D Hamiltonian for any $p' \in \mathbb{Z}$:

$$D'_{\mathbf{k}_{2\mathrm{D}}}(C_n)\mathcal{H}_{k_z}(C_n^{-1}\mathbf{k}_{2\mathrm{D}})D'_{\mathbf{k}_{2\mathrm{D}}}(C_n)^{-1} = \mathcal{H}_{k_z}(\mathbf{k}_{2\mathrm{D}}). \tag{21}$$

We observe that $D'_{\mathbf{k}_{2\mathrm{D}}}(C_n)$ [together with $D'_{\mathbf{k}_{2\mathrm{D}}}(\{\mathbb{1}|\mathbf{t}_{2\mathrm{D}}\}) = D_{\mathbf{k}}(\{\mathbb{1}|\mathbf{t}_{2\mathrm{D}}\})$] furnishes a representation of the 2D space group pn (i.e., the 2D symmetry group generated by C_n rotation with respect to a point and by translations). This implies that the Hamiltonian $\mathcal{H}_{k_z}$ describes a 2D system with C_n symmetry, and that the rotation eigenvalues of its energy bands at a $C_{n/\ell}$-invariant HSP Π are

$$r_{p,p'}^{(n/\ell)} = e^{2\pi i\frac{p+p'-1}{n/\ell}}, \tag{22}$$

where we recognize $e^{2\pi i \frac{p+p'-1}{n/\ell}} = \Pi_{p+p'}^{(n/\ell)}$ as defined in Eq. (2). With these eigenvalues, the symmetry-indicator formulas for the corner charge in 2D systems with rotational symmetry C_2, C_3, C_4, and C_6 [28,30], e.g., (A1)–(A3), can be directly applied to compute the fractional hinge charges even for nonsymmorphic 3D SGs.

Note that a nontrivial symmetry of the formulas for the corner charges can now be easily deduced. Namely, the nonuniqueness of Eq. (20) due to the freedom of choosing $p' \in \mathbb{Z}$ implies that the symmetry-indicator formulas for the corner charges must be symmetric under *cyclic permutations of the rotation eigenvalues* (which correspond to the replacement $p' \mapsto p' + 1$). In particular, this applies irrespective of the nonsymmorphicity, as can be seen by setting $m = 0$ in the symmetry S_n above. We are not aware whether this symmetry has been previously pointed out, but it is easily verified explicitly for the symmetry class A (i.e., without time-reversal symmetry), which we checked using the generating Wannier configurations discussed in Appendix A of Ref. [30]. Time-reversal symmetry implies that the number of bands with rotation eigenvalues $\Pi_p^{(n/\ell)}$ and $(\Pi_p^{(n/\ell)})^*$ must match; however, this matching will generically be lost after performing a cyclic permutation of rotation eigenvalues. For this reason, the symmetry-indicator formulas derived under the assumption that time-reversal symmetry is present, i.e., Eqs. (A4) and (A5), do not manifest the symmetry under cyclic permutations of the rotation eigenvalues. If n is even, a reduced symmetry of the symmetry-indicator formulas under $p' \mapsto p' + \frac{n}{2}$ remains.

In summary, we have shown that the fractional hinge charges of nonsymmorphic crystals in wire geometry with screw symmetry $\{C_n|\frac{m}{n}\mathbf{e}_z\}$ are characterized by the same symmetry-indicator formulas that apply for corner charges in 2D systems with rotational symmetry C_n, after the k_z dependence of the screw eigenvalues is removed. It remains to be shown that this removal is compatible with the identification of ICRs of the little group with those of the little cogroup described in Ref. [59]. This task is left for Sec. VII B.

B. Bulk-hinge correspondence of TPPs

The characterization of TPs reproduced in Table I is phrased in terms of ICRs of the little *cogroup* $\overline{\mathcal{G}}^{\mathbf{k}}$ of the HSL on which the TPs lie, even though the symmetry constraints on the nodal-line structure near the TPs involve the ICRs of the little *group* $\mathcal{G}^{\mathbf{k}}$. For symmorphic SGs, this is explained by the fact that the ICRs of $\mathcal{G}^{\mathbf{k}}$ restricted to elements $\{R|0\} \in \mathcal{G}^{\mathbf{k}}$ (forming a group isomorphic to $\overline{\mathcal{G}}^{\mathbf{k}}$) are identical to the ones of $\overline{\mathcal{G}}^{\mathbf{k}}$: the ICR ς of $\mathcal{G}^{\mathbf{k}}$ is injectively mapped to the ICR ρ of $\overline{\mathcal{G}}^{\mathbf{k}}$ by

$$\forall\, \{R|0\} \in \mathcal{G}^{\mathbf{k}} : \rho(R) = \varsigma(\{R|0\}). \tag{23}$$

For nonsymmorphic SGs, on the other hand, this is not the case. Nevertheless, we have shown in Ref. [59] that for little groups that support TPs a different mapping between ICRs ς of $\mathcal{G}^{\mathbf{k}}$ restricted to $\overline{\mathcal{G}}^{\mathbf{k}}$ and ICRs ρ of $\overline{\mathcal{G}}^{\mathbf{k}}$ exists (see Appendix A in Ref. [59]): Let $\varsigma^{1\mathrm{D}}$ be any 1D ICR of $\mathcal{G}^{\mathbf{k}}$ (e.g., the one that facilitates the formation of the discussed TP), then the ICR ς of $\mathcal{G}^{\mathbf{k}}$ is injectively mapped to the ICR ρ of $\overline{\mathcal{G}}^{\mathbf{k}}$ by

$$\forall\, \{R|\mathbf{v}\} \in \mathcal{G}^{\mathbf{k}} : \rho(R) = \varsigma^{1\mathrm{D}}(\{R|\mathbf{v}\})^{-1}\varsigma(\{R|\mathbf{v}\}). \tag{24}$$

Note that, in contrast to the symmorphic case, the restriction of ς to $\overline{\mathcal{G}}^{\mathbf{k}}$ is *not* a representation of $\overline{\mathcal{G}}^{\mathbf{k}}$ but a *projective* representation.

Here, we are interested in the rotation eigenvalues at HSLs, i.e., the eigenvalues of $\rho(C_{n/\ell})$ at momenta invariant under $C_{n/\ell}$ symmetry. It follows from Eq. (24) that the eigenvalues $s^{(n/\ell)}$ of $\varsigma(S_{n/\ell})$ and $r^{(n/\ell)}$ of $\rho(C_{n/\ell})$ are related as

$$r^{(n/\ell)} = \rho^{1\mathrm{D}}(S_{n/\ell})^{-1} s^{(n/\ell)}. \tag{25}$$

However, as a 1D ICR, $\rho^{1\mathrm{D}}(S_{n/\ell})$ must be one of the eigenvalues defined in Eq. (19), i.e., $s_{\tilde{p}}^{(n/\ell)}$ for some $\tilde{p} \in \mathbb{Z}$. Then,

$$r^{(n/\ell)} = e^{i\frac{1}{n}[mk_z - 2\pi(\tilde{p}-1)]} s^{(n/\ell)}, \tag{26}$$

which is fully compatible with Eq. (20) for $p' = 1 - \tilde{p}$ in the sense that if $s^{(n/\ell)}$ is one of the eigenvalues of $D_{\mathbf{k}}(S_n)$, then $r^{(n/\ell)}$ is the corresponding eigenvalue of $D'_{\mathbf{k}_{2\mathrm{D}}}(C_n)$. In particular, we observe that the k_z dependence on the right-hand side of Eq. (26) cancels, and $r^{(n/\ell)}$ does not depend on k_z.

Given a TPP formed by four bands transforming according to certain ICRs of the little group, the relevant rotation eigenvalues used to compute the hinge-charge jump should be obtained by applying the construction described in Sec. VII A. However, the preceding paragraph implies that the same results are obtained if we first map the ICRs of the little group to ICRs of the little cogroup [cf. Eq. (24)] and then apply the symmetry-indicator formulas in (A1)–(A3) to the rotation eigenvalues obtained from the ICRs of the little cogroup. In fact, the nonuniqueness of $\rho^{1\mathrm{D}}$ in Eq. (24) (if 1D ICRs of $\mathcal{G}^{\mathbf{k}}$ exist) amounts precisely to the nonuniqueness of p' in Eq. (20), further evincing how the two presented descriptions are two facets of the same argument. We therefore conclude that both the TP types and the hinge-charge jumps can be determined from the ICRs of the little cogroup, which implies that the bulk-hinge correspondence derived in Sec. IV C directly applies to nonsymmorphic SGs as well.

VIII. TRIPLE POINTS IN SPINFUL BAND STRUCTURES

The presented analysis of the higher-order bulk-boundary correspondence of TPPs is easy to generalize to the spinful case. According to the classification of TPs by Ref. [49], in spinful systems without magnetic order, TPs can be protected on the HSLs ΓA, KH, and $K'H'$ of SGs with threefold rotational symmetry. Only two magnetic point groups (as little cogroups of HSLs) can protect TPs: C_{3v} ($3m$) resulting in type-B TPs, and C_{3v} supplemented with $m_z\mathcal{T}$ ($\bar{6}'m2'$) resulting in type-A TPs. The spinful ICRs of the two MPGs are equivalent, such that we do not need to consider them separately for the discussion of the hinge-charge jump and of the bulk-polarization jump (which only depend on the rotation eigenvalues). The main difference between the two cases is that the additional antiunitary symmetry $m_z\mathcal{T}$ in $\bar{6}'m2'$ forces the NL arcs (characteristic of type-B TPs) to coalesce on the rotation axis, resulting in the type-A TPs. For both MPGs there are two spinful 1D ICRs $\rho_1^{1\mathrm{D}}$, $\rho_2^{1\mathrm{D}}$ and only a single spinful 2D ICR $\rho^{2\mathrm{D}}$, giving rise to three different TPPs ($\rho^{2\mathrm{D}}$; $\rho_a^{1\mathrm{D}}$, $\rho_b^{1\mathrm{D}}$) with $a, b \in \{1, 2\}$. However, $\rho_1^{1\mathrm{D}}$ and $\rho_2^{1\mathrm{D}}$ have identical rotation eigenvalues; therefore, they are not

distinguished in the corresponding symmetry indicators, and they all result in the *same* value of jumps $\Delta Q_{\llcorner}$ and $\Delta\mathbf{P}$.

For simplicity, we restrict the explicit analysis to the case when the C_3 rotation center of the sample resides at the $1a$ WP (a straightforward analysis using the symmetry-indicator formulas from Ref. [30] reveals that our results remain true if the rotation center resides at WP $1b$ or $1c$). Similar to Sec. IV, we set all ionic charge to WP $1a$. Then, the corner charge on a 2D cut is given by (cf. class A in Ref. [30])

$$Q_{\llcorner}^{(3)} = \frac{e}{3}\left(\left[K_1^{(3)}\right] + \left[K_2^{(3)}\right] + \left[K_1'^{(3)}\right] + \left[K_2'^{(3)}\right]\right) \mod e. \tag{27}$$

The square brackets are defined in the exact same way as in the spinless case, $[\Pi_p^{(n)}] = \#\Pi_p^{(n)} - \#\Gamma_p^{(n)}$; however the labeling of rotation eigenvalues in Eq. (2) is replaced by

$$\Pi_p^{(n)} = e^{2\pi i(p-1)/n} e^{\pi i/n}, \quad p = 1, 2, \ldots, n. \tag{28}$$

The bulk polarization can similarly be expressed in terms of the symmetry indicators as [29,30]

$$\mathbf{P}^{(3)} = \frac{e}{3}\left(2\left[K_1^{(3)}\right] + \left[K_2^{(3)}\right] + \left[K_1'^{(3)}\right] + 2\left[K_2'^{(3)}\right]\right)(\mathbf{a}_1 + \mathbf{a}_2) \mod e\mathbf{R}. \tag{29}$$

By performing an analysis (not appended) similar to the one detailed in Appendixes A 3 and A 4 for the spinless case, we derive the bulk-hinge correspondence for spinful TPPs in triangular geometry. Independent of the HSL on which the TPP lies and regardless of the WP of the rotation center, the hinge-charge jump is universally found to be

$$\Delta Q_{\llcorner} = \frac{e}{3} \mod e \tag{30}$$

and the jump of the bulk polarization

$$\Delta\mathbf{P} = 0 \mod e\mathbf{R}. \tag{31}$$

We observe that even in spinful systems, all TPPs carry fractional hinge-charge jump.

The derived results directly apply to TPPs reported in WC-type crystalline materials reported by Ref. [49]. In particular, TaN exhibits a type-(A, A) TPP characterized by a hinge-charge jump $\frac{e}{3}$ along the ΓA line. Furthermore, this material is very close to the ideal semimetallic TPP case, with only small additional Fermi pockets around the K point and A point of the BZ. We have considered extracting the predicted hinge-charge jump for TaN from first-principles calculations (as we have done for Sc_3AlC under strain), however, the absence of a surface gap has prevented us from doing so. In the future, a systematic check of the materials that host TPPs for open surface gaps could lead to a better material candidate.

IX. CONCLUSIONS AND OUTLOOKS

In this work we exposed higher-order topological fingerprints of triple nodal points (TPs) in three dimensions (3D). Our focus has been on the *spinless case*, where one encounters an interplay of band nodes with a rich topological structure: nodal lines (NLs) can be protected by mirror (m_v) planes, NLs governed by non-Abelian topology and equipped with monopole charges can be stabilized by space-time inversion ($\mathcal{PT}$) symmetry, and either species of NLs can be pinned to high-symmetry lines (HSLs) by rotation (C_n) or antiunitary rotation ($C_n\mathcal{PT}$) symmetry. In particular, triple-point pairs [TPPs; formed when a 2D irreducible corepresentation (ICR) crosses a pair of 1D ICRs] are semimetallic features where a NL along a HSL is transferred across three adjacent energy gaps.

The rich topological structure of spinless systems supporting TPs prompted us to analyze HSLs with 13 distinct magnetic little cogroups, summarized by Table I. The main finding of our analysis is that triple-point pairs demarcated by a pair of type-A or by a pair of type-B TPs are generally characterized by a *fractional jump of the hinge charge*. These results apply also to nonsymmorphic space groups. On top of the spinless analysis, in the last section we briefly considered the *spinful case*, where TPs arise in the presence of C_{3v} symmetry, and where a fractional hinge-charge jump is also predicted to be a universal higher-order feature of TPPs. Note that while three-dimensional Weyl nodes and Dirac nodes exist in both the higher-order [40–47] and first-order [87,109] varieties, we report that *all* type-(A, A) and type-(B, B) TPPs are *universally* associated with the higher-order bulk-hinge correspondence. Our finding thus overcomes the previous unsuccessful search for a general bulk-boundary characterization of TPs in surface states [49,52,57,61], as conventionally associated with first-order topology.

Although our analysis in the presence of C_4 rotational symmetry explicitly assumed a primitive tetragonal Bravais lattice, the result in Table II generalizes *with no alterations* to the body-centered tetragonal case. To understand this, note that the derivation of the hinge-charge jump (cf. Appendix A 3 b) is based on considering a two-dimensional (2D) system with C_4 symmetry. It is found that (1) the ICRs at the Γ and at the M point of the 2D square lattice are *identical*, and that (2) the corner-charge jump associated with a band inversion of a 2D ICR with two 1D ICRs is *also identical* for both the Γ and at the M point. The 3D models with tetragonal (either primitive or body-centered) symmetry are obtained from the 2D systems by interpreting the band-inversion-tuning parameter as a third momentum component k_z. The difference between the two Bravais lattices merely corresponds to the way the periodically changing Hamiltonians $\mathcal{H}_{k_z}(\mathbf{k}_{2D}) = \mathcal{H}_{k_z+2\pi}(\mathbf{k}_{2D})$ are glued together: for the body-centered case, $\mathcal{H}_{k_z}(\mathbf{k}_{2D}) = \mathcal{H}_{k_z+\pi}(\mathbf{k}_{2D} + \Gamma - M)$, whereas such a constraint is absent for the primitive case. It is clear that the mathematical analysis of the hinge-charge jump in Sec. IV C leading to Table II applies irrespective of this additional constraint. An analogous argument in the presence of C_3 also reveals why in the trigonal case we find identical classification of TPPs along the lines Γ, K, and K'.

While the presented spinless material Sc_3AlC [57] requires unrealistic values of applied strain to realize the quantized hinge-charge jump, our analysis demonstrates that the discussed phenomenology could conceivably be realized and observed in crystalline solids if more appropriate compounds are identified in the future. Furthermore, metamaterial realizations (e.g., in acoustics, similar to those of Refs. [42,47]) are definitely feasible.

Finally, it is interesting to speculate whether a similar universal higher-order bulk-boundary correspondence extends to other previously reported one-dimensional nodal structures;

for example, aside from the nodal-line segment spanned by a TPP which has been considered by this work, nodal-line chains [66,90,110], gyroscopes [35,111,112], and starfruits [113] were proposed. They all require crossing of bands with particular choices of symmetry eigenvalues which is associated with a change of the symmetry indicators, potentially implying similar phenomenology of higher-order topological hinge-charge jumps. Given the numerous material candidates for the various nodal-line compositions, it should be of theoretical as well as of experimental interest to consider such generalizations in the future.

We provide access to all the data and code necessary to reproduce the results presented here in the supplementary data and code [114].

ACKNOWLEDGMENTS

We thank A. Bouhon, A. Skurativska, L. Trifunovic, and S. S. Tsirkin for valuable discussions. P.M.L. and T.B. were supported by the Ambizione Grant No. 185806 by the Swiss National Science Foundation. T.N. acknowledges support from the European Research Council (ERC) under the European Union's Horizon 2020 research and innovation program (Grant No. ERC-StG-Neupert-757867-PARATOP). T.B. and T.N. were supported by the NCCR MARVEL funded by the Swiss National Science Foundation. X.L. acknowledges the support by the China Scholarship Council (CSC).

APPENDIX A: CORNER AND HINGE CHARGES

In this Appendix we derive various statements presented in Sec. IV in relation to the second Stiefel-Whitney (2SW) class and hinge charges. For reference, we include the relevant symmetry-indicator formulas for the corner charge of spinless 2D systems with C_n symmetry [28,30], including both the case without (with) spinless time-reversal symmetry, in Appendix A 1. Next, in Appendix A 2 we show that in spinless 2D systems with $C_2\mathcal{T}$ and C_n symmetries, where $n = 4, 6$, the 2SW class can be written in terms of C_4 and C_6 symmetry indicators. In particular, we prove Eq. (6) from Sec. IV A. Then, in Appendix A 3 we consider triple-point pairs (TPPs), i.e., pairs of triple points (TPs) formed by consecutive triplets of bands, protected by C_n symmetry, where $n = 3, 4, 6$, in spinless systems with $\mathcal{PT}$ symmetry. We derive Table II presented in Sec. IV C which gives the jumps in the 2SW class of 2D cuts and in the hinge charge for the different combinations of irreducible corepresentations. Finally, in Appendix A 4 we discuss why TPPs are not associated with a jump in the *surface* charge.

1. Symmetry-indicator formulas for the corner charge

Here we list the symmetry-indicator formulas for the corner charges $Q^{(n)}_{\llcorner,mX}$ of 2D crystals with C_n symmetry in the corresponding geometries shown in Fig. 7(a) with the center of the sample located at the Wyckoff position (WP) mX (cf. Ref. [30] for the labeling of WPs). In all cases we assume that the ionic charges are placed at WP $1a$ and we use the notation of Ref. [28], defined in Eqs. (2) and (3), for the labeling of rotation eigenvalues and symmetry indicators.

In the absence of time-reversal symmetry (symmetry class A), Ref. [30] derives the formulas to be the following: for $n = 3$,

$$Q^{(3)}_{\llcorner,1a} = \frac{e}{3}\left(\left[K_1^{(3)}\right] + \left[K_2^{(3)}\right] + \left[K_1'^{(3)}\right] + \left[K_2'^{(3)}\right]\right) \mod e, \tag{A1a}$$

$$Q^{(3)}_{\llcorner,1b} = -\frac{e}{3}\left(\left[K_1^{(3)}\right] + \left[K_2'^{(3)}\right]\right) \mod e, \tag{A1b}$$

$$Q^{(3)}_{\llcorner,1c} = -\frac{e}{3}\left(\left[K_2^{(3)}\right] + \left[K_1'^{(3)}\right]\right) \mod e; \tag{A1c}$$

for $n = 4$,

$$Q^{(4)}_{\llcorner,1a} = \frac{e}{4}\left(-\left[X_1^{(2)}\right] + \frac{1}{2}\left[M_1^{(4)}\right] - \frac{3}{2}\left[M_3^{(4)}\right]\right) \mod e, \tag{A2a}$$

$$Q^{(4)}_{\llcorner,1b} = \frac{e}{4}\left(\left[X_1^{(2)}\right] - \frac{3}{2}\left[M_1^{(4)}\right] + \frac{1}{2}\left[M_3^{(4)}\right]\right) \mod e; \tag{A2b}$$

and for $n = 6$,

$$Q^{(6)}_{\llcorner,1a} = -\frac{e}{6}\left(2\left[K_1^{(3)}\right] + \frac{3}{2}\left[M_1^{(2)}\right]\right). \tag{A3}$$

If spinless time-reversal symmetry $\mathcal{T}$ satisfying $\mathcal{T}^2 = +\mathbb{1}$ is present, i.e., in symmetry class AI, the formulas simplify due to constraints on the topological invariants $[\Pi_p^{(n)}]$ [30]. In our work, this case only occurs for $n = 4$,

$$Q^{(4)}_{\llcorner,1a} = \frac{e}{4}\left(-\left[X_1^{(2)}\right] + 2\left[M_1^{(4)}\right] + 3\left[M_2^{(4)}\right]\right) \mod e, \tag{A4a}$$

$$Q^{(4)}_{\llcorner,1b} = \frac{e}{4}\left(\left[X_1^{(2)}\right] + 2\left[M_1^{(4)}\right] + 3\left[M_2^{(4)}\right]\right) \mod e, \tag{A4b}$$

and for $n = 6$,

$$Q^{(6)}_{\llcorner,1a} = \frac{e}{4}\left[M_1^{(2)}\right] + \frac{e}{6}\left[K_1^{(3)}\right] \mod e. \tag{A5}$$

Finally, we also need the formula for $n = 2$, which is given in Ref. [28]:

$$Q^{(2)}_{\llcorner,1a} = \frac{e}{4}\left(-\left[X_1^{(2)}\right] - \left[Y_1^{(2)}\right] + \left[M_1^{(2)}\right]\right) \mod e. \tag{A6}$$

2. Stiefel-Whitney insulators with rotational symmetry

a. C_4 symmetry

We first consider C_4 symmetry. The four time-reversal-invariant momenta are Γ, X, X', and M, where X and X' are equivalent. According to Eq. (5) a nontrivial 2SW class is equivalent to

$$\left\lfloor \tfrac{1}{2}\#\Gamma_2^{(2)} \right\rfloor + 2\left\lfloor \tfrac{1}{2}\#X_2^{(2)} \right\rfloor + \left\lfloor \tfrac{1}{2}\#M_2^{(2)} \right\rfloor = 1 \mod 2. \tag{A7}$$

This does not constrain $\#X_2^{(2)}$ at all, but it is equivalent to either

$$\left\lfloor \tfrac{1}{2}\#\Gamma_2^{(2)} \right\rfloor = 0 \mod 2 \wedge \left\lfloor \tfrac{1}{2}\#M_2^{(2)} \right\rfloor = 1 \mod 2$$
$$\Leftrightarrow \quad \#\Gamma_2^{(2)} \in \{0, 1\} \mod 4 \wedge \#M_2^{(2)} \in \{2, 3\} \mod 4$$
$$\Rightarrow \quad \#M_2^{(2)} - \#\Gamma_2^{(2)} =: \left[M_2^{(2)}\right] \in \{1, 2, 3\} \mod 4$$

or the same with Γ and M exchanged, where the latter implies $[M_2^{(2)}] \in \{1, 2, 3\} \mod 4$ as well. Thus, $w_2 = 1$ implies

$[M_2^{(2)}] \in \{1, 2, 3\} \mod 4$. On the other hand, $w_2 = 0$ implies

$$\lfloor \tfrac{1}{2}\#\Gamma_2^{(2)} \rfloor = \lfloor \tfrac{1}{2}\#M_2^{(2)} \rfloor \mod 2$$
$$\Rightarrow \quad \big[M_2^{(2)}\big] \in \{0, 1, 3\} \mod 4.$$

Furthermore, time reversal combined with C_4 symmetry imply [28] that $[M_2^{(4)}] = [M_4^{(4)}]$, such that together with $[M_2^{(2)}] = [M_2^{(4)}] + [M_4^{(4)}]$ (which follows from $C_4^2 = C_2$) we find

$$\big[M_2^{(2)}\big] = 2\big[M_2^{(4)}\big]. \tag{A8}$$

Therefore, $[M_2^{(2)}]$ has to be even. Since we already restricted $[M_2^{(2)}]$ for $w_2 = 1$ to the set $\{1, 2, 3\} \mod 4$ (and to the set $\{0, 1, 3\} \mod 4$ for $w_1 = 0$), selecting the even element of the corresponding set results in

$$w_2 = \tfrac{1}{2}\big[M_2^{(2)}\big] \mod 2 = \big[M_2^{(4)}\big] \mod 2. \tag{A9}$$

Finally, using Eq. (A9) and assuming vanishing bulk polarization, $[X_1^{(2)}] = 0$ [28], we can rewrite Eq. (4a) as

$$Q_{\llcorner}^{(4)} = \frac{e}{4}\big(2\big[M_1^{(4)}\big] + 3w_2\big) \mod \frac{e}{2}. \tag{A10}$$

We observe that for $w_2 = 1$ the term in the brackets is an odd integer, while it is an even integer for $w_2 = 0$. This restricts the fractional part of $Q_{\llcorner}^{(4)}$ to $\pm\frac{e}{4}$ in the first, and to 0 or $\frac{e}{2}$ in the second case.

b. C_6 symmetry

Next, we consider C_6 symmetry, where the four time-reversal-invariant momenta are Γ, M, M', and M'' with the latter three being equivalent. Correspondingly,

$$\lfloor \tfrac{1}{2}\#\Gamma_2^{(2)} \rfloor + 3\lfloor \tfrac{1}{2}\#M_2^{(2)} \rfloor = 1 \mod 2. \tag{A11}$$

A nontrivial value $w_2 = 1$ implies, in analogy with the analysis of the C_4-symmetric case, that

$$\big[M_2^{(2)}\big] \in \{1, 2, 3\} \mod 4, \tag{A12}$$

while $w_2 = 0$ implies

$$\big[M_2^{(2)}\big] \in \{0, 1, 3\} \mod 4. \tag{A13}$$

For the next step in our reasoning we need to apply the following property: if $[M_1^{(2)}] = 1 \mod 2$, then the bulk is necessarily gapless. This can be seen as follows. By assumption, the number of occupied bands with C_2-rotation eigenvalue 1 changes by an odd number between Γ and M:

$$\#M_1^{(2)} - \#\Gamma_1^{(2)} = [M_1^{(2)}] = 1 \mod 2. \tag{A14}$$

Since the C_2 symmetry acts as inversion on the 1D BZ segment $\Gamma M \Gamma$, Eq. (A14) implies [34] that the occupied bands carry a total Berry phase π on that segment. We further consider the triangle formed by the $\Gamma M \Gamma$ paths of the three BZs around a K point, as illustrated in Fig. 21. Due to the sixfold rotational symmetry the three sides of the triangle all contribute $\pi \mod 2\pi$ to the Berry phase, such that the total Berry phase along the triangular contour is $\pi \mod 2\pi$, indicating that there are an odd number of band nodes (formed *between* the occupied and the unoccupied bands) inside the triangle, i.e., the bulk is gapless. Conversely, a gapped bulk implies $[M_1^{(2)}] = 0 \mod 2$. Noting that $[M_1^{(2)}] = -[M_2^{(2)}]$ (because $\sum_{p=1}^{n}[\Pi_p^{(n)}] = 0$ [28]), an insulating bulk band structure equivalently requires $[M_2^{(2)}]$ to be even. Therefore,

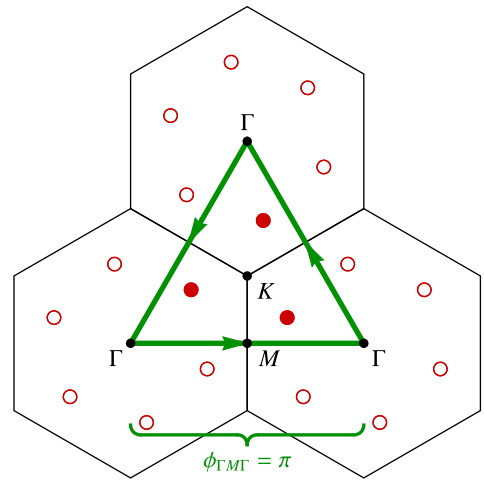

FIG. 21. Three hexagonal Brillouin zones around a K point of a C_6-symmetric model. Assuming $[M_1^{(2)}] = 1 \mod 2$ the total Berry phase $\phi_{\Gamma M\Gamma}$ of the occupied bands along the closed contour $\Gamma M \Gamma$ equals π (cf. Appendix A 2 b). Therefore, the Berry phase along the triangular contour (green) is also $\phi_{\triangle} = 3\pi = \pi \mod 2\pi$. The result implies that the triangle encloses an odd number of band nodes in the principal gap (red disks), i.e., the system is *not an insulator*.

$$w_2 = \tfrac{1}{2}\big[M_1^{(2)}\big] \mod 2. \tag{A15}$$

Using Eq. (A15) (and noting that for C_6-symmetric systems the bulk polarization *always* vanishes [28]), we can rewrite Eq. (4b) for the corner charge as

$$Q_{\llcorner}^{(6)} = \frac{e}{6}\big(\big[K_1^{(3)}\big] + 3w_2\big) \mod e. \tag{A16}$$

It follows from time-reversal symmetry that at HSPs states have either real rotation eigenvalues or come in pairs with complex-conjugate rotation eigenvalues. In particular, this implies that $[K_2^{(3)}] = [K_3^{(3)}]$ and because of the same number of filled bands at points K and Γ, it follows that

$$\big[K_1^{(3)}\big] = -\big[K_2^{(3)}\big] - \big[K_3^{(3)}\big] = 0 \mod 2, \tag{A17}$$

i.e., $[K_1^{(3)}]$ is an even integer. Thus, the term in brackets in Eq. (A16) is an odd integer for $w_2 = 1$ and an even integer for $w_2 = 0$. This restricts $Q_{\llcorner}^{(6)}$ to $\pm\frac{e}{6}$ or $\frac{e}{2}$ in the first case, and to 0 or $\pm\frac{e}{3}$ in the second case.

3. Hinge-charge jump and 2SW monopole due to triple points

We start from the classification of TPs in spinless $\mathcal{PT}$-symmetric systems as presented in Ref. [60] for little cogroups $\overline{\mathcal{G}}^{\mathbf{k}} = C_{3(v)}, C_{4(v)}, C_{6(v)}$ of some high-symmetry line (HSL) and we consider the situation depicted in Fig. 9. We compare quantities in the orange k_z range (to the left of the first TP, where the 2D ICR ρ^{2D} is occupied) and the blue k_z range (to the right of the second TP, where the two 1D ICRs ρ_a^{1D} and ρ_b^{1D} are occupied). For the ICRs the notation of Ref. [65] is used. In particular, when defining the changes $\Delta Q_{\llcorner}$ and Δw_2, we subtract the first (orange k_z range) from the latter (blue k_z range). For each 2D or 1D ICR ρ of $\overline{\mathcal{G}}^{\mathbf{k}} \cup (\mathcal{PT})\overline{\mathcal{G}}^{\mathbf{k}}$,

TABLE IV. Rotation eigenvalues and symmetry indicators for all irreducible corepresentations of $C_{3(v)}$ with $\mathcal{PT}$ at a high-symmetry point $\Pi = \Gamma, K, K'$ of a C_3-symmetric system or at $\Pi = K$ of a C_6-symmetric system. The list of ICRs is unchanged if $\mathcal{PT}$ symmetry is removed in the case of C_{3v}.

ICRs for		Eigenvalue of	Symmetry indicators at Π	
C_{3v}	C_3	C_3	$\#\Pi_1^{(3)}$	$\#\Pi_2^{(3)}$
A_1, A_2	A_1	1	1	0
E	${}^2E^1E$	$e^{2\pi i/3}, e^{-2\pi i/3}$	0	1

we look up the corresponding rotation eigenvalues on the Bilbao crystallographic server (BCS) [103–105] using the program COREPRESENTATIONS PG [82,83] and, assuming there are no other band inversions in the principal gap, compute the relevant symmetry indicators (see Tables IV, V,and VII). Before proceeding with the mathematical analysis, we make two remarks. First, note that the HSL on which the TPs lie does not need to go through the center of the BZ (point Γ of the 2D cut). Namely, the little cogroup $C_{3(v)}$ is also realized at the K point(s) of space groups (SGs) with threefold or sixfold rotational symmetry, while $C_{4(v)}$ is also realized at M points of SGs with fourfold rotational symmetry.

In all cases we assume that the SG contains $\mathcal{PT}$, acting as $(C_2\mathcal{T})_{2D}$ in the 2D cuts, and C_n with order $n \in \{3, 4, 6\}$. Furthermore, we place all ionic charge at the center of the unit cell because, ultimately, we are interested in the change of the corner charge as a function of k_z and the ionic charge distribution does not depend on k_z. If the system symmetry is C_3, then $\mathcal{T}_{2D}$ ($= C_2\mathcal{PT} = m_z\mathcal{T}$) is not present, such that the corner charge is given by Eq. (A1). For SG symmetries with rotation of order $n = 4, 6$, the C_2 combines with $\mathcal{PT}$ to give $C_2\mathcal{PT} = \mathcal{T}_{2D}$, such that we can apply the simplified formulas (A4) and (A5). For the 2SW class, we use the results of the previous subsection, i.e., Eqs. (A9) and (A15).

We next go in detail through all the possible cases.

a. Triple points along $C_{3(v)}$-symmetric lines

For $C_{3(v)}$ there is only one possible configuration of two TPs, namely, the one with ICRs $(E; A, A)$. The symmetry indicators (cf. Table IV) imply that $\Delta\#\Pi_1^{(3)} = 2$ and $\Delta\#\Pi_2^{(3)} = -1$.

Let us first consider TPs occurring along the HSL $\Pi = \Gamma$ of a C_3-symmetric system. If the rotation center of the sample lies at WP $1a$, then $\Delta[K_p^{(3)}] = \Delta[K_p'^{(3)}] = -\Delta\#\Gamma_p^{(3)}$. Then, according to Eq. (A1a), the hinge-charge jump is

$$\Delta Q_{\llcorner,1a}^{(3)} = -\frac{2e}{3}\left(\Delta\#\Gamma_1^{(3)} + \Delta\#\Gamma_2^{(3)}\right) \mod e = \frac{e}{3} \mod e. \tag{A18}$$

If the TPs instead occur along HSL $\Pi = K$ (or equivalently K') of a C_3-symmetric system (with rotation center still set to $1a$, then $\Delta[K_p^{(3)}] = \Delta\#K_p^{(3)}$ such that

$$\Delta Q_{\llcorner,1a}^{(3)} = \frac{e}{3}\left(\Delta\#K_1^{(3)} + \Delta\#K_2^{(3)}\right) \mod e = \frac{e}{3} \mod e. \tag{A19}$$

It is easily verified by using Eqs. (A1b) and (A1c) that the derived results for $\Delta Q_{\llcorner}$ remain unchanged if the rotation center of the finite system is instead located at WP $1b$ or $1c$.

If $\Pi = K$ of a C_6-symmetric system, then we need to use Eq. (A5) instead, resulting in the same

$$\Delta Q_{\llcorner}^{(6)} = \frac{e}{6}\Delta\#K_1^{(3)} \mod e = \frac{e}{3} \mod e. \tag{A20}$$

This concludes the derivation of $\Delta Q_{\llcorner}^{(n)} = \frac{e}{3} \mod e$ for TPPs along $C_{3(v)}$-symmetric lines.

We briefly analyze the jump Δw_2 of the 2SW class. We have argued in Sec. IV C and demonstrated in Sec. V D that the 2SW class is not symmetry indicated for C_3-symmetric systems. For C_6, on the other hand, we use Eq. (A15) to find

$$\Delta w_2 = \tfrac{1}{2}\Delta\left[M_1^{(2)}\right] = 0, \tag{A21}$$

because, by assumption, there is neither a band inversion at Γ nor at M.

b. Triple points along $C_{4(v)}$-symmetric lines

Next, we consider $C_{4(v)}$-symmetric lines with ICRs and symmetry indicators given in Table V. Here, we need to distinguish three TP configurations [namely, $(E; A, A)$, $(E; B, B)$, and $(E; A, B)$] and two HSLs (namely, $\Pi = \Gamma$ and K). The differences $\Delta\#\Pi_1^{(2)}$, $\Delta\#\Pi_1^{(4)}$, and $\Delta\#\Pi_2^{(4)}$ for the various TP configurations are listed in Table VI. By recalling Eq. (A9), we find that for all cases

$$\Delta w_2 = \Delta\left[M_2^{(4)}\right] \mod 2 = 1 \mod 2, \tag{A22}$$

in agreement with the fact that the TPs are type A (cf. Sec. III A).

To identify the jump in the hinge charge, we have to analyze the two HSLs separately. First, for $\Pi = \Gamma$ we have $\Delta[\mathrm{P}_p^{(n)}] = -\Delta\#\Gamma_p^{(n)}$ for both $\mathrm{P} \in \{K, M\}$, and the change in corner charge is given by

$$\Delta Q_{\llcorner}^{(4)} = -\frac{e}{4}\left(\mp\Delta\#\Gamma_1^{(2)} + 2\Delta\#\Gamma_1^{(4)} + 3\Delta\#\Gamma_2^{(4)}\right) \mod e, \tag{A23}$$

where the negative (positive) sign of $\Delta\#\Gamma_1^{(2)}$ corresponds to setting the center of the system to WP $1a$ ($1b$). Observe in Table V that $\Delta\Pi_1^{(2)}$ is *even* for all TPPs, which means that the "$\mp$" sign ambiguity is unimportant, and both WPs lead to the same value of the hinge-charge jump.

In contrast, for $\Pi = M$ we obtain contributions from $\Delta[M_p^{(4)}] = \Delta\#M_p^{(4)}$, leading to

$$\Delta Q_{\llcorner}^{(4)} = \frac{e}{4}\left(2\Delta\#M_1^{(4)} + 3\Delta\#M_2^{(4)}\right) \mod e. \tag{A24}$$

Careful evaluation of Eqs. (A23), (A24), and (A32) for all combinations of ICRs gives the following results: For TPPs

TABLE V. Rotation eigenvalues and symmetry indicators for all irreducible corepresentations of $C_{4(v)}$ with $\mathcal{PT}$ at a high-symmetry point $\Pi = \Gamma, M$ of a C_4-symmetric system. The list of ICRs is unchanged if $\mathcal{PT}$ symmetry is removed in the case of C_{4v}.

ICRs for		Eigenvalues of		Symmetry indicators at Π		
C_{4v}	C_4	C_2	C_4	$\#\Pi_1^{(2)}$	$\#\Pi_1^{(4)}$	$\#\Pi_2^{(4)}$
A_1, A_2	A	1	1	1	1	0
B_1, B_2	B	1	-1	1	0	0
E	E	$-1, -1$	$i, -i$	0	0	1

TABLE VI. Changes in symmetry indicators ($\Delta\#\Pi_p^{(n)}$), hinge charge ($\Delta Q_{\llcorner}^{(4)}$) and second Stiefel-Whitney class (Δw_2) associated with the different configurations of triple-point pairs (TPPs). Each TPP is specified by the irreducible corepresentations (ICRs) (ρ^{2D}; ρ_a^{1D}, ρ_b^{1D}) on a fourfold rotation axis, corresponding to the high-symmetry point $\Pi = \Gamma, M$ in a 2D cut perpendicular to the rotation axis. The changes are defined by subtracting the characteristics of the systems with ρ^{2D} occupied from those of the system with $\rho_{a,b}^{1D}$ occupied. The hinge-charge jump is computed using Eq. (A23) for $\Pi = \Gamma$ and Eq. (A24) for $\Pi = M$, while Δw_2 is computed from Eq. (A9).

ICRs	$(E;A,A)$	$(E;B,B)$
$\Delta\#\Pi_1^{(2)}$	2	2
$\Delta\#\Pi_1^{(4)}$	2	0
$\Delta\#\Pi_2^{(4)}$	-1	-1
$\Delta Q_{\llcorner}^{(4)}$ mod e	$+\frac{e}{4}$	$+\frac{e}{4}$
Δw_2 mod 2	1	1

along either Γ or M, $\Delta Q_{\llcorner}^{(4)} = \frac{e}{4}$ for both $(E;A,A)$ and $(E;B,B)$. The results are summarized in Table VI.

c. *Triple points along $C_{6(v)}$-symmetric lines*

There is only one HSL with little cogroup $C_{6(v)}$ (namely, Γ in C_6-symmetric systems), and considering the possible crossings of ICRs (listed in Table VII) results in six distinct TPP configurations. We first focus on the cases where the two TPs are of the same type, which gives the four TPPs listed in Table VIII. By combining $\Delta[\Pi_p^{(n)}] = -\Delta\#\Gamma_p^{(n)}$ (for $\Pi \in \{M, K\}$) with Eqs. (A5) and (A15), we calculate the jumps

$$\Delta Q_{\llcorner}^{(6)} = -\frac{e}{4}\Delta\#\Gamma_1^{(2)} - \frac{e}{6}\Delta\#\Gamma_1^{(3)} \quad \text{mod } e, \tag{A25}$$

$$\Delta w_2 = -\frac{1}{2}\Delta\#\Gamma_1^{(2)} \quad \text{mod } 2. \tag{A26}$$

The computed values of $\Delta Q_{\llcorner}^{(6)}$ and of Δw_2 for all the TPPs where both TPs are of the same type are listed in Table VIII. We find that a nontrivial change of the 2SW class, which occurs for two type-A TPs, is associated with a hinge-charge jump $\Delta Q_{\llcorner}^{(6)} = +\frac{e}{6}$. In contrast, pairs of type-B TPs are characterized by trivial $\Delta w_2 = 0$ and are associated with a hinge-charge jump of $\Delta Q_{\llcorner}^{(6)} = -\frac{e}{3}$.

TABLE VII. Rotation eigenvalues and symmetry indicators for all irreducible corepresentations of $C_{6(v)}$ with $\mathcal{PT}$ at the high-symmetry point Γ of a C_6-symmetric system. The list of ICRs is unchanged if $\mathcal{PT}$ symmetry is removed in the case of C_{6v}.

ICRs for		Eigenvalues of		Symmetry indicators at Γ	
C_{6v}	C_6	C_2	C_3	$\#\Gamma_1^{(2)}$	$\#\Gamma_1^{(3)}$
A_1, A_2	A	1	1	1	1
B_1, B_2	B	-1	1	0	1
E_1	${}^2E_2^1E_2$	$-1, -1$	$e^{2\pi i/3}, e^{-2\pi i/3}$	0	0
E_2	${}^2E_1^1E_1$	1, 1	$e^{2\pi i/3}, e^{-2\pi i/3}$	2	0

TABLE VIII. Changes in symmetry indicators ($\Delta\#\Gamma_1^{(n)}$), hinge charge ($\Delta Q_{\llcorner}^{(6)}$), and second Stiefel-Whitney class (Δw_2) associated with the different configurations of triple-point pairs (TPPs) along the Γ line of C_6-symmetric systems. Each TPP is specified by the irreducible corepresentations (ICRs) (ρ^{2D}; ρ_a^{1D}, ρ_b^{1D}) along the Γ line. For simplicity we use the labels of ICRs for C_{6v}, the corresponding notation for C_6 can be extracted from Table VII. The changes are defined by subtracting the characteristics of the systems with ρ^{2D} occupied from those of the system with $\rho_{a,b}^{1D}$ occupied. The values of $\Delta Q_{\llcorner}^{(6)}$ and Δw_2 are computed from Eq. (A25) and (A26), respectively.

TP types	(A, A)		(B, B)	
ICRs	$(E_1;A_i,A_j)$	$(E_2;B_i,B_j)$	$(E_1;B_i,B_j)$	$(E_2;A_i,A_j)$
$\Delta\#\Gamma_1^{(2)}$	2	-2	0	0
$\Delta\#\Gamma_1^{(3)}$	2	2	2	2
$\Delta Q_{\llcorner}^{(6)}$ mod e	$+\frac{e}{6}$	$+\frac{e}{6}$	$-\frac{e}{3}$	$-\frac{e}{3}$
Δw_2 mod 2	1	1	0	0

Finally, there is the possibility to have two TPs of *different types*, i.e., one type A and one type B, by choosing one of the following ICR combinations: $(E_1;A_i,B_j)$, $(E_2;A_i,B_j)$. In these two cases, we find that $\Delta[M_1^{(2)}] = -\Delta\#\Gamma_1^{(2)} = 1$ mod 2 (i.e., it is an *odd number*). This implies that the value of $[M_1^{(2)}]$ must be odd on one side of the TPP. However, recall from Appendix A 2 that a gapped bulk requires $[M_1^{(2)}] = 0$ mod 2. It therefore follows that the bulk is necessarily gapless on one side of the TPP, such that the hinge-charge jump cannot be defined in this case. This finding is consistent with the intuitive explanation given in the main text, where the different type of the two TPs forces the attached NL arcs to cross the orange or blue k_z range. In Fig. 10(c). a 2D cut in the orange k_z range would correspond to the situation shown in Fig. 21 with the red disks corresponding to places where the red attached NL arcs cross the 2D cut.

4. No jump of the surface charge due to triple points

For the hinge-charge jump to be observable, it is important that the surface charge (more precisely, the surface charge *density*; this corresponds to the edge charge density of the 2D cuts at fixed k_z) is vanishing [28] for the k_z ranges on both sides of the TPP. This can only be true if the *jump* of the surface charge associated with the TPP is zero. Here we show that this is indeed true for all the TPPs shown in Table II.

Before deriving the desired fact mathematically from the corresponding symmetry-indicator formulas, let us present a simple argument based on the quantization of Berry phase. Namely, recall that for a boundary of a high-symmetry orientation with respect to the crystalline axes, the surface charge is in a one-to-one correspondence [81] with the Berry phase along a closed momentum-space ($\mathbf{k}$) path along the direction perpendicular to the considered surface. Here, first recall [59,60] that stable TPs require the presence of either $\mathcal{PT}$ symmetry (in which case the Berry phase is quantized to 0 vs π on *any* closed $\mathbf{k}$ path due to the reality condition [68]) or of m_v mirror symmetry (in which case the mirror symmetry acts like inversion on the straight $\mathbf{k}$ paths perpendicular to the

boundaries considered in Figs. 2, 14, and 15, thus quantizing the Berry phase of interest to 0 vs π [115]).

The quantization of the Berry phase implies that the surface charge can only change if the $\mathbf{k}$ paths of the required orientation encounter a bulk nodal line (carrying the π quantum of Berry phase). However, a look at Fig. 10 reveals that for both type-(A, A) and type-(B, B) TPPs it is possible to continuously shift a horizontal $\mathbf{k}$ path from the orange k_z range to the blue k_z range without encountering any (red) nodal line in the principal gap. We therefore anticipate the surface charge to be identical in both k_z ranges (and therefore the hinge-charge jump to be observable) at least when the boundaries are oriented symmetrically with respect to the crystal axes.

More formally, we now derive the same conclusion for an *arbitrarily* oriented C_n-symmetric system. In such a case the surface charge density of a gapped 2D crystal is given [80] by $\sigma_{\text{surf}} = \mathbf{P}\cdot\hat{\mathbf{n}}$, where $\mathbf{P}$ is the bulk polarization and $\hat{\mathbf{n}}$ the surface normal. To prove that $\Delta\sigma_{\text{surf}} = 0$ across the TPP for arbitrary boundary termination, it needs to be true that $\Delta\mathbf{P}\cdot\hat{\mathbf{n}} = 0$ when moving across the TPP. Similar to the corner charge, the bulk polarization $\mathbf{P}^{(n)}$ of a 2D crystal with C_n rotational symmetry can be expressed [28–30] using symmetry indicators. For C_3-symmetric crystals, we use the result of Refs. [29,30] which does not assume time-reversal symmetry to be present,

$$\mathbf{P}^{(3)} = \frac{e}{3}\big(2\big[K_1^{(3)}\big] + \big[K_1'^{(3)}\big] + \big[K_2^{(3)}\big] + 2\big[K_2'^{(3)}\big]\big)(\mathbf{a}_1+\mathbf{a}_2) \mod e\mathbf{R}, \tag{A27}$$

while for C_n with $n = 4, 6$, we can use the simplified expressions from Ref. [28]:

$$\mathbf{P}^{(4)} = \frac{e}{2}\big[X_1^{(2)}\big](\mathbf{a}_1+\mathbf{a}_2) \mod e\mathbf{R}, \tag{A28}$$

$$\mathbf{P}^{(6)} = 0 \mod e\mathbf{R}. \tag{A29}$$

Here, $\mathbf{a}_1$ and $\mathbf{a}_2$ are lattice basis vectors and $\mathbf{R} = m_1\mathbf{a}_1 + m_2\mathbf{a}_2$ with $m_1, m_2 \in \mathbb{Z}$ is a general Bravais lattice vector.

We now briefly apply the symmetry-indicator formulas in Appendix A 4 [Eq. (A29)] to show that the polarization jump $\Delta\mathbf{P}^{(n)}$ associated with the TPPs in C_n-symmetric systems is always vanishing. First, for a TPP along the Γ line of a C_3-symmetric system [cf. Eq. (A18)], we obtain from Appendix A 4 the jump of the bulk polarization

$$\Delta\mathbf{P}^{(3)} = -e\big(\Delta\#\Gamma_1^{(3)} + \Delta\#\Gamma_2^{(3)}\big)(\mathbf{a}_1+\mathbf{a}_2) \mod e\mathbf{R} = 0 \mod e\mathbf{R}. \tag{A30}$$

Similarly, for a TPP along the K line [cf. Eq. (A19)]

$$\Delta\mathbf{P}^{(3)} = \frac{e}{3}\big(2\Delta\#K_1^{(3)} + \Delta\#K_2^{(3)}\big)(\mathbf{a}_1+\mathbf{a}_2) \mod e\mathbf{R} = 0 \mod e\mathbf{R}, \tag{A31}$$

where we have read from Table IV that $\Delta\#K_1^{(3)} = 2$ and $\Delta\#K_2^{(3)} = -1$ for a TPP formed by ICRs $(E; A_i, A_j)$.

Furthermore, note that per Appendix A 4 the polarization always vanishes in C_6-symmetric systems. Therefore, $\Delta\mathbf{P}^{(6)} = 0 \mod e\mathbf{R}$ for TPPs along both the K line [cf. Eq. (A20)] and the Γ line [cf. Eq. (A25)] of C_6-symmetric systems. Next, for TPPs along the Γ line of C_4-symmetric systems [cf. Eq. (A23)] we find from Eq. (A28) that the change in bulk polarization is

$$\Delta\mathbf{P}^{(4)} = -\frac{e}{2}\Delta\#\Gamma_1^{(2)}(\mathbf{a}_1+\mathbf{a}_2) \mod e\mathbf{R} = 0 \mod e\mathbf{R}, \tag{A32}$$

where we have read from Table VI that $\Delta\#\Gamma_1^{(2)}$ is even for all possible TPPs. Finally, note that TPPs along the M line [cf. Eq. (A24)] do not have an effect on the symmetry indicator $[X_1^{(2)}]$ in Eq. (A28), therefore, again $\Delta\mathbf{P}^{(4)} = 0 \mod e\mathbf{R}$. We conclude that all TPPs listed in Table II are associated with no jump in surface charge, thus making the hinge-charge jump observable for an appropriate choice of the boundary termination.

APPENDIX B: EULER MONOPOLE CHARGE IN THE PRESENCE OF ROTATIONAL SYMMETRY

In this Appendix we derive the statements made in Sec. IV B and apply them to triple-point pairs (TPPs) to find the combinations of irreducible corepresentations (ICRs) that necessarily lead to a gapless bulk on at least one side of the TPP. Such TPPs cannot be associated with a higher-order signature on the wire hinges; for brevity, we call them *inadmissible TPP configurations*. For the remaining cases, we determine the value of the Euler monopole charge given in Table II. The analysis assumes the presence of space-time inversion ($\mathcal{PT}$) symmetry unless explicitly stated otherwise (a particular case of the latter is the entire Appendix B 5).

The presented arguments are based on analyzing the spectrum of Wilson-loop operators on certain appropriately chosen paths. The Wilson-loop operators are defined in terms of projectors onto occupied eigenstates $|u_i(\mathbf{k})\rangle$ of the Bloch Hamiltonian $\mathcal{H}(\mathbf{k})$. We organize the occupied eigenstates into an $N \times N_{\text{occ}}$ matrix

$$\mathsf{u}(\mathbf{k}) = (|u_1(\mathbf{k})\rangle \quad |u_2(\mathbf{k})\rangle \quad \ldots \quad |u_{N_{\text{occ}}}(\mathbf{k})\rangle), \tag{B1}$$

where N is the total number of bands and N_{occ} is the number of occupied bands. In the presence of $\mathcal{PT}$ symmetry satisfying $(\mathcal{PT})^2 = +\mathbb{1}$, we always adopt a basis of the Hilbert space in which $\mathcal{PT}$ is represented by complex conjugation $\mathcal{K}$. Then, the Bloch Hamiltonian is a real-symmetric matrix, and the eigenstates [as well as the matrix $\mathsf{u}(\mathbf{k})$] can be gauged to be real. To determine the advertised properties of TPPs, we need to study how the spectrum of the Wilson operator on certain appropriately chosen paths is constrained by $\mathcal{PT}$, m_v, and C_n symmetries.

The discussion in this Appendix is structured as follows. In Appendix B 1 we study how C_n rotational symmetry constrains the Wilson-loop operator on an appropriately chosen path, composed of two C_n-related segments. Next, in Appendix B 2, we use the previous result to relate the Berry phase of the occupied bands on a particular choice of path to the C_n eigenvalues of the occupied bands at the high-symmetry line, and in Appendix B 3 we derive a symmetry-indicator formula for the Euler monopole charge. Then, in Appendix B 4, we apply the previous two results to TPPs, identifying which TPPs are inadmissible and giving the Euler monopole charge for each admissible TPP configuration. Finally, in Appendix B 5

we extend the discussion of inadmissible TPPs to systems without $\mathcal{PT}$ symmetry.

1. Symmetry constraint on Wilson-loop operator

We define the following family of closed contours

$$\Gamma(\phi) = \gamma(\phi)^{-1} \circ \gamma(0) \tag{B2}$$

consisting of half circles given by $\gamma(\phi) : \theta \in [0, \pi] \mapsto \gamma(\theta, \phi)$ with

$$\gamma(\theta, \phi) = R \begin{pmatrix} \sin(\theta)\cos(\phi) \\ \sin(\theta)\sin(\phi) \\ -\cos(\theta) \end{pmatrix}. \tag{B3}$$

One example of such a contour is illustrated in Fig. 8 in green color. We abbreviate $\mathsf{u}(\theta, \phi) = \mathsf{u}(\gamma(\theta, \phi))$, $\mathsf{u}_0 = \mathsf{u}(0, \phi)$, and $\mathsf{u}_1 = \mathsf{u}(\pi, \phi)$ for any $\phi \in [0, 2\pi)$.

Given any closed path $\Gamma(t)$ defined on $t \in [0, 1]$, the Wilson-loop operator is defined by

$$\mathcal{W}(\Gamma)_{mn} = \lim_{\delta t \to 0} \left\langle u_m(\Gamma(1)) \middle| \prod_t^{1 \leftarrow 0} \mathbb{P}(\Gamma(t)) \middle| u_n(\Gamma(0)) \right\rangle, \tag{B4}$$

where δt is the discretization of t in the product, the arrow over the product symbol indicates the ordering of the factors from small to large values of t (i.e., in this case factors with smaller t are to the right), and

$$\mathbb{P}(\mathbf{k}) = \sum_{j=1}^{N_{\text{occ}}} |u_j(\mathbf{k})\rangle\langle u_j(\mathbf{k})| \tag{B5}$$

is the projector onto the occupied subspace. Observing that

$$\mathsf{u}(\mathbf{k})\mathsf{u}(\mathbf{k})^\dagger = \sum_{j=1}^{N_{\text{occ}}} |u_j(\mathbf{k})\rangle\langle u_j(\mathbf{k})| = \mathbb{P}(\mathbf{k}), \tag{B6}$$

we can rewrite the expression for the Wilson-loop operator in matrix form ($\mathcal{W}$ is an $N_{\text{occ}} \times N_{\text{occ}}$ matrix)

$$\mathcal{W}(\Gamma) = \lim_{\delta t \to 0} \mathsf{u}(\Gamma(1))^\dagger \prod_t^{1 \leftarrow 0} \mathsf{u}(\Gamma(t))\mathsf{u}(\Gamma(t))^\dagger \mathsf{u}(\Gamma(0)). \tag{B7}$$

The Wilson-loop operator for one of the closed contours $\Gamma(\phi)$ defined above is then found to be

$$\begin{aligned} \mathcal{W}(\phi) &= \mathcal{W}(\Gamma(\phi)) \\ &= \lim_{\delta\theta \to 0} \mathsf{u}_0^\dagger \left[\prod_\theta^{0 \to \pi} \mathsf{u}(\theta, \phi)\mathsf{u}(\theta, \phi)^\dagger \right] \\ &\quad \times \left[\prod_\theta^{\pi \leftarrow 0} \mathsf{u}(\theta, 0)\mathsf{u}(\theta, 0)^\dagger \right] \mathsf{u}_0. \end{aligned} \tag{B8}$$

Reordering the terms in the products, this becomes

$$\begin{aligned} &= \lim_{\delta\theta \to 0} \mathsf{u}_0^\dagger \mathsf{u}_0 \left[\prod_\theta^{0 \to \pi - \delta\theta} \mathsf{u}(\theta, \phi)^\dagger \mathsf{u}(\theta + \delta\theta, \phi) \right] \mathsf{u}_1^\dagger \\ &\quad \times \mathsf{u}_1 \left[\prod_\theta^{\pi - \delta\theta \leftarrow 0} \mathsf{u}(\theta + \delta\theta, 0)^\dagger \mathsf{u}(\theta, 0) \right] \mathsf{u}_0 \\ &= \lim_{\delta\theta \to 0} \left[\prod_\theta^{0 \to \pi - \delta\theta} V(\theta, \phi)^\dagger \right] \left[\prod_\theta^{\pi - \delta\theta \leftarrow 0} V(\theta, 0) \right] \mathsf{u}_0 \end{aligned} \tag{B9}$$

with

$$V(\theta, \phi) = \mathsf{u}(\theta + \delta\theta, \phi)^\dagger \mathsf{u}(\theta, \phi). \tag{B10}$$

If we choose the real gauge along $\Gamma(\phi)$ by monodromy, $V(\theta, \phi) \in \mathsf{SO}(N_{\text{occ}})$.

The C_n rotational symmetry relates eigenstates at points in momentum space related by that symmetry:

$$\mathsf{u}(C_n\mathbf{k}) = D(C_n)\mathsf{u}(\mathbf{k})\mathcal{B}(\boldsymbol{k}), \tag{B11}$$

where $D(C_n)$ is the corepresentation matrix of C_n in the chosen basis, i.e., where $D(\mathcal{PT}) = \mathbb{1}$, and $\mathcal{B}(\boldsymbol{k}) \in \mathsf{O}(N_{\text{occ}})$ is a sewing matrix [33]. Thus, for any θ, ϕ,

$$\mathsf{u}\left(\theta, \phi + \frac{2\pi}{n}\right) = D(C_n)\mathsf{u}(\theta, \phi)\mathcal{B}(\theta, \phi). \tag{B12}$$

Substituting this into the expression for the Wilson-loop operator, we find

$$\begin{aligned} \mathcal{W}\left(\phi + \frac{2\pi}{n}\right) &= \lim_{\delta\theta \to 0} \mathsf{u}_0^\dagger \left[\prod_\theta^{0 \to \pi} D(C_n)\mathsf{u}(\theta, \phi)\mathsf{u}(\theta, \phi)^\dagger D(C_n)^\dagger \right] \\ &\quad \times \left[\prod_\theta^{\pi \leftarrow 0} \mathsf{u}(\theta, 0)\mathsf{u}(\theta, 0)^\dagger \right] \mathsf{u}_0, \end{aligned} \tag{B13}$$

where the sewing matrices canceled out. Reordering the terms again,

$$\begin{aligned} &= \lim_{\delta\theta \to 0} \mathsf{u}_0^\dagger D(C_n)\mathsf{u}_0 \left[\prod_\theta^{0 \to \pi - \delta\theta} \mathsf{u}(\theta, \phi)^\dagger \mathsf{u}(\theta + \delta\theta, \phi) \right] \\ &\quad \times \mathsf{u}_1^\dagger D(C_n)^\dagger \mathsf{u}_1 \left[\prod_\theta^{\pi - \delta\theta \leftarrow 0} \mathsf{u}(\theta + \delta\theta, 0)^\dagger \mathsf{u}(\theta, 0) \right] \mathsf{u}_0. \end{aligned} \tag{B14}$$

Note that

$$\begin{aligned} \mathsf{u}_0^\dagger D(C_n)\mathsf{u}_0 &= D_0(C_n), \\ \mathsf{u}_1^\dagger D(C_n)\mathsf{u}_1 &= D_1(C_n) \end{aligned} \tag{B15}$$

gives the corepresentation matrices $D_{0,1}(C_n)$ of only the occupied bands at $\Gamma(0)$ and $\Gamma(1/2)$ (i.e., at the south and north pole), respectively. Thus,

$$\begin{aligned} \mathcal{W}\left(\phi + \frac{2\pi}{n}\right) &= \lim_{\delta\theta \to 0} D_0(C_n) \left[\prod_\theta^{0 \to \pi - \delta\theta} V(\theta, \phi)^\dagger \right] \\ &\quad \times D_1(C_n)^\dagger \left[\prod_\theta^{\pi - \delta\theta \leftarrow 0} V(\theta, 0) \right] \mathsf{u}_0. \end{aligned} \tag{B16}$$

Defining

$$P(\phi) = \left[\prod_\theta^{\pi - \delta\theta \leftarrow 0} V(\theta, \phi) \right] \in \mathsf{SO}(N_{\text{occ}}), \tag{B17}$$

we arrive at Eq. (9) of Sec. IV B:

$$\mathcal{W}\left(\phi + \frac{2\pi}{n}\right) = D_0(C_n)P(\phi)^\dagger D_1(C_n)^\dagger P(\phi)\mathcal{W}(\phi). \tag{B18}$$

2. Berry phase on a symmetric path

The constraint on the Wilson-loop operator derived above has implications for the Berry phase of the occupied bands computed on the contours $\Gamma(\phi)$. The Berry phase is given by $\varphi = \arg\det \mathcal{W}$, such that

$$\varphi\left(\phi + \frac{2\pi}{n}\right) = \arg\det\left[D_0(C_n)P(\phi)^\dagger D_1(C_n)^\dagger P(\phi)\mathcal{W}(\phi)\right].$$

Using that inside the determinant all matrices commute,

$$\begin{aligned} &= \arg\det \mathcal{W}(\phi) + \arg\det\left[D_0(C_n)D_1(C_n)^\dagger\right] \\ &= \varphi(\phi) + \arg\det\left[D_0(C_n)D_1(C_n)^\dagger\right] \mod 2\pi, \end{aligned} \tag{B19}$$

which is exactly Eq. (10). The difference in Berry phase on the two contours is found to be

$$\Delta\varphi = \arg\det\left[D_0(C_n)D_1(C_n)^\dagger\right]. \tag{B20}$$

Recall that in the presence of $\mathcal{PT}$ symmetry, the Berry phase on any closed loop is (as well as their differences) quantized to 0 vs π, and that the Berry curvature vanishes identically away from the nodal lines [68]. It therefore follows that the trivial value $\Delta\varphi = 0$ indicates that there is an *even* number of nodal lines enclosed by the contour $\gamma(\phi + 2\pi/n)^{-1} \circ \gamma(\phi)$, while a nontrivial value $\Delta\varphi = \pi$ indicates an *odd* number. This implies that each $\frac{2\pi}{n}$ sector of the spherical surface is penetrated by an even (odd) number of nodal lines in the principal gap and thus, if $\Delta\varphi = \pi$, that the surface *must* contain gapless points.

3. Symmetry indicators for Euler monopole charge

We now specialize to the case where $N_{\mathrm{occ}} = 2$ and assume that $D_{0,1}(C_n) \in \mathsf{SO}(2)$. Since the nth power of $D_{0,1}(C_n)$ gives the identity, it follows that for $j \in \{0, 1\}$,

$$D_j(C_n) = e^{-\frac{2\pi i}{n} r_j s_y} \quad \text{with} \quad r_j \in \mathbb{Z} \tag{B21}$$

and Pauli matrices s_i acting on the space of the two valence bands. Because $\mathsf{SO}(2)$ is an Abelian group, we find that

$$\begin{aligned} \mathcal{W}\left(\phi + \frac{2\pi}{n}\right) &= D_0(C_n)D_1(C_n)^\dagger \lim_{\delta\theta\to 0}\left[\prod_\theta^{0\to\pi-\delta\theta} V(\theta,\phi)^\dagger\right] \\ &\quad\times\left[\prod_\theta^{\pi-\delta\theta\leftarrow 0} V(\theta,0)\right]\mathsf{u}_0 \\ &= D_0(C_n)D_1(C_n)^\dagger\mathcal{W}(\phi). \end{aligned} \tag{B22}$$

From the family of Wilson-loop operators $\mathcal{W}(\phi)$ for $\phi \in [0, 2\pi)$, the Euler class can be obtained [73]. Since $\mathcal{W}(\phi) \in \mathsf{SO}(2)$, there is a $\zeta(\phi) \in [0, 2\pi)$ such that

$$\mathcal{W}(\phi) = e^{i\zeta(\phi)s_y} \tag{B23}$$

given by the Pfaffian of the logarithm

$$\zeta(\phi) = \mathrm{Pf}[\log\mathcal{W}(\phi)] \mod 2\pi. \tag{B24}$$

The phase $\zeta(\phi)$ changes continuously in ϕ as long as the two-band subspace is separated from the other bands by energy gaps, and its winding number determines the Euler class as

$$\chi = \frac{1}{2\pi}\int_0^{2\pi}\frac{d\zeta(\phi)}{d\phi} = \frac{1}{2\pi}[\zeta(2\pi) - \zeta(0)]. \tag{B25}$$

We remark that the above expression should be read with caution. Namely, a gauge transformation $\mathsf{u}_0 \mapsto \mathsf{u}_0 U$ with $U \in \mathsf{O}(2)$ at the base point of the closed path Γ transforms the Wilson-loop operator as follows:

$$\mathcal{W}(\phi) \mapsto U^\top\mathcal{W}(\phi)U, \tag{B26}$$

such that $\zeta(\phi) \mapsto \zeta'(\phi)$ with

$$\begin{aligned} \zeta'(\phi) &= \mathrm{Pf}\left\{\log\left[U^\top\mathcal{W}(\phi)U\right]\right\} \mod 2\pi \\ &= \mathrm{Pf}\left\{U^\top\log\left[\mathcal{W}(\phi)\right]U\right\} \mod 2\pi. \end{aligned}$$

Using that $\mathrm{Pf}(BAB^\top) = \det(B)\mathrm{Pf}(A)$, we obtain

$$= \det(U)\zeta(\phi) \mod 2. \tag{B27}$$

Since $\det(U) = \pm 1$, the sign of $\zeta(\phi)$ and therefore χ is gauge dependent [73]. Therefore, the well-defined topological invariant that we can extract is the *absolute value* $|\chi|$ of the Euler monopole charge.

Equation (B22) implies that

$$\begin{aligned} \zeta\left(\phi + \frac{2\pi}{n}\right) &= \mathrm{Pf}\left[\log e^{\frac{2\pi i}{n}(r_1 - r_0)s_y + i\zeta(\phi)s_y}\right] \\ &= \frac{2\pi}{n}(r_1 - r_0) + \zeta(\phi) \mod 2\pi \end{aligned} \tag{B28}$$

and applying that identity n times gives

$$\zeta(\phi + 2\pi) = 2\pi(r_1 - r_0) + \zeta(\phi) \mod 2\pi. \tag{B29}$$

Therefore, the Euler class is

$$\chi = r_1 - r_0 \mod n. \tag{B30}$$

Recall that the parity of χ is the second Stiefel-Whitney class

$$w_2 = \chi \mod 2. \tag{B31}$$

Observe that, for odd n, Eq. (B30) leaves the parity of χ undetermined. It follows that for C_3, w_2 is not constrained by symmetry, which is consistent with what we demonstrated in Sec. V D.

4. Application to triple-point pairs

We apply the above results to TPPs formed by a 2D ICR $\rho^{2\mathrm{D}}$ and two 1D ICRs $\rho_a^{1\mathrm{D}}$, $\rho_b^{1\mathrm{D}}$. In that case the representation matrices of C_n in the orange and blue k_z ranges appearing in Eqs. (B19) and (B30) are

$$\begin{aligned} D_0(C_n) &= \rho^{2\mathrm{D}}(C_n), \\ D_1(C_n) &= \rho_a^{1\mathrm{D}}(C_n) \oplus \rho_b^{1\mathrm{D}}(C_n), \end{aligned} \tag{B32}$$

respectively. For the relevant point groups stabilizing TPs in the presence of $\mathcal{PT}$ symmetry, Table IX lists the representation matrices for all 1D and 2D ICRs.

In Appendix B 2 we have derived a necessary condition for the enclosing spherical surface (on which the Wilson=loop operators are computed) to be gapped. Substituting Eq. (B32) into Eq. (B19), we find that the condition

$$\arg\det\left[\rho^{2\mathrm{D}}(C_n)\rho_a^{1\mathrm{D}}(C_n)^\dagger \oplus \rho_b^{1\mathrm{D}}(C_n)^\dagger\right] = 0 \tag{B33}$$

TABLE IX. Irreducible corepresentations (ICRs) of the C_n rotational symmetry in the point groups $C_{n(v)}$ with space-time inversion symmetry $\mathcal{PT}$ for $n \in \{3, 4, 6\}$. The notation for the ICRs follows Ref. [65], where we drop the subscripts if they do not affect the result. Note that for the 2D ICRs of the point group $C_{6(v)}$ we define ${}^2E_2\,{}^1E_2 \mapsto E_1$ and ${}^2E_1\,{}^1E_1 \mapsto E_2$. The 2D ICRs are all $\mathsf{SO}(2)$ matrices and are therefore given in the form $e^{-\frac{2\pi i}{n} r s_y}$ for $r \in \mathbb{Z}$ and the Pauli matrix s_y.

$C_{6(v)}$	ICR	A	B	E_1	E_2
	$\rho(C_6)$	1	-1	$e^{-\frac{2\pi i}{6} s_y}$	$e^{-\frac{2\pi i}{6} 2 s_y}$
$C_{4(v)}$	ICR	A	B	E	
	$\rho(C_4)$	1	-1	$e^{-\frac{2\pi i}{4} s_y}$	
$C_{3(v)}$	ICR	A		E	
	$\rho(C_3)$	1		$e^{-\frac{2\pi i}{3} s_y}$	

is equivalent to

$$\det \rho^{2D}(C_n) = \rho_a^{1D}(C_n)\rho_b^{1D}(C_n). \tag{B34}$$

According to Table IX, all 2D ICRs have determinant 1, such that Eq. (B34) is violated by all combinations of ICRs that involve two 1D ICRs with *different* rotation eigenvalue. For C_4 symmetries this excludes $(E; A, B)$ and for C_6 $(E_i; A, B)$ with $i = 1, 2$. (Note that we have dropped subscripts at A and B where they do not make a difference; this convention is also adopted in Tables II, IX, and X.)

Finally, we apply Eq. (B30) to all admissible combinations of ICRs from Table IX, i.e., where the 1D ICRs have *equal* rotation eigenvalues. In all those cases both $\rho^{2D}(C_n)$ and $\rho_a^{1D}(C_n) \oplus \rho_b^{1D}(C_n)$ are indeed $\mathsf{SO}(2)$ matrices. The results are shown in Table X. Note that (i) only the absolute value of the Euler class is well defined since the sign is gauge dependent, and (ii) the symmetry-indicator formula determines the Euler monopole charge modulo n, where n is the order of the rotational symmetry. Due to these these ambiguities, $\{0, 1, \ldots, \lfloor \frac{n}{2} \rfloor\}$ is the largest set of unique values of the Euler monopole charge that can be distinguished based on the ICRs of the two valence bands. More precisely, all values of χ such that $\chi = mn \pm p$ (with n the order of the rotational symmetry, p an element of the just specified set, and $m \in \mathbb{Z}$) are not distinguishable from $\chi = p$. With the convention that $a \mod n \in (-\lfloor n/2 \rfloor, \ldots, \lfloor n/2 \rfloor]$, we write $|\chi \mod n|$ to indicate the representative of the corresponding equivalence class of all such indistinguishable values of χ.

In particular, for $n = 6$, values $|\chi| = 4$ and $|\chi| = 5$ are indistinguishable from $|\chi| = 2$ and $|\chi| = 1$, respectively; while for $n = 4$, the value $|\chi| = 3$ is indistinguishable from $|\chi| = 1$. For these two cases the parity of χ is well defined, such that the 2SW monopole charge, given by $w_2 = \chi \mod 2 \in \mathbb{Z}_2$, is uniquely determined. In contrast, for $n = 3$, the symmetry-indicator formula for χ can only distinguish values $|\chi| = 0$ and $|\chi| = 1$, with $|\chi| = 2$ being indistinguishable from $|\chi| = 1$. This implies that the parity is not fixed by the symmetry indicators and therefore the 2SW monopole charge in C_3-symmetric models is not determined from the symmetry eigenvalues.

TABLE X. Euler class and second Stiefel-Whitney class computed on a surface enclosing a triple-point pair for all possible combinations of irreducible corepresentations (ICRs) in systems with space-time inversion symmetry $\mathcal{PT}$ squaring to the identity and assuming that on that surface the two-band subspace of occupied bands is separated from the remaining bands by energy gaps. Combinations of ICRs leading necessarily to a gapless bulk below or above the TPP are excluded. The first column gives the order n of rotational symmetry protecting the triple points. In the second column we list possible combinations of one 2D and two 1D ICRs, where the notation follows Ref. [65]. Note that we drop the subscript of the ICRs if the choice of the subscript does not affect the result. Furthermore, for the 2D ICRs of the point group $C_{6(v)}$ we define ${}^2E_2\,{}^1E_2 \mapsto E_1$ and ${}^2E_1\,{}^1E_1 \mapsto E_2$. For convenience we repeat the results on triple-point type for the given combinations of ICRs in the third column. Finally, we give Euler class χ and the second Stiefel-Whitney class w_2 in the last two columns.

n	ICRs	Type	$\lvert\chi \mod n\rvert$[a]	w_2
6	$(E_1; A, A)$	(A, A)	1	1
	$(E_1; B, B)$	(B, B)	2	0
	$(E_2; A, A)$	(B, B)	2	0
	$(E_2; B, B)$	(A, A)	1	1
4	$(E; A, A)$	(A, A)	1	1
	$(E; B, B)$	(A, A)	1	1
3	$(E; A, A)$	(B, B)	1 or 2[b]	1 or 0[b]

[a]Here we use the convention that $a \mod n \in (-\lfloor n/2 \rfloor, \ldots, \lfloor n/2 \rfloor]$, such that $|a \mod n| \in \{0, 1, \ldots, \lfloor n/2 \rfloor\}$, see text.

[b]Explicitly, we find $\chi = -1$, which cannot be distinguished from 2. However, because χ is only well defined up to a sign, the Euler class could also take the value 1. This implies that the parity of the Euler class is not uniquely determined by the symmetry indicator and thus the second Stiefel-Whitney class is not constrained by C_3 symmetry.

5. Gaplessness in absence of $\mathcal{PT}$ symmetry

Here, we discuss the implications of Eq. (B19) (the derivation of which only assumes the C_n rotational symmetry) in the *absence* of $\mathcal{PT}$ symmetry. By adjusting a few steps leading to Eq. (B20), one should recognize that the Berry phase on any closed loop of the form $\Lambda(n, \phi) = \gamma(\phi + 2\pi/n)^{-1} \circ \gamma(\phi)$ (and assuming the trajectory does not encounter nodes in the principal gap) is given by

$$\varphi_n = \arg \det[D_0(C_n) D_1(C_n)^\dagger], \tag{B35}$$

independent of ϕ. In the presence of $\mathcal{PT}$, we have argued that the Berry phase on any closed path [including the phase φ_n on $\Lambda(n, \phi)$] is quantized to 0 vs π, and that $\varphi_n = \pi$ implies an odd number of nodal lines to pass through the loop. If $\mathcal{PT}$ is absent but vertical mirror symmetries (m_v) are present, then an analogous quantization of Berry phase can be established for loops that are symmetric under mirror reflection [115–117], and nodal lines can only be stabilized inside mirror planes. In this case, a π Berry phase implies that the mirror-symmetric loop encloses an odd number of nodal lines inside the mirror-invariant plane. (The cases with neither $\mathcal{PT}$ nor m_v are dealt with trivially towards the end of this section.)

In the relevant magnetic point groups with rotational symmetry C_n, with vertical mirror symmetry, but without $\mathcal{PT}$ symmetry (cf. Table I), we can therefore choose ϕ such that

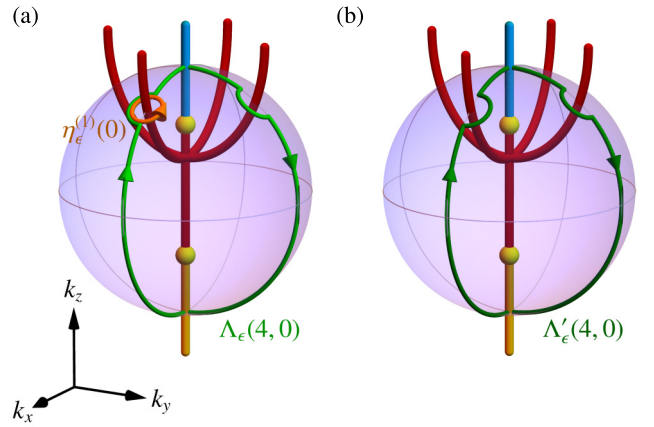

FIG. 22. Illustration of the closed loops considered in Appendix B 5 for the particular case $n = 4$. (a) The contour $\Lambda_\epsilon(n,\phi)$ (green) consists of two rotation-related semicircular arcs inside rotation-related mirror planes (here m_x and m_y). If mirror-protected nodal lines occur along the contour, we avoid them with infinitesimal half-circles perpendicular to the mirror plane containing the avoided nodal lines. The infinitesimal circular contour $\eta_\epsilon^{(1)}(\phi)$ enclosing the nodal line is illustrated as a dark orange ring; it is symmetric under m_y. (b) Composition of $\Lambda_\epsilon(n,\phi)$ with $\eta_\epsilon^{(1)}(\phi)$ results in the new contour $\Lambda'_\epsilon(n,\phi)$, which is symmetric under the diagonal mirror symmetry $m_{\bar{x}y}$.

$\gamma(\phi)$ lies within one of the mirror planes m_1, $\gamma(\phi + 2\pi/n)$ in its copy m_1' related by C_n symmetry, and the two parts of the contour are mapped onto each other by the mirror symmetry with mirror plane m_2 lying between m_1 and m_1'. However, we need to be more careful because ϕ is now fixed to a mirror plane and therefore $\gamma(\phi)$ might contain band nodes in the principal gap.

If $\gamma(\phi)$ does not contain any band nodes, then $\varphi_n = \pi$ implies that m_2 contains an odd number of nodal lines as illustrated in Fig. 8(b) for $\Lambda(4,0) = \Gamma(2\pi/4)$. On the other hand, if $\gamma(\phi)$ does contain M_1 band nodes, we exclude them by modifying γ to γ_ϵ such that the band nodes are circumvented (but enclosed by the loop) with infinitesimal half-circles [see Fig. 22(a)]. Now $\Lambda_\epsilon(n,\phi) = \gamma_\epsilon(\phi + 2\pi/n)^{-1} \circ \gamma_\epsilon(\phi)$ is not mirror symmetric anymore, but it is still composed of two segments related by rotational symmetry; therefore, the Berry phase on $\Lambda_\epsilon(n,\phi)$ is still φ_n. We next compose $\Lambda_\epsilon(n,\phi)$ with an infinitesimal circular contour $\eta_\epsilon^{(i)}(\phi)$ around each excluded band node on $\gamma_\epsilon(\phi)$ such that the resulting loop $\Lambda'_\epsilon(n,\phi)$ does *not* include the band nodes anymore. Observe that this new path is mirror symmetric with respect to m_2, and its Berry phase is therefore quantized to $\{0,\pi\}$ [cf. Fig. 22(b)]. Additionally, the Berry phase on $\eta_\epsilon^{(i)}(\phi)$ is quantized as well and is indeed π because it is itself mirror symmetric (albeit with respect to m_1 rather than m_2) and by assumption it encloses exactly one band node. Thus, the Berry phase on $\Lambda'_\epsilon(n,\phi)$ satisfies

$$\varphi_n' = \varphi_n + M_1\pi \mod 2\pi \tag{B36}$$

and it determines the parity of the number M_2 of nodal lines in the mirror plane m_2, i.e.,

$$\varphi_n' = (M_2 \mod 2)\pi. \tag{B37}$$

By combining the previous two equations, we obtain

$$\varphi_n = (M_1 + M_2 \mod 2)\pi, \tag{B38}$$

meaning that $\varphi_n \in \{0,\pi\}$ determines the parity of the number of nodal lines in mirror planes m_1 and m_2 together, i.e., exactly the ones passing through a $\frac{2\pi}{n}$ sector of the enclosing sphere, just as in the presence of $\mathcal{PT}$.

Let us finally remark that for TPs stabilized by $C_n\mathcal{PT}$ with $n = 4, 6$, we only need to consider the case *with* mirror symmetry because if no mirror symmetry is present, then nodal lines cannot be stabilized away from the rotation axis (see also the discussion in Sec. IV D). Therefore, there are no stable band nodes bound to the enclosing sphere. But, the case of $C_n\mathcal{PT}$ and mirror symmetry reduces to the case $C_{n'}$ with $n' = n/2 \in \{2, 3\}$ and mirror symmetry that we have discussed in the previous two paragraphs.

In conclusion, we have shown that even in the absence of $\mathcal{PT}$ symmetry,

$$\det \rho^{2D}(C_n) \neq \rho_a^{1D}(C_n)\rho_b^{1D}(C_n) \tag{B39}$$

implies that the bulk in the orange or blue k_z ranges is necessarily gapless. It remains to check this condition for all possible combinations of ICRs. To that end, recall from Sec. IV D that in the presence of vertical mirror symmetry, addition of $\mathcal{PT}$ does not change the ICRs and Table IX still applies, giving the same result as in the presence of $\mathcal{PT}$. The only remaining cases are the magnetic point groups $\bar{4}'2'm$ and $\bar{6}'m2'$. For the former we find $\det \rho^{2D}(C_2) = 1$, $\rho_{a,b}^{1D}(C_2) = 1$ and for the latter $\det \rho^{2D}(C_3) = 1$, $\rho_{a,b}^{1D}(C_3) = 1$, such that in both cases none of the combinations of ICRs are necessarily gapless.

APPENDIX C: TIGHT-BINDING MODELS

1. Construction of minimal tight-binding models

To construct the three tight-binding models discussed in Sec. V, we proceed as follows. We first choose a point group (D_{4h} and D_{6h} for our models) containing the little cogroup $\overline{\mathcal{G}}^{\mathbf{k}}$ which we want to protect the triple points (TPs) as a subgroup. The choice of orbitals determines the irreducible representations of the point group. Using the 3D GENPOS application on the Bilbao crystallographic server (BCS), we determine a set of possible generators of that point group, and then find their matrix representations using the REPRESENTATIONS PG application [106]. To find the ICRs corresponding to the irreducible representations of the chosen orbitals after inclusion of $\mathcal{PT}$ symmetry with $(\mathcal{PT})^2 = +\mathbb{1}$, we follow Ref. [65]. Given the set of generators, their ICRs and a generating set of hopping vectors, we use the Python package QSYMM [118] to construct a family of symmetry-allowed Bloch Hamiltonians.

Finally, we tune the parameters in that family of Hamiltonians such that we obtain a four-band triple-point pair (TPP), accompanied by the minimal number of additional nodal lines (NLs). This is achieved by first introducing a double-band inversion at Γ by setting selected intraorbital hopping parameters to be nonvanishing, and then by adding interorbital terms until we gap out all band nodes that are not required by the symmetry or topology. Note that the type of the TPs can be predicted using our previously developed classification [60].

Using topological quantum chemistry (TQC) and the BANDREP application on BCS [38,106,119], we deduce the ICRs at the high-symmetry points, and using the COMPATIBILITY RELATIONS [106] infer the ones along the relevant rotation axis.

2. Details of the discussed tight-binding models

Here, we provide details of the models studied in Sec. V. For each model we present the Hamiltonian, the basis in which the Hamiltonian is expressed, the numerical values of parameters considered in the main text, and the matrix representations that we used to construct the models (cf. Appendix C 1).

a. C_6-symmetric model with two type-A triple points

The model discussed in Sec. V B has SG $P6/mmm$ (No. 191) and is defined on a hexagonal lattice with lattice constants $a = c = 1$. As described in the main text, we place $(d_{xy}, d_{x^2-y^2})$ and $f_{x(x^2-3y^2)}$, $f_{y(3x^2-y^2)}$ orbitals at Wyckoff position (WP) $1a$ (site-symmetry group D_{6h}). We adopt the basis $(d_{xy}, d_{x^2-y^2}, if_{x(x^2-3y^2)}, if_{y(3x^2-y^2)})$, such that $\mathcal{PT}$ is represented simply by complex conjugation. According to TQC such a placement of orbitals results in the irreducible representations $(E_{2g}; B_{1u}, B_{2u})$ of D_{6h} with unchanged ICRs after adding $\mathcal{PT}$. In the above basis, the generators of D_{6h} have matrix representations

$$C_{6z} = \mathrm{diag}(R(-2\pi/3), -\mathbb{1}_\tau), \tag{C1a}$$
$$m_v = \sigma_z \otimes \tau_z, \tag{C1b}$$
$$\mathcal{P} = \sigma_z \otimes \mathbb{1}_\tau, \tag{C1c}$$
$$\mathcal{PT} = \mathcal{K}, \tag{C1d}$$

where $m_v : y \to -y$ and $R(\theta)$ is the 2D rotation matrix

$$R(\theta) = \begin{pmatrix} \cos\theta & -\sin\theta \\ \sin\theta & \cos\theta \end{pmatrix}. \tag{C2}$$

The Pauli matrices σ_i act on the d vs f (i.e., angular momentum) degree of freedom, while τ_i act on the two-level degrees of freedom with a fixed angular momentum.

Including only the nearest neighbor in plane as well as the nearest vertical hopping terms, the model's Bloch Hamiltonian can be written as

$$\begin{aligned}\mathcal{H}^{(6)}_{\mathsf{AA}}(\mathbf{k}) = &-\Big[t_1 + 2t_2\Big(\cos k_x + 2\cos\frac{k_x}{2}\cos\frac{\sqrt{3}k_y}{2}\Big)\\ &\frac{\sqrt{3}}{2} + t_3\cos k_z\Big]\gamma_3 - t_4(\gamma_{14} - \gamma_{25})\\ &- t_5\Big[\Big(\cos k_x - \cos\frac{k_x}{2}\cos\frac{\sqrt{3}k_y}{2}\Big)(\gamma_{14} + \gamma_{25})\\ &- \sqrt{3}\sin\frac{k_x}{2}\sin\frac{\sqrt{3}k_y}{2}(\gamma_{15} - \gamma_{24})\Big]\\ &- 2t_6\Big[\sin\frac{k_x}{2}\Big(2\cos\frac{k_x}{2} + \cos\frac{\sqrt{3}k_y}{2}\Big)\gamma_1\\ &- \sqrt{3}\cos\frac{k_x}{2}\sin\frac{\sqrt{3}k_y}{2}\gamma_2\Big],\end{aligned} \tag{C3}$$

with the gamma matrices defined in Sec. II. We tune the parameters to $t_1 = 3$, $t_2 = -\frac{1}{2}$, $t_3 = -2$, $t_4 = \frac{1}{4}$, $t_5 = \frac{1}{6}$, and $t_6 = -\frac{1}{3}$ to obtain a double-band inversion at Γ and no other band inversions. The resulting band structure is shown in Fig. 14(a).

b. C_6-symmetric model with two type-B triple points

The second C_6-symmetric model, discussed in Sec. V C, has the same space group (SG) $P6/mmm$ (No. 191) and is also defined on a hexagonal lattice with lattice constants $a = c = 1$. However, the d orbitals are replaced by p orbitals, such that we place (p_x, p_y) and $f_{x(x^2-3y^2)}$, $f_{y(3x^2-y^2)}$ at WP $1a$. We adopt the basis $(ip_x, ip_y, if_{x(x^2-3y^2)}, if_{y(3x^2-y^2)})$. According to TQC, this results in the irreducible representations $(E_{1u}; B_{1u}, B_{2u})$ of D_{6h}, again with unchanged ICRs after adding $\mathcal{PT}$. In the above basis, the generators of D_{6h} have matrix representations

$$C_{6z} = \mathrm{diag}(R(2\pi/6), -\mathbb{1}_\tau), \tag{C4a}$$
$$m_v = \mathrm{diag}(\tau_x, -\tau_z), \tag{C4b}$$
$$\mathcal{P} = -\mathbb{1}_\sigma \otimes \mathbb{1}_\tau, \tag{C4c}$$
$$\mathcal{PT} = \mathcal{K}, \tag{C4d}$$

where Pauli matrices σ_i act on the p vs f (i.e., angular momentum) degree of freedom, while τ_i act on the two-level degrees of freedom with a fixed angular momentum.

The model's Bloch Hamiltonian with only the nearest neighbor in plane and the nearest vertical hopping terms is

$$\begin{aligned}\mathcal{H}^{(6)}_{\mathsf{BB}}(\mathbf{k}) = &-\Big[t_1 + 2t_2\Big(\cos k_x + 2\cos\frac{k_x}{2}\cos\frac{\sqrt{3}k_y}{2}\Big)\\ &\frac{\sqrt{3}}{2} + t_3\cos k_z\Big]\gamma_3 - t_4(\gamma_{14} - \gamma_{25})\\ &- t_5\Big[\Big(\cos k_x - \cos\frac{k_x}{2}\cos\frac{\sqrt{3}k_y}{2}\Big)(\gamma_{15} - \gamma_{24})\\ &+ \sqrt{3}\sin\frac{k_x}{2}\sin\frac{\sqrt{3}k_y}{2}(\gamma_{14} + \gamma_{25})\Big]\\ &- \sqrt{2}t_6\Big[\Big(\cos k_x - \cos\frac{k_x}{2}\cos\frac{\sqrt{3}k_y}{2}\Big)(\gamma_1 - \gamma_2)\\ &- \sqrt{3}\sin\frac{k_x}{2}\sin\frac{\sqrt{3}k_y}{2}(\gamma_1 + \gamma_2)\Big],\end{aligned} \tag{C5}$$

with the gamma matrices defined in Sec. II. We set the model parameters to $t_1 = 4$, $t_2 = -\frac{2}{3}$, $t_3 = -3$, $t_4 = -\frac{1}{2}$, $t_5 = -\frac{1}{3}$, and $t_6 = \frac{6}{5}$, which results in the band structure plotted in Fig. 15(a).

c. C_3-symmetric models

The C_3-symmetric models of Sec. V D are obtained by starting from either Eq. (C3) or Eq. (C5) and adding the

following perturbations to the Hamiltonian:

$$\Delta\mathcal{H}^{(3)}_{\mathsf{AA}}(\mathbf{k}) = \delta_{C_3}\begin{pmatrix}1 & 0\\ 0 & 0\end{pmatrix}\otimes\left[\begin{pmatrix}-173\,\sin k_x & 0\\ 0 & 2\,\sin\frac{k_x}{2}\left(58\,\cos\frac{k_x}{2}+115\,\cos\frac{\sqrt{3}k_y}{2}\right)\end{pmatrix}+200\,\cos\frac{k_x}{2}\,\sin\frac{\sqrt{3}k_y}{2}\,\tau_x\right]\sin k_z \quad \text{(C6)}$$

and

$$\Delta\mathcal{H}^{(3)}_{\mathsf{BB}}(\mathbf{k}) = U_{\mathsf{BB}}\,\Delta\mathcal{H}^{(3)}_{\mathsf{AA}}(\mathbf{k})U^{\dagger}_{\mathsf{BB}}, \quad \text{(C7)}$$

where

$$U_{\mathsf{BB}} = \frac{1}{\sqrt{2}}\begin{pmatrix}1 & -1\\ 1 & 1\end{pmatrix}\otimes\begin{pmatrix}1 & 0\\ 0 & 0\end{pmatrix}+\mathbb{1}\otimes\begin{pmatrix}0 & 0\\ 0 & 1\end{pmatrix}, \quad \text{(C8)}$$

respectively, resulting in the Hamiltonians $\mathcal{H}^{(3)}_{\mathsf{AA}}(\mathbf{k})$ and $\mathcal{H}^{(3)}_{\mathsf{BB}}(\mathbf{k})$ whose NL structure is shown in Figs. 16(a) and 16(d), respectively. Note that, in contrast to the C_6-symmetric models, the subscript of the Hamiltonian does *not* denote the types of TPs because a C_3-symmetric little cogroup only allows for type-B TPs [60]. Instead, the subscript indicates from which C_6-symmetric model the corresponding C_3-symmetric model is derived.

APPENDIX D: COMPUTATION OF THE CORNER CHARGES

In this Appendix we provide technical details on some of the methods used in the extraction of the corner charges from the charge distribution obtained from exact diagonalization of the tight-binding models. First, note that if the electronic or ionic charge distribution leads to finite charge on different Wyckoff positions in the unit cell, we are left with an ionic crystal [88]. Therefore, a coarse graining or smoothing via a moving average is necessary to properly define edge and surface charge. In Appendix D 1 we present a discrete method that performs this task. We used this method for the analysis of the models discussed in Secs. V and VI A. However, while this coarse graining easily removes strong oscillations of the charge distribution on sub-unit-cell length scales, oscillations due to trivial edge-localized states can remain [29] and obscure the corner charge. Therefore, in Appendix D 2 we discuss a method that we developed to remove the signal due to such edge states. The method applies to the case when the *total* edge charge per unit cell (of the ribbon, i.e., the collection of sites periodically repeated in the ribbon geometry) is vanishing, but the presence of edge-localized states induces a nontrivial profile of the charge density as a function of the distance to the boundary, as has been observed for Sc_3AlC in Sec. VI A.

1. Coarse graining of charge distribution

To coarse grain the electric charge distribution defined on the *original lattice*, we first need to choose the *target lattice*. The choice of target lattice defines the coarse-graining length scale. To coarse grain over a single unit cell with multiple sites, it is convenient to consider a single Wyckoff position of maximal symmetry to define the target lattice. Some examples are shown in Fig. 23. Note that it is also possible to coarse grain over larger lengths scales, i.e., multiple unit cells. Such a situation is depicted in Fig. 23(c) where coarse graining is performed over seven original hexagonal unit cells. However, note that due to overlapping of the coarse-graining cells, the Wigner-Seitz tessellation formed around the coarse-graining centers (not illustrated) coincides with the original honeycomb lattice.

The coarse graining is performed by redistributing the charge from the original to the target lattice. If a site on the original lattice belongs to m coarse-graining cells, then a fraction $\frac{1}{m}$ of the total charge on the original site is distributed to each of the corresponding target sites. Consequently, charge on corner sites is generally transferred to a single target site. In Fig. 23(a), where we illustrate the coarse graining as applied to Sc_3AlC, redistribution weights of magnitude 1, $\frac{1}{2}$, and $\frac{1}{4}$ are illustrated with solid, dashed, and dotted arrows, respectively.

We have applied the coarse-graining method to achieve a charge redistribution in all the discussed models. In particular, Fig. 13 shows a comparison of the charge distribution before [Figs. 13(a) and 13(b)] and after [Figs. 13(c) and 13(d)] coarse graining for the C_4-symmetric model of Sec. II. The definitions of the original and target lattice as well as the coarse-graining unit cell are shown in Fig. 23(b). Figures 23(a) and 23(c) give the same information for the model

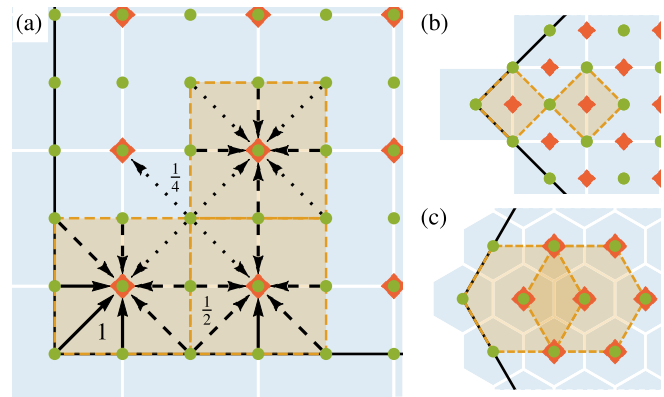

FIG. 23. Discrete coarse-graining method. (a) The charge on the original lattice (defined by the unit cells shaded in blue and sublattice sites shown as green disks) is redistributed to the target lattice (defined by the red diamond sites). Here the lattice corresponding to the projection of Sc_3AlC (see Sec. VI A) is shown. Each site in the target lattice is assigned a coarse-graining cell (unit cell of that lattice; shaded in orange). The charge on each green site is then redistributed (black arrows) with equal weights (weight 1 shown by solid, $\frac{1}{2}$ by dashed, and $\frac{1}{4}$ by dotted lines) to all those red sites whose coarse-graining cell is adjacent to the green site. Only a few arrows are shown to maintain clarity of the illustration. (b), (c) Definitions of the original (green) and target (red) lattice and the coarse-graining cell (orange) for the C_4- and C_6-symmetric models discussed in Sec. V, respectively. Note that in (c) the coarse-graining cells overlap; as a consequence, the original and the target lattice coincide except for a missing layer on the boundary.

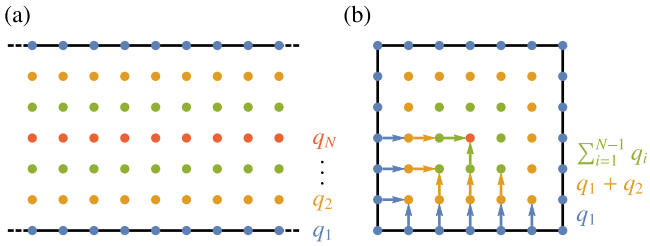

FIG. 24. Procedure to remove the edge signal from the charge distribution of a C_4-symmetric system. It is assumed that the total edge charge per unit cell (of the ribbon geometry) vanishes. The solid lines in both panels represent the boundary of the lattice. (a) Ribbon geometry extended in the horizontal direction with $2N - 1 = 7$ unit cells in the vertical direction (corresponding to $N = 4$ inequivalent layers). Unit cells of the lattice are indicated by dots, colored according to their distance to the boundary. We denote by q_i the charge per unit cell on the ith layer (which is constant within the layer). (b) Flake geometry for the same system. Here, *shells* of unit-cell sites (dots) correspond to the layers from the ribbon geometry (indicated by the corresponding color). The charge on the whole flake is redistributed according to the arrows indicated in the bottom-left part of the system. The amount of charge that is transferred from a site that belongs to the jth shell to the next one is given by $\sum_{i=1}^{j} q_j$, where q_i are the charges determined in the ribbon geometry [cf. (a)]. Note that the charge redistribution flows perpendicular to the boundary; therefore, no charge is transferred between the corners.

of Sc_3AlC (cf. Sec. VI A) and the C_6-symmetric models (cf. Secs. V B and V C), respectively.

2. Removal of edge signal from charge distribution

Even after coarse graining (as described above), charge oscillations caused by trivial edge-localized states can remain. Note that in contrast to the oscillations on sub-unit-cell scale, these remaining oscillations are generally perpendicular to the edges, and vanish in the bulk. Since the total corner and edge charges are defined via integration over regions with boundaries perpendicular to the edges of the sample [29], the remaining oscillations do not prevent us from computing these total charges [see Fig. 18(c) for such a calculation on the *original* coarse-grained data]. However, such oscillations can visually obscure the localization properties of the charge. Here, we discuss a method to subtract such edge-localized oscillations for the cases where the total edge charge per unit cell (of the ribbon geometry) vanishes. The method applies to C_n-symmetric systems with $n \geqslant 3$, where the bulk as well as the finite-size sample satisfy the symmetry requirement. For concreteness we choose $n = 4$ for the following discussion. In particular, the described setup directly applies to the case of Sc_3AlC as presented in Sec. VI A.

Two separate calculations need to be performed: one on a ribbon with $2N - 1$ layers (of unit cells) [cf. Fig. 24(a)] and one on a flake with N *shells* (of unit cells) [cf. Fig. 24(b)], such that there is a direct correspondence between the layers and the shells. Due to the rotational symmetry, the four sides of each shell are equivalent and only a single orientation of the ribbon needs to be computationally modeled. Note that compatible fillings (in particular, the same choice of chemical potential) need to be considered for the two systems. The

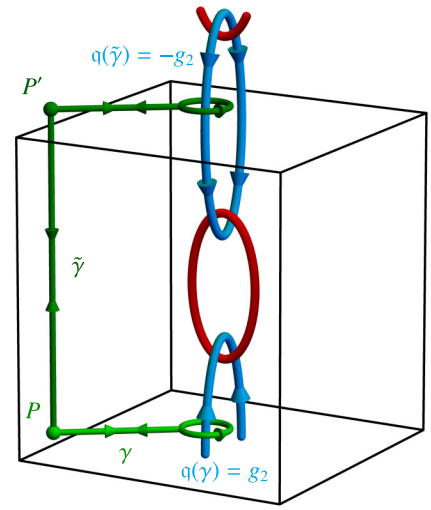

FIG. 25. Definition of nodal-line (NL) orientations via the non-Abelian invariant, illustrated on the example of multiband nodal link [60] of a three-band model; red (blue) line indicates a NL formed by the lower (upper) two bands. The non-Abelian invariant is computed on paths γ (light green) and $\tilde{\gamma}$ (dark green), where P' is shifted relative to P by a reciprocal lattice vector. In the three-band example shown here, $\mathfrak{q}(\gamma) = g_2$ (corresponding to a nodal line in the second gap, shown in blue) and bands 2 and 3 have different Berry phases $\phi_2 \neq \phi_3$. Therefore, the orientation of the upper blue nodal ring is opposite to the one of the lower ring, $\mathfrak{q}(\gamma) = -g_2$.

charge distributions obtained for both geometries first need to be coarse grained to the level of unit cells (cf. Sec. VI A), such that the coarse-grained lattice has a single site per unit cell. The resulting lattices are depicted in Figs. 24(a) and 24(b).

From the calculation on the ribbon, the total charge q_i per unit cell in the ith layer can easily be extracted. On the flake, we then redistribute the charge as indicated in Fig. 24 with arrows: from a site in the jth shell (but not on one of the diagonals) the charge $\sum_{i=1}^{j} q_i$ is transferred to the $(j + 1)$th shell. There is no charge transfer *away* from sites that lie on one of the diagonals. Therefore, this procedure seemingly leads to a charge accumulation on the diagonals and in the center. However, recall that, by assumption, the total edge charge

TABLE XI. Compounds with space-time inversion symmetry that host type-A triple points (TPs) on the given high-symmetry line (HSL) and are therefore candidates for having a nontrivial Euler monopole charge. Some compounds host multiple TPs. For each material and TP the space group, the HSL on which the TP lies, the nodal-line (NL) segment carrying the Euler monopole charge, i.e., the segment enclosed by the ellipsoid, the relevant Berry phases, and the Euler monopole charge induced from Wilson-loop spectra are shown.

Material	SG	HSL	NL segment	ϕ_B	χ
Na_2LiN	129	$\Gamma - Z - \Gamma$	[-0.29, 0.29]	$(0, \pi)$	2
			[0.29, 0.71]	$(\pi, 0)$	2
Li_2NaN [91]	191	$\Gamma - A - \Gamma$	[-0.08, 0.08]	(0,0)	0
			[0.08, 0.92]	$(0, \pi)$	2
TiB_2 [56]	191	$\Gamma - A - \Gamma$	[-0.26, 0.26]	$(0, \pi)$	2

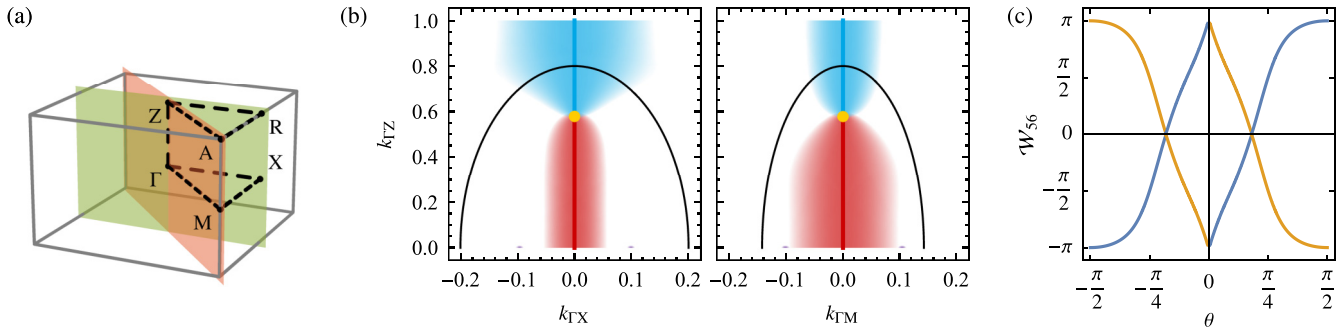

FIG. 26. Computation of Euler monopole charges of a pair of single triple points in Na_2LiN with the surface centered at Γ. (a) Shows the Brillouin zone, the high-symmetry points, and the planes in which the nodal lines are shown in (b). (b) Size of the four relevant gaps (orange, red, blue, and purple, according to increasing energy; at the triple point both the red and blue gaps are closed) in the two mirror planes shown in (a) encoded by the intensity of the color (and with a cutoff at a gap of 0.02 eV). The triple point (yellow) and the central nodal line are emphasized by appropriately colored overlays. (c) Wilson-loop spectrum computed for the relevant bands on the ellipsoid indicated in (b). We observe that the Wilson-loop spectrum winds twice, which implies $|\chi| = 2$.

vanishes, such that in the limit of large N, $\sum_{i=1}^{N} q_i = 0$. Consequently, the accumulated charge compensates oscillations on the diagonals and converges to zero at the center of the flake. Furthermore, note that the charge redistribution flows strictly *perpendicular* to the flake boundaries; therefore, no charge is transferred between the corners of the flake, keeping its value invariant (up to corrections that are exponentially small in the system size).

The effect of the method can be seen in Fig. 18, where the original (coarse-grained) distribution is shown in Figs. 18(d) and 18(e), and the charge distribution after removing the edge signal is displayed in Figs. 18(f) and 18(g). We remark that the data in Figs. 18(f) and 18(g) have undergone one additional coarse-graining step *after* the removal of the edge charge. Compared to Fig. 18(d), the localization of the corner charge in Fig. 18(f) is visually much more manifest.

APPENDIX E: GENERALIZED QUATERNION CHARGE IN DIFFERENT BRILLOUIN ZONES

In this Appendix we formalize the relationship between the orientation of nodal lines (NLs) and their copies in neighboring Brillouin zones (BZs). The orientation of a NL as used in Sec. III B can be formally defined using the non-Abelian invariant introduced by Ref. [66] (also called *generalized quaternion charge* therein). While the topological classification of band nodes is given by equivalence classes of the generalized quaternion group (each equivalence class contains either a single element or two elements that differ by a sign), the sign of the invariant becomes well defined if the contours have a common base point P. In that case the sign of the generalized quaternion invariant computed on a contour enclosing a single NL *defines* [71] the orientation of that NL (cf. Fig. 25).

The prior works [66,71] on the non-Abelian band topology have only considered closed contours which are fully contained within a single BZ. However, to understand the reversal of NL orientation between neighboring copies of BZ (cf. Fig. 6), one must explicitly consider paths that cross the BZ boundary. Such paths entail additional complications, as is well known from the case of the Zak-Berry phase [79,120]; namely, in general $\mathcal{H}(\mathbf{k})$ and $\mathcal{H}(\mathbf{k}+\mathbf{b})$, where $\mathbf{b}$ is any reciprocal lattice vector, are not identical, but are related by a diagonal unitary rotation. In the Supplemental Material [72] we explain how to compute the non-Abelian invariant in that case and then prove a very general statement relating the values of the invariant computed on contours shifted by a reciprocal lattice vector but connected to a common base point (see, e.g., the light and dark green paths γ and $\tilde{\gamma}$ in Fig. 25).

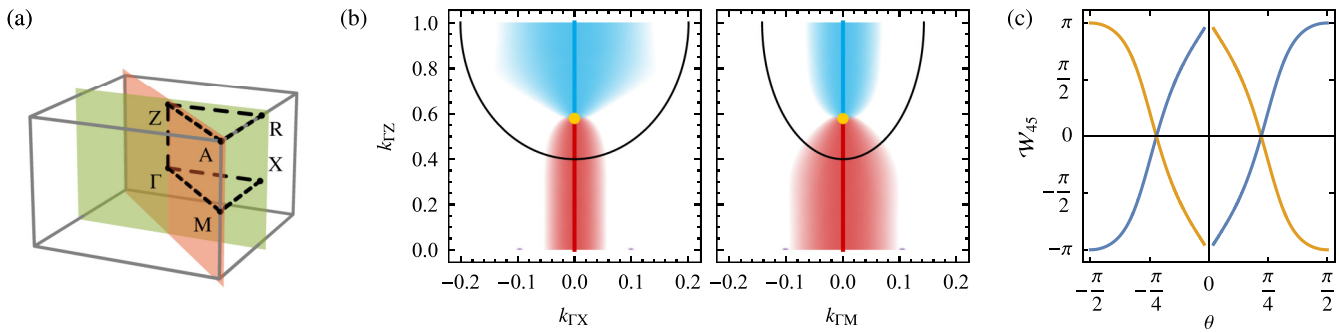

FIG. 27. Computation of Euler monopole charges of a pair of single triple points in Na_2LiN with the surface centered at Z. The organization of the panels is in one-to-one correspondence with Fig. 26 (the same cutoff of 0.02 eV is used). In (c) we observe that the Wilson-loop spectrum winds twice, which implies $|\chi| = 2$.

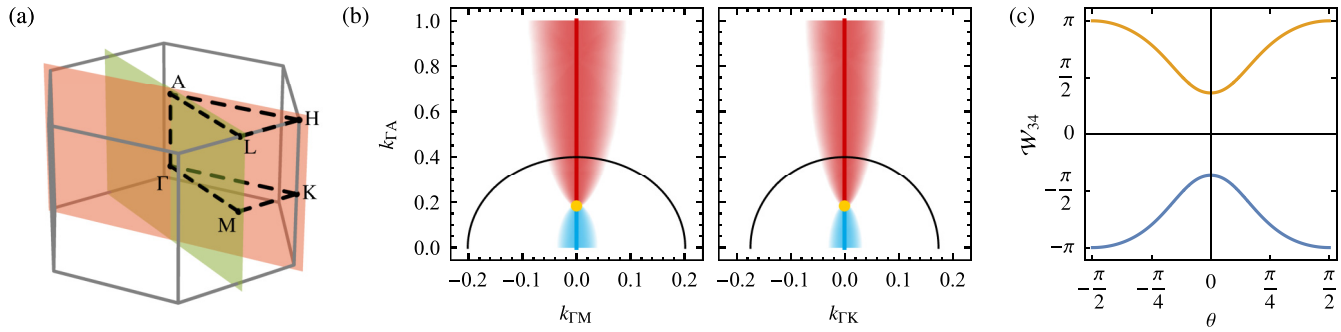

FIG. 28. Computation of Euler monopole charges of a pair of single triple points in Li_2NaN with the surface centered at Γ. The organization of the panels is in one-to-one correspondence with Fig. 26 (cutoff 0.02 eV). In (c) we observe that the Wilson-loop spectrum winds twice, which implies $\chi = 0$.

As a corollary of that general statement, we find that the following holds:

Corollary 1. Assume an N-band system with $\mathcal{PT}$ symmetry squaring to $+\mathbb{1}$ described in the orbital basis by a Hermitian Bloch Hamiltonian $\mathcal{H}(\mathbf{k})$. Let $\gamma : t \in [0, 1] \mapsto \gamma(t)$ be a closed contour with no band degeneracies located inside the (first) BZ. The path starts at the *base point* $P = \gamma(0) = \gamma(1)$ and we decompose

$$\mathfrak{q}(\gamma) = s \prod_{j \in J} g_j \tag{E1}$$

with $s \in \{\pm 1\}$, g_j the generators defined in Refs. [60,66], and $J \subseteq \{1, 2, \ldots, N-1\}$ a subset of the energy gaps of the N-band Hamiltonian (factors with smaller subscript j appearing to the right). Then, the generalized quaternion charge on the corresponding contour $\tilde{\gamma}$ with the same base point and enclosing the same band inversions but in the BZ shifted by the reciprocal lattice vector $\mathbf{b}$ (cf. Fig. 25) is

$$\mathfrak{q}(\tilde{\gamma}) = (-1)^m \mathfrak{q}(\gamma), \tag{E2}$$

where m is the number of elements of the set

$$\{j \in J | \phi_j \neq \phi_{j+1}\} \tag{E3}$$

with $\phi_j \in \{0, \pi\}$ the Berry phase of the jth band in the direction $\mathbf{b}$. [Note that in the conditioning in Eq. (E3) the label $j + 1$ may not be in the set J.]

We briefly discuss the application of Corollary 1 to the situation discussed in Sec. III B and depicted in Fig. 6. We are interested in the change of the orientation of the blue nodal ring when comparing two copies displaced by the primitive reciprocal lattice vector in k_z direction. Recall that the orientation of nodal lines (NLs) is defined via the generalized quaternion invariant of unique paths encircling those NLs with a fixed base point. This is exactly the situation of Corollary 1 with $\mathfrak{q}(\gamma) = sg_2$ (in the figure the case $s = +1$ is illustrated). Then, the corollary implies that the orientation changes if and only if the Berry phases of bands 2 and 3 are different, i.e., if $\phi_2 + \phi_3 = \pi \mod 2\pi$, in agreement with the statements in the main text. We also remark that if $\mathfrak{q}(\gamma) = \pm 1$ (i.e., if the Berry phase of each band on γ is trivial and *no* NLs are enclosed by γ), we have $J = \varnothing$ and Corollary 1 therefore immediately implies that $\mathfrak{q}(\gamma) = \mathfrak{q}(\tilde{\gamma})$.

APPENDIX F: ADDITIONAL MATERIAL EXAMPLES WITH EULER MONOPOLE CHARGE

From the list of triple-point (TP) materials in Ref. [59], we select additional candidates (aside from Li_2NaN) that potentially host TP-induced Euler monopole charges, namely, Na_2LiN, Li_2NaN, and TiB_2. Based on the first-principles calculations performed in Ref. [59] (and whose results are

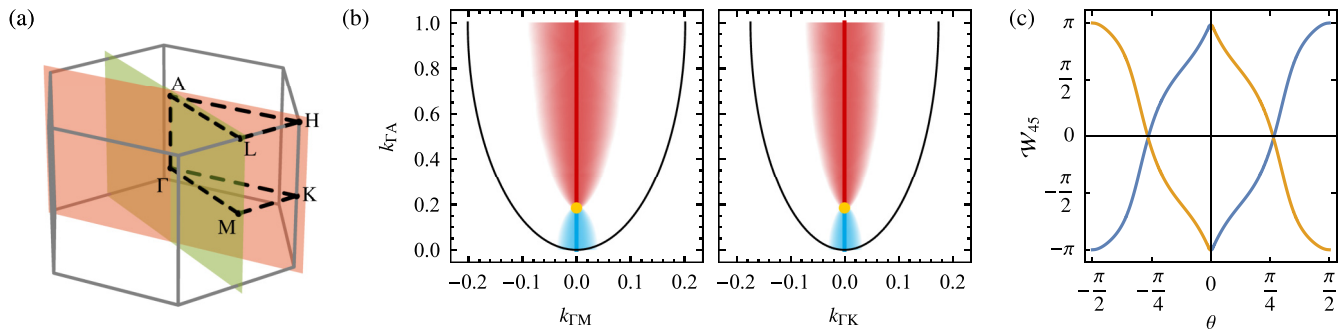

FIG. 29. Computation of Euler monopole charges of a pair of single triple points in Li_2NaN with the surface centered at A. The organization of the panels is in one-to-one correspondence with Fig. 26 (cutoff 0.02 eV). In (c) we observe that the Wilson-loop spectrum winds twice, which implies $|\chi| = 2$.

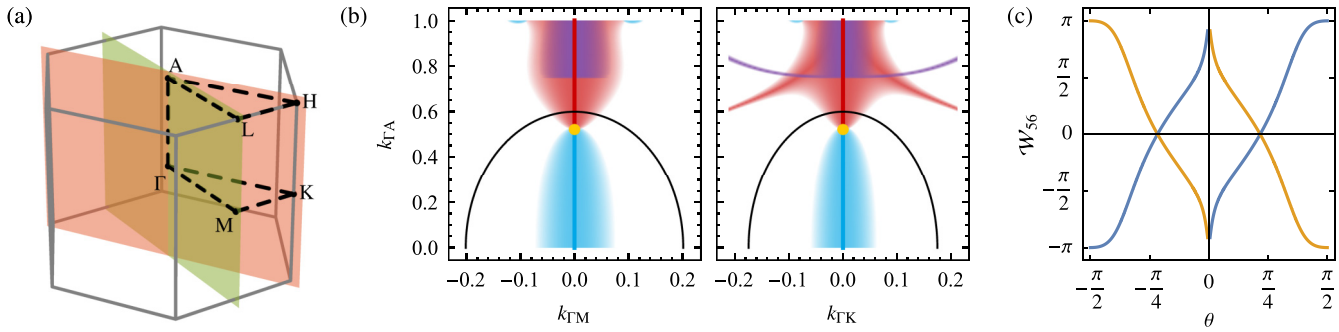

FIG. 30. Computation of Euler monopole charges of a pair of single triple points in TiB_2 with the surface centered at Γ. The organization of the panels is in one-to-one correspondence with Fig. 26 (cutoff 0.05 eV). In (c) we observe that the Wilson-loop spectrum winds twice, which implies $|\chi| = 2$.

given in the corresponding supplemental data and code [121]), we construct maximally localized Wannier functions using WANNIER90 [97] with *s* orbitals of alkali-metal elements, *d* orbitals of transition metal elements, and *p* orbitals of non-metal elements (for Li_2NaN no orbitals of Li are included). For the resulting Wannier tight-binding models we use the Python package Z2PACK [100,101] to compute the Wilson-loop spectra on ellipsoids enclosing the appropriate NL segments as well as the relevant Berry phases (cf. Fig. 6). The results are summarized in Table XI and in Figs. 26–30 we show for each TP material and NL segment the resulting Wilson-loop spectrum from the value χ of the Euler monopole charge is deduced. By comparing the Berry phases and the values of the Euler monopole charge, we verify the condition for nontrivial Euler monopole charge discussed in Sec. III B. We provide access to the Wannier tight-binding models as well as the Wilson-loop spectra in the supplementary data and code [114].

[1] W. A. Benalcazar, B. A. Bernevig, and T. L. Hughes, Science **357**, 61 (2017).
[2] W. A. Benalcazar, B. A. Bernevig, and T. L. Hughes, Phys. Rev. B **96**, 245115 (2017).
[3] Z. Song, Z. Fang, and C. Fang, Phys. Rev. Lett. **119**, 246402 (2017).
[4] F. Schindler, A. M. Cook, M. G. Vergniory, Z. Wang, S. S. P. Parkin, B. A. Bernevig, and T. Neupert, Sci. Adv. **4**, eaat0346 (2018).
[5] J. Langbehn, Y. Peng, L. Trifunovic, F. von Oppen, and P. W. Brouwer, Phys. Rev. Lett. **119**, 246401 (2017).
[6] M. Ezawa, Phys. Rev. Lett. **120**, 026801 (2018).
[7] F. Schindler, Z. Wang, M. G. Vergniory, A. M. Cook, A. Murani, S. Sengupta, A. Y. Kasumov, R. Deblock, S. Jeon, I. Drozdov, H. Bouchiat, S. Guéron, A. Yazdani, B. A. Bernevig, and T. Neupert, Nat. Phys. **14**, 918 (2018).
[8] F. K. Kunst, G. van Miert, and E. J. Bergholtz, Phys. Rev. B **97**, 241405(R) (2018).
[9] D. Călugăru, V. Juričić, and B. Roy, Phys. Rev. B **99**, 041301(R) (2019).
[10] M. J. Park, Y. Kim, G. Y. Cho, and S. B. Lee, Phys. Rev. Lett. **123**, 216803 (2019).
[11] M. Serra-Garcia, V. Peri, R. Süsstrunk, O. R. Bilal, T. Larsen, L. G. Villanueva, and S. D. Huber, Nature (London) **555**, 342 (2018).
[12] S. Imhof, C. Berger, F. Bayer, J. Brehm, L. W. Molenkamp, T. Kiessling, F. Schindler, C. H. Lee, M. Greiter, T. Neupert, and R. Thomale, Nat. Phys. **14**, 925 (2018).
[13] M. Serra-Garcia, R. Süsstrunk, and S. D. Huber, Phys. Rev. B **99**, 020304(R) (2019).
[14] S. Mittal, V. V. Orre, G. Zhu, M. A. Gorlach, A. Poddubny, and M. Hafezi, Nat. Photonics **13**, 692 (2019).
[15] B. Y. Xie, G. X. Su, H. F. Wang, H. Su, X. P. Shen, P. Zhan, M. H. Lu, Z. L. Wang, and Y. F. Chen, Phys. Rev. Lett. **122**, 233903 (2019).
[16] A. El Hassan, F. K. Kunst, A. Moritz, G. Andler, E. J. Bergholtz, and M. Bourennane, Nat. Photonics **13**, 697 (2019).
[17] M. Geier, L. Trifunovic, M. Hoskam, and P. W. Brouwer, Phys. Rev. B **97**, 205135 (2018).
[18] E. Khalaf, Phys. Rev. B **97**, 205136 (2018).
[19] J. Ahn, S. Park, and B.-J. Yang, Phys. Rev. X **9**, 021013 (2019).
[20] E. Lee, R. Kim, J. Ahn, and B.-J. Yang, npj Quantum Mater. **5**, 1 (2020).
[21] G. van Miert and C. Ortix, Phys. Rev. B **98**, 081110(R) (2018).
[22] Z. Wang, B. J. Wieder, J. Li, B. Yan, and B. A. Bernevig, Phys. Rev. Lett. **123**, 186401 (2019).
[23] L. Trifunovic and P. W. Brouwer, Phys. Rev. X **9**, 011012 (2019).
[24] C. W. Peterson, W. A. Benalcazar, T. L. Hughes, and G. Bahl, Nature (London) **555**, 346 (2018).
[25] Y. Hwang, J. Ahn, and B.-J. Yang, Phys. Rev. B **100**, 205126 (2019).
[26] T. E. Pahomi, M. Sigrist, and A. A. Soluyanov, Phys. Rev. Research **2**, 032068(R) (2020).
[27] B. J. Wieder and B. Andrei Bernevig, arXiv:1810.02373.
[28] W. A. Benalcazar, T. Li, and T. L. Hughes, Phys. Rev. B **99**, 245151 (2019).
[29] H. Watanabe and S. Ono, Phys. Rev. B **102**, 165120 (2020).
[30] R. Takahashi, T. Zhang, and S. Murakami, Phys. Rev. B **103**, 205123 (2021).
[31] Y. Fang and J. Cano, Phys. Rev. B **103**, 165109 (2021).
[32] L. Fu and C. L. Kane, Phys. Rev. B **76**, 045302 (2007).

[33] C. Fang, M. J. Gilbert, and B. A. Bernevig, Phys. Rev. B **86**, 115112 (2012).

[34] A. Alexandradinata, X. Dai, and B. A. Bernevig, Phys. Rev. B **89**, 155114 (2014).

[35] Y. Kim, B. J. Wieder, C. L. Kane, and A. M. Rappe, Phys. Rev. Lett. **115**, 036806 (2015).

[36] H. C. Po, A. Vishwanath, and H. Watanabe, Nat. Commun. **8**, 50 (2017).

[37] J. Kruthoff, J. de Boer, J. van Wezel, C. L. Kane, and R.-J. Slager, Phys. Rev. X **7**, 041069 (2017).

[38] B. Bradlyn, L. Elcoro, J. Cano, M. G. Vergniory, Z. Wang, C. Felser, M. I. Aroyo, and B. A. Bernevig, Nature (London) **547**, 298 (2017).

[39] Z. Song, T. Zhang, and C. Fang, Phys. Rev. X **8**, 031069 (2018).

[40] H.-X. Wang, Z.-K. Lin, B. Jiang, G.-Y. Guo, and J.-H. Jiang, Phys. Rev. Lett. **125**, 146401 (2020).

[41] Sayed Ali Akbar Ghorashi, T. Li, and T. L. Hughes, Phys. Rev. Lett. **125**, 266804 (2020).

[42] Q. Wei, X. Zhang, W. Deng, J. Lu, X. Huang, M. Yan, G. Chen, Z. Liu, and S. Jia, Nat. Mater. **20**, 812 (2021).

[43] M. Ezawa, Phys. Rev. B **97**, 155305 (2018).

[44] M. Ezawa, Sci. Rep. **9**, 5286 (2019).

[45] M. Lin and T. L. Hughes, Phys. Rev. B **98**, 241103(R) (2018).

[46] B. J. Wieder, Z. Wang, J. Cano, X. Dai, L. M. Schoop, B. Bradlyn, and B. A. Bernevig, Nat. Commun. **11**, 627 (2020).

[47] H. Qiu, M. Xiao, F. Zhang, and C. Qiu, Phys. Rev. Lett. **127**, 146601 (2021).

[48] K. Wang, J.-X. Dai, L. B. Shao, S. A. Yang, and Y. X. Zhao, Phys. Rev. Lett. **125**, 126403 (2020).

[49] Z. Zhu, G. W. Winkler, Q. S. Wu, J. Li, and A. A. Soluyanov, Phys. Rev. X **6**, 031003 (2016).

[50] T. T. Heikkilä and G. E. Volovik, New J. Phys. **17**, 093019 (2015).

[51] T. Hyart and T. T. Heikkilä, Phys. Rev. B **93**, 235147 (2016).

[52] H. Weng, C. Fang, Z. Fang, and X. Dai, Phys. Rev. B **93**, 241202(R) (2016).

[53] B. Q. Lv, Z. L. Feng, Q. N. Xu, X. Gao, J. Z. Ma, L. Y. Kong, P. Richard, Y. B. Huang, V. N. Strocov, C. Fang, H. M. Weng, Y. G. Shi, T. Qian, and H. Ding, Nature (London) **546**, 627 (2017).

[54] J.-Z. Ma, J.-B. He, Y.-F. Xu, B. Q. Lv, D. Chen, W.-L. Zhu, S. Zhang, L.-Y. Kong, X. Gao, L.-Y. Rong, Y.-B. Huang, P. Richard, C.-Y. Xi, E. S. Choi, Y. Shao, Y.-L. Wang, H.-J. Gao, X. D. Dai, C. Fang, H.-M. Weng *et al.*, Nat. Phys. **14**, 349 (2018).

[55] G. Chang, S. Y. Xu, S. M. Huang, D. S. Sanchez, C. H. Hsu, G. Bian, Z. M. Yu, I. Belopolski, N. Alidoust, H. Zheng, T. R. Chang, H. T. Jeng, S. A. Yang, T. Neupert, H. Lin, and M. Z. Hasan, Sci. Rep. **7**, 1688 (2017).

[56] X. Zhang, Z.-M. Yu, X.-L. Sheng, H. Y. Yang, and S. A. Yang, Phys. Rev. B **95**, 235116 (2017).

[57] J. Kim, H.-S. Kim, and D. Vanderbilt, Phys. Rev. B **98**, 155122 (2018).

[58] Y. Chen, Y. Xie, Y. Gao, P.-Y. Chang, S. Zhang, and D. Vanderbilt, Phys. Rev. Materials **2**, 044205 (2018).

[59] P. M. Lenggenhager, X. Liu, T. Neupert, and T. Bzdušek, Phys. Rev. B **106**, 085128 (2022).

[60] P. M. Lenggenhager, X. Liu, S. S. Tsirkin, T. Neupert, and T. Bzdušek, Phys. Rev. B **103**, L121101 (2021).

[61] G. W. Winkler, S. Singh, and A. A. Soluyanov, Chin. Phys. B **28**, 077303 (2019).

[62] Y. Xie, J. Cai, J. Kim, P.-Y. Chang, and Y. Chen, Phys. Rev. B **99**, 165147 (2019).

[63] A. Das and S. Pujari, Phys. Rev. B **102**, 235148 (2020).

[64] D. B. Litvin, *Magnetic Group Tables* (International Union of Crystallography, Chester, UK, 2013)

[65] C. J. Bradley and A. P. Cracknell, *The Mathematical Theory of Symmetry in Solids: Representation Theory for Point Groups and Space Groups* (Clarendon, Oxford, 1972).

[66] Q. Wu, A. A. Soluyanov, and T. Bzdušek, Science **365**, 1273 (2019).

[67] C. Fang, Y. Chen, H.-Y. Kee, and L. Fu, Phys. Rev. B **92**, 081201(R) (2015).

[68] T. Bzdušek and M. Sigrist, Phys. Rev. B **96**, 155105 (2017).

[69] Y. X. Zhao and Y. Lu, Phys. Rev. Lett. **118**, 056401 (2017).

[70] J. Ahn, D. Kim, Y. Kim, and B.-J. Yang, Phys. Rev. Lett. **121**, 106403 (2018).

[71] A. Tiwari and T. Bzdušek, Phys. Rev. B **101**, 195130 (2020).

[72] See Supplemental Material at http://link.aps.org/supplemental/10.1103/PhysRevB.106.085129, which includes additional Refs. [122–125], for a mathematical discussion and a rigorous proof of the orientation reversal, which arises when comparing two copies of a nodal line displaced by a reciprocal lattice vector, as summarized in Appendix E.

[73] A. Bouhon, Q. Wu, R.-J. Slager, H. Weng, O. V. Yazyev, and T. Bzdušek, Nat. Phys. **16**, 1137 (2020).

[74] A. Bouhon, T. Bzdušek, and R.-J. Slager, Phys. Rev. B **102**, 115135 (2020).

[75] F. N. Ünal, A. Bouhon, and R.-J. Slager, Phys. Rev. Lett. **125**, 053601 (2020).

[76] J. Noh, W. A. Benalcazar, S. Huang, M. J. Collins, K. P. Chen, T. L. Hughes, and M. C. Rechtsman, Nat. Photonics **12**, 408 (2018).

[77] A. Bouhon, A. M. Black-Schaffer, and R.-J. Slager, Phys. Rev. B **100**, 195135 (2019).

[78] A. Alexandradinata, J. Höller, C. Wang, H. Cheng, and L. Lu, Phys. Rev. B **102**, 115117 (2020).

[79] D. Vanderbilt, *Berry Phases in Electronic Structure Theory: Electric Polarization, Orbital Magnetization and Topological Insulators* (Cambridge University Press, Cambridge, 2018).

[80] D. Vanderbilt and R. D. King-Smith, Phys. Rev. B **48**, 4442 (1993).

[81] R. D. King-Smith and D. Vanderbilt, Phys. Rev. B **47**, 1651 (1993).

[82] L. Elcoro, B. J. Wieder, Z. Song, Y. Xu, B. Bradlyn, and B. A. Bernevig, Nat. Commun. **12**, 5965 (2021).

[83] Y. Xu, L. Elcoro, Z. D. Song, B. J. Wieder, M. G. Vergniory, N. Regnault, Y. Chen, C. Felser, and B. A. Bernevig, Nature (London) **586**, 702 (2020).

[84] X.-Q. Sun, S.-C. Zhang, and T. Bzdušek, Phys. Rev. Lett. **121**, 106402 (2018).

[85] A. A. Burkov, M. D. Hook, and L. Balents, Phys. Rev. B **84**, 235126 (2011).

[86] C. Fang, H. Weng, X. Dai, and Z. Fang, Chin. Phys. B **25**, 117106 (2016).

[87] X. Wan, A. M. Turner, A. Vishwanath, and S. Y. Savrasov, Phys. Rev. B **83**, 205101 (2011).

[88] H. Watanabe and H. C. Po, Phys. Rev. X **11**, 041064 (2021).
[89] S. Ren, I. Souza, and D. Vanderbilt, Phys. Rev. B **103**, 035147 (2021).
[90] T. Bzdušek, Q.-S. Wu, A. Rüegg, M. Sigrist, and A. A. Soluyanov, Nature (London) **538**, 75 (2016).
[91] L. Jin, X. Zhang, X. Dai, H. Liu, G. Chen, and G. Liu, J. Mater. Chem. C **7**, 1316 (2019).
[92] K. Persson, Materials Data on Sc_3 AlC (SG:221) by Materials Project, doi:10.17188/1207828.
[93] G. Kresse and J. Furthmüller, Phys. Rev. B **54**, 11169 (1996).
[94] G. Kresse and D. Joubert, Phys. Rev. B **59**, 1758 (1999).
[95] J. P. Perdew, K. Burke, and M. Ernzerhof, Phys. Rev. Lett. **77**, 3865 (1996).
[96] A. Jain, S. P. Ong, G. Hautier, W. Chen, W. D. Richards, S. Dacek, S. Cholia, D. Gunter, D. Skinner, G. Ceder, and K. a. Persson, APL Mater. **1**, 011002 (2013).
[97] G. Pizzi, V. Vitale, R. Arita, S. Blügel, F. Freimuth, G. Géranton, M. Gibertini, D. Gresch, C. Johnson, T. Koretsune *et al.*, J. Phys.: Condens. Matter **32**, 165902 (2020).
[98] N. Marzari, A. A. Mostofi, J. R. Yates, I. Souza, and D. Vanderbilt, Rev. Mod. Phys. **84**, 1419 (2012).
[99] X. Liu, Code for symmetrizing wannier90 matrices: https://github.com/Liu-Xiaoxiong/symmetrize_wann_matrix.
[100] A. A. Soluyanov and D. Vanderbilt, Phys. Rev. B **83**, 235401 (2011).
[101] D. Gresch, G. Autès, O. V. Yazyev, M. Troyer, D. Vanderbilt, B. A. Bernevig, and A. A. Soluyanov, Phys. Rev. B **95**, 075146 (2017).
[102] J. Gao, Q. Wu, C. Persson, and Z. Wang, Comput. Phys. Commun. **261**, 107760 (2021).
[103] M. I. Aroyo, J. M. Perez-Mato, D. Orobengoa, E. Tasci, G. De La Flor, and A. Kirov, Bulg. Chem. Commun. **43**, 183 (2011).
[104] M. I. Aroyo, J. M. Perez-Mato, C. Capillas, E. Kroumova, S. Ivantchev, G. Madariaga, A. Kirov, and H. Wondratschek, Z. Kristallogr. Cryst. Mater. **221**, 15 (2006).
[105] M. I. Aroyo, A. Kirov, C. Capillas, J. M. Perez-Mato, and H. Wondratschek, Acta Crystallogr. A **62**, 115 (2006).
[106] L. Elcoro, B. Bradlyn, Z. Wang, M. G. Vergniory, J. Cano, C. Felser, B. Andrei Bernevig, D. Orobengoa, G. De La Flor, and M. I. Aroyo, J. Appl. Crystallogr. **50**, 1457 (2017).
[107] M. Nakahara, *Geometry, Topology and Physics*, Graduate Student Series in Physics (Hilger, Bristol, 1990).
[108] S. Park, Y. Hwang, H. C. Choi, and B.-J. Yang, Nat. Commun. **12**, 6781 (2021).
[109] S. M. Young, S. Zaheer, J. C. Y. Teo, C. L. Kane, E. J. Mele, and A. M. Rappe, Phys. Rev. Lett. **108**, 140405 (2012).
[110] S.-S. Wang, Y. Liu, Z.-M. Y. Yu, X.-L. Sheng, and S. A. Yang, Nat. Commun. **8**, 1844 (2017).
[111] R. Yu, H. Weng, Z. Fang, X. Dai, and X. Hu, Phys. Rev. Lett. **115**, 036807 (2015).
[112] H. Weng, Y. Liang, Q. Xu, R. Yu, Z. Fang, X. Dai, and Y. Kawazoe, Phys. Rev. B **92**, 045108 (2015).
[113] C. Chen, Z. Su, X. Zhang, Z. Chen, and X.-L. Sheng, J. Phys. Chem. C **121**, 28587 (2017).
[114] P. M. Lenggenhager, X. Liu, T. Neupert, and T. Bzdušek, Data and code for: Universal higher-order bulk-boundary correspondence of triple nodal points, doi:10.3929/ethz-b-000490611.
[115] J. Zak, Phys. Rev. Lett. **62**, 2747 (1989).
[116] T. L. Hughes, E. Prodan, and B. A. Bernevig, Phys. Rev. B **83**, 245132 (2011).
[117] T. Bzdušek, Symmetry and topology of nodal semimetals, Ph.D. thesis, Eidgenössische Technische Hochschule Zürich, Switzerland, 2017, Sec. III.1.1.
[118] D. Varjas, T. Rosdahl, and A. R. Akhmerov, New J. Phys. **20**, 093026 (2018).
[119] M. G. Vergniory, L. Elcoro, Z. Wang, J. Cano, C. Felser, M. I. Aroyo, B. A. Bernevig, and B. Bradlyn, Phys. Rev. E **96**, 023310 (2017).
[120] J. Zak, Europhys. Lett. **9**, 615 (1989).
[121] P. M. Lenggenhager, X. Liu, T. Neupert, and T. Bzdušek, Data and code for: Triple nodal points characterized by their nodal-line structure in all magnetic space groups, doi:10.3929/ethz-b-000500759.
[122] M. Fruchart, D. Carpentier, and K. Gawedzki, Europhys. Lett. **106**, 60002 (2014).
[123] E. Dobardžić, M. Dimitrijević, and M. V. Milovanović, Phys. Rev. B **91**, 125424 (2015).
[124] A. Nelson, T. Neupert, A. Alexandradinata, and T. Bzdušek, Phys. Rev. B **106**, 075124 (2022).
[125] P. Woit, Lecture notes: Clifford algebras and Spin groups, http://www.math.columbia.edu/%7Ewoit/LieGroups-2012/cliffalgsandspingroups.pdf#page=6.